Universidade de São Paulo
Instituto de Física

Modelagem molecular de aditivos nanoestruturados em material asfáltico

Angèle Aja-Fowé

Orientador: Prof. Dr. Caetano Rodrigues Miranda

Tese de doutorado apresentada ao Instituto de Física da Universidade de São Paulo, como requisito parcial para a obtenção do título de Doutor em Ciências

São Paulo
2021

FICHA CATALOGRÁFICA
Preparada pelo Serviço de Biblioteca e Informação
do Instituto de Física da Universidade de São Paulo

Aja-Fowé, Angèle

Modelagem molecular de aditivos nanoestruturados em material asfáltico. São Paulo, 2021.

Tese (Doutorado) – Universidade de São Paulo. Instituto de Física. Depto. de Física dos Materiais e Mecânica.

Orientador: Prof. Dr. Caetano Rodrigues Miranda
Área de Concentração: Ciências de Materiais Computacionais

Unitermos: 1. Asfalto; 2. Modelagem molecular; 3. Nanopartículas.

USP/IF/SBI-061/2021

University of São Paulo
Institute of Physics

Molecular Modeling of Nanostructured Additives to Asphaltic Materials

Angèle Aja-Fowé

Supervisor: Prof. Dr. Caetano Rodrigues Miranda

Thesis submitted to the Institute of Physics of the University of São Paulo in partial fulfillment of the requirement for the degree of Doctor of Science

São Paulo
2021

Publications List in view

• Angèle Aja-Fowé, Michele Aparecida Salvador, and Caetano Rodrigues Miranda; *Study of asphaltene aggregation using molecular docking and density functional theory*; submitted to Energy & Fuels (2021)

• Angèle Aja-Fowé, Alexsandro Kirch, and Caetano Rodrigues Miranda; *The role of silica nanoparticles on the mechanical properties of asphalt: a molecular dynamics study*; submitted to The Journal of Physical Chemistry C (2021)

Acknowledgments

• First of all, I thank Almighty God for his love, his favor, his grace, his goodness, and the power he put in me so I may achieve this project.

• I would like to express my sincere thanks to my supervisor Prof. Dr. Caetano Rodrigues Miranda for giving me this research topic, for his support, suggestions, encouragement, and the scientific knowledge provided throughout my work.

• My special thanks go to Dr. Alexsandro Kirch for the suggestions and reviews he has provided for this work. I thank all my labmates at the SAMPA group for their support and the nice time we have spent together.

• I express my deepest thanks to my parents Fowé Jean Pierre Marie and Donjeu Cécile, my fiancé Sop Sidzé Sylvain Landry, my kids Djouédjong Gloria Priscille and Fowé Humilde, my sisters and brothers Alida, Ninon, Elvira, Frederic, Zita, Boris, Christian, and my nephew and nieces for their moral and psychological support, and their unconditional love.

• I acknowledge the NanoPetro workstations on the Josephson Cluster for the computational time provided. I would like to acknowledge to CNPq and CAPES funding agencies for their financial support throughout my research.

• I express my grateful acknowledge the African Institute for Mathematical Science (AIMS) - Cameroon that has given me the first opportunity of interacting with scientists from the various continent and to conduct my goal toward an international research level.

• Finally, I deeply thank the International Centre for Theoretical Physics (ICTP) for the deep knowledge provided for my career and the great opportunities given to me and which has led me to meet my supervisor without whom I will have not to carry out my Ph.D. at the prestigious University of Sao Paulo.

Abstract

Asphalt is a highly complex material formed as a by-product of the distillation of crude oil, used in road pavements, also known as bitumen. Its composition contains more than one million distinct molecules, varying in polarity and molecular weight; in general, a mixture of aliphatic, aromatic, and naphthenic hydrocarbons. The performance of asphalt pavement strongly depends on both its chemical composition and the aggregates. Because of its complexity, the chemical composition of asphalt can not be unequivocally determined. Building a model asphalt for molecular simulation is important to correlate the physical properties at the atomic level that strongly affect the overall highway performance and durability of asphalt. Besides, the interaction mechanism of inorganic nanostructure to solve the current durability issues is still inconclusive. To contribute to the improvement of the current performance of asphalt pavement, this thesis has focused on developing a new molecular model of asphalt for molecular simulation and studying the effects of silica (SiO_2) nanoparticles (NPs) on the thermodynamics and mechanical properties of asphalt. The model asphalt was based on a real sample from the Brazilian/Laguna ABG crude oil source. The chemical composition of the model asphalt was subdivided into four groups: asphaltenes, polar aromatics, naphthene aromatics, and saturates. Four components were used to represent each group in the ABG, namely, docosane $C_{22}\,H_{46}$, 1,7-dimethylnaphthalene $C_{12}\,H_{12}$, resin (R) $C_{26}\,H_{41}\,S_2\,N$ and asphaltene (A) $C_{53}\,H_{58}\,S$ in the proportions of [19.1:46.5:18.7:15.8] respectively. As the first step of this work, the description from the dimer to hexamer interaction of the A and R molecules was investigated in steps. Molecular docking was used to select the most favorable conformation. Then, we used density functional theory (DFT) to analyze the energetic, electronic, and structural properties of the aggregates. The results in this step provided aggregates with sizes between 3.67 Å and 22.25 Å. The results indicated that formation energy increases considerably from dimer to the hexamer with values between -25.85 kcal/mol and -245.90 kcal/mol. Whereas the optimized structures of the aggregates with large aromatic rings were energetically more favorable because the interaction was mainly carried out by the $\pi - \pi$ stacking in the aromatic ring. In the second step, molecular dynamics (MD) simulations were used to investigate the role of additive hydroxylated silica nanoparticles on the thermodynamics and mechanical properties of the model asphalt. Three hydroxylated SiO_2-NPs models were used with different hydroxylated terminal group distribution on the amorphous SiO_2-NP surface: model A contains 83 % Si(OH), and 17 % $Si(OH)_2$; model D has 17 % Si(OH), and 83 % $Si(OH)_2$; and model E with 50 % Si(OH), 50 % $Si(OH)_2$. These properties include density, bulk modulus, isothermal compressibility, and viscosity. It was found that the ABG and modified ABG with SiO_2-NPs displayed physical properties that were qualitatively similar to those of real asphalt. The densities of the modified ABG models were higher than that of the ABG asphalt. After adding the NPs, the viscosity and the bulk modulus of the modified asphalts significantly improved as these properties increased compared to the neat model. This result is highly dependent on the hydrophilic coverage of the nanoparticle with the geminal-rich model displaying the highest values at room temperature. The achievements of this thesis may guide developments target to prevent mechanical deformation in the asphalt pavement and civil and infrastructure applications.

Keywords: Asphalt; molecular simulations; asphaltene aggregation; silica nanoparticles; molecular docking

Resumo

O asfalto é um material altamente complexo formado como subproduto da destilação do petróleo bruto, utilizado em pavimentação asfáltica, também conhecido como betume. Sua composição contém mais de um milhão moléculas distintas, variando em polaridade e peso molecular; em geral, uma mistura de hidrocarbonetos alifáticos, aromáticos e naftênicos. O desempenho do pavimento asfáltico fortemente depende de sua composição química e dos agregados. Devido à sua complexidade, a composição química do asfalto não pode ser determinada de forma inequívoca. Construir um modelo de asfalto para simulações moleculares é importante para correlacionar as propriedades físicas no nível atômico que afetam fortemente ao desempenho pavimentação e durabilidade do asfalto. Além disso, ao mecanismo de interação da nanoestrutura inorgânica para resolver os atuais problemas de durabilidade ainda é inconclusivo. Para contribuir com a melhora do desempenho atual do pavimento asfáltico, esta tese se concentrou no desenvolvimento de um novo modelo molecular de asfalto para simulação molecular e no estudo dos efeitos das nanopartículas (NPs) de sílica (SiO_2) na termodinâmica e nas propriedades mecânicas do asfalto. O modelo de asfalto foi baseado em uma amostra real da fonte de petróleo bruto ABG brasileira / Laguna. A composição química do asfalto modelo foi subdividida em quatro grupos: asfaltenos, polares aromáticos, nafteno aromáticos, e saturados. Quatro componentes foram utilizados para representar cada grupo no ABG: Docosano $C_{22}\,H_{46}$, 1,7-dimetilnaftaleno $C_{12}\,H_{12}$, resina (R) $C_{26}\,H_{41}\,S_2\,N$ e asfalteno (A) $C_{53}\,H_{58}\,S$ nas proporções de [19,1:46,5:18,7:15,8], respectivamente. Como etapa inicial deste trabalho, a descrição da interação dímero até hexâmero das moléculas A e R foi investigada em etapas. Docking molecular foi usado para selecionar a conformação mais favorável. Em seguida, utilizamos a teoria do funcional da densidade (DFT) para analisar as propriedades energéticas, eletrônicas e estruturais dos agregados. Os resultados nesta etapa indicaram que a energia de formação aumenta consideravelmente do dímero para o hexâmero com valores entre -25,85 kcal/mol e -245,90 kcal/mol. Já as estruturas otimizadas dos agregados com anéis aromáticos foram energeticamente mais favoráveis graças a interação resultante do empilhamento $\pi - \pi$ nos anéis. Na segunda etapa, simulações de dinâmica molecular (MD) foram utilizadas para investigar o papel das nanopartículas de sílica hidroxilada aditiva na termodinâmica e nas propriedades mecânicas do modelo de asfalto. Três modelos hidroxilados de NPs de SiO_2 foram usados com diferentes distribuições de grupos terminais hidroxilados na superfície amorfa de NP: o modelo A contendo 83% de Si(OH) e 17% de $Si(OH)_2$; o modelo D com 17% de Si(OH) e 83% de $Si(OH)_2$; e o modelo E com 50% de Si(OH), 50% de $Si(OH)_2$. Essas propriedades incluem densidade, módulo volumétrico, compressibilidade isotérmica e viscosidade. Verificou-se que o ABG e o ABG modificado com NPs de SiO_2 exibiram propriedades qualitativamente semelhantes às do asfalto real. As densidades dos modelos ABG modificados foram maiores do que as do asfalto ABG. Depois de adicionar as NPs, a viscosidade e o módulo volumétrico dos asfaltos modificados melhoraram significativamente em comparação com o modelo original. Este resultado é altamente dependente da cobertura hidrofílica da nanopartícula com o modelo rico em geminal exibindo os valores mais altos a temperatura ambiente. Os avanços dessa tese podem orientar o desenvolvimento para prevenção da deformação mecânica em aplicações de pavimentação asfáltica e aplicações em engenharia civil e infraestrutura.

Palavras-chave: Asfalto; Simulação Molecular; Agregação de Asfalteno; Nanopartículas de sílica; Docking Molecular.

Dedicated to my dad and mum Jean Pierre Marie Fowé & Cécile Donjeu

CONTENTS

CHAPTER 1

INTRODUCTION

1.1 Thesis description and motivation

Asphalt pavement consists of multiple layers which include unbound and bituminous-bound materials as shown in Figure 1.1 [1]. The pavement structure is comprised of layers produced with different materials which lays on a subgrade (foundation). On top of the subgrade, there is the sub-base layer following by a course-based which itself is cover by asphalt layers.

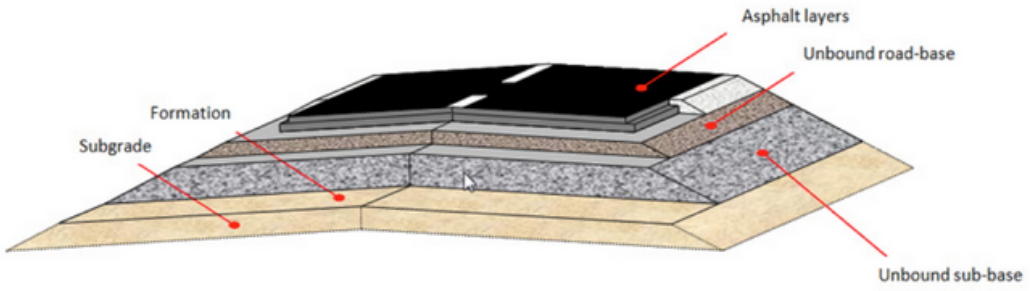

Figure 1.1: Asphalt pavement [1]

Asphalt is the heaviest fraction of crude oil or petroleum. In Europe, asphalt can be considered as a mixture of mineral aggregates and binder (bitumen) also known as asphalt mixture or asphalt concrete. Figure 1.2 shows a schematic definition of the asphalt mixture.

Aggregates are crushed rocks, sand, gravel, or other mineral matter. Bitumen is a black, brown to a dark viscous mineral substance that is used to hold aggregates together [2, 3, 4, 5].

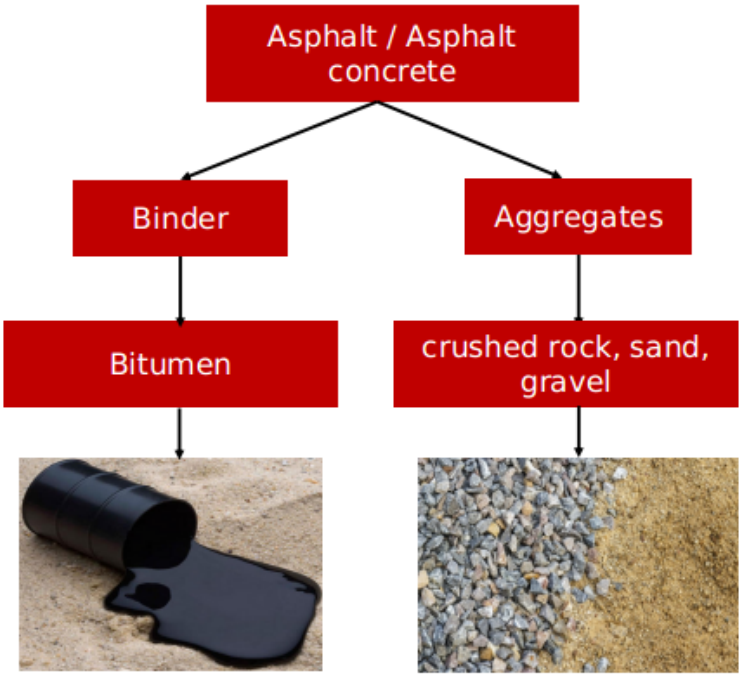

Figure 1.2: Schematic view definition of the asphalt

In North America, asphalt is referred to as a binder also called asphalt binder. The terms asphalt and bitumen can then be used as synonymous. In our work, we shall use naming from North America to represent the asphalt. Figure 1.3 shows the asphalt in its viscous form.

Figure 1.3: Asphalt viscous dark material [6]

Crude oils are made up of hydrocarbon, in general in a liquid phase. It also contains components of sulfur (S), nitrogen (N), oxygen (O), and other elements. The chemical nature of crude oils is very complex and their constituents can be classified based on the types of hydrocarbon and the molecular weight [7, 8]. There are four types of chemical components found in crude oils. 1) Paraffins: they are straight chains of hydrocarbon joined by a single bond. Paraffins are very stable and saturated molecules. 2) Naphthenes: these components are cyclic hydrocarbon also called cycloparaffins which are joined by single bonds. As paraffins, naphthenes are very stable and saturated. These two classes of hydrocarbon are also called saturates. 3) Aromatics: these are hydrocarbons derivatives of benzene. They are unsaturated and very stable. Paraffin, naphthene, and aromatic are relatively lighter and are colorless molecules. 4) Asphaltenes are the colored (black to brown), solid or viscous hydrocarbon components found in crude oil. They are made up of cyclic and aromatic rings with aliphatic chains. Asphaltenes are relatively high molecular weight. There are other types of components found in crude oil called resin. Resin has properties between asphaltene and saturates. They are viscous or liquid and are less colored than asphaltene.

As automobiles grow in popularity, the demand for more and better roads leads to innovations in both production and performance of asphalt. According to the National Transport Confederation of Brazil (CNT) [9], in 2018, a survey of 107161 km of highway shows that 50.9 % have pavement problems compared to the year 2019 with 52.4 % on 108863 km evaluated. Studies have been carried out on asphalt molecular structure and their physical and chemical properties at the atomic level to improve the performance of the road pavement [10, 11, 12, 13, 14, 15, 16, 17, 18]. However, only a few models of asphalt for molecular dynamics simulation have been developed up to date with none of them based on Brazilian asphalt. Building models asphalt for molecular simulation from Brazilian crude oil sources is important as it contributes to the prediction of quality and durability of asphalt pavement and therefore has a positive impact on the environment and economy. Indeed, a good chemical structure representation of asphalt could be useful to correlate the physical properties to the engineering one. The model asphalt constructed can therefore be used to predict the rheological and mechanical properties of asphalt pavement.

Studies have shown that the addition of polymer nanocomposites can improve the mechanical properties of asphalt. Researchers have put their interests in this sense and

they found that nanomaterials have a significant effect in improving the engineering properties of asphalt binder [19, 20, 21, 22, 23, 24, 25]. This class of material is generally composed of clay functional with radical polymers. From the applied point of view, this means that the use of nanostructures has a great potential of reducing the formation of cracks and mechanical deformations in asphalt pavements.

Nanomaterials used in construction include sand, granite, limestone, quartz, etc. In particular, Silica (SiO_2) is common in sand and granite with a high percentage. Caetano Miranda and coworkers have developed several studies involving the use of hydroxylated silica nanoparticles in interfaces of interest to the Oil industry [26, 27, 28, 29, 30, 31]. As a natural extension of these investigations, given the advantages in terms of synthesis, cost, and stability, we will investigate the potential use of SiO_2 nanoparticles as additives for asphalts.

1.2 Asphalt composition, production, and usefulness

Generally, asphalt is composed of a mixture of aliphatic, aromatic, and naphthenic hydrocarbons. They all consist mainly of compounds of carbon (C) and hydrogen (H), but often contain N, S, and O. In solid forms, it may contain iron (Fe), silicon (Si), Nickel (Ni), and aluminum (Al). A generic asphalt elemental analysis shows that it has approximately 84 % of C, 10 % of H, 1 % of O, and the remainder consists of several other elements [10, 3, 32]. Because of its complexity, the chemical composition of asphalt can not be unequivocally determined. However, its components can be grouped based on their polarity, solubility, and molecular weight into asphaltenes, saturates, and resin [33, 34]. This later can still be subdivided into naphthene-aromatic and polar-aromatic as shown in Figure 1.4.

Asphalt occurs naturally in both asphalt lakes and rock asphalt (a mixture of sand, limestone, and asphalt). Nowadays, the production of refined petroleum asphalt outstripped the use of natural asphalt. Asphalt is produced by removing the lighter fractions (such as liquid petroleum gas, petrol, and diesel) from heavy crude oil during the refining process [35]. After the distillation process of crude oil, the residue deposit is asphalt mud in its basic form. To obtain asphalt in the liquid state, many processes such as cutting back, emulsifying, and

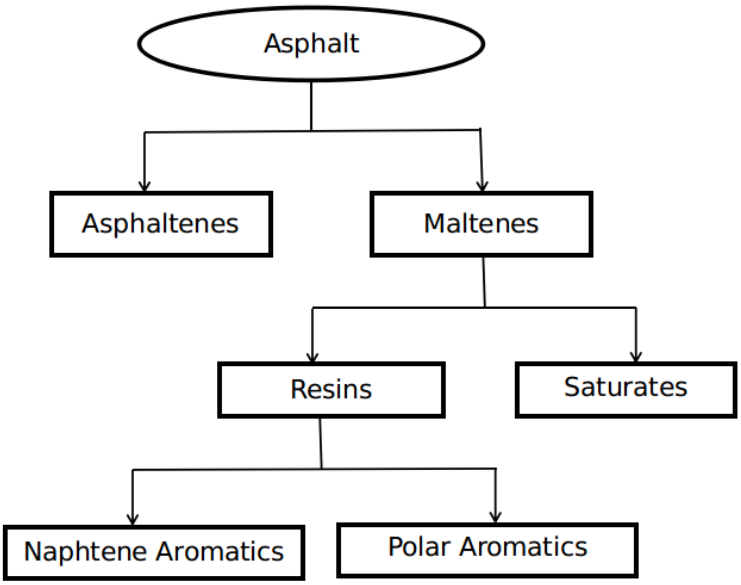

Figure 1.4: Chemical composition of a generic asphalt model

air blowing [36] have to be done in an asphalt plant: 1- Cutting back consists to blend the asphalt residue with a volatile substance which gives out a more malleable asphalt; 2- The emulsifying process consists of adding an emulsifying agent such as clay and silicates to the asphalt to reduce the capacity of asphalt to separate with water; 3- The air blowing consist of injecting air into asphalt after heating it at high temperature (up to 500 ^{o}C) thus, making asphalt to remain in the liquid state when cooling.

Asphalt is an excellent waterproofing agent and was long used in shipbuilding. It was heated and applied all over the bottom of the ships to prevent attack by sea creatures. Nowadays, the main use of asphalt is for road pavement. Asphalt can also be used for surfacing work on airfields, vehicle parking areas, sport, and recreation areas.

1.3 Objectives and scopes

The goals of this work are to 1) develop a molecular model of asphalt for molecular simulation which has average molecular structures similar to those of Brazilian/Laguna ABG asphalt from the Strategic Highway Research Program (SHRP) [14]. -"The SHRP was a highly focused, ambitious research effort that targeted four specific areas for intense study over the time frame from 1987 to 1993. Asphalt was one of the four study areas [37]"-. 2) Study the

effects of silica nanoparticles modification on the physical properties of the ABG asphalt, to predict the macro-level properties of asphalt. Molecular simulation is one way to predict the macroscopic properties that result from specified microscopic molecular interactions and structures. We will investigate the effects of intrinsic properties of asphalt through multiscale molecular simulations where some theoretical models will be presented.

This is an essential work for the development of the asphalt molecular models, where thermodynamic and mechanical properties will be determined for different types of hydroxylated silica nanoparticles to identify which ones potentially improve the mechanical response of asphalt as well as how stable they are in that system. This thesis is important to propose possible models of asphalt for molecular simulation with an improvement on the asphalt response and therefore contribute to energy and environmental technologies. The research results' contributions of this thesis to the Science and Technology are the following:

1) Explanation of the physicochemical nature of the aggregation of asphaltenes molecules, which can form nanoaggregates up to the hexamer.

2) Proposition of a molecular model for asphalt with typical compositions found in Brazil.

3) Design and computational screening of silica nanoparticles as additives to asphalt to improve its mechanical properties.

1.4 Outline of the thesis

We have begun with an introduction in Chapter 1, in which we have presented the summary of the thesis including the motivations and the objectives. In Chapter 2, we have reviewed the fundamentals of molecular modeling and simulation of asphalt including the chemical composition and physical properties. Chapter 3 is devoted to the methodologies used in this thesis. These include first principles, molecular mechanics and dynamics simulation techniques. In Chapter 4, the results on asphaltene aggregation using molecular docking and first-principles calculations are presented. Chapter 5 refers to the construction of the asphalt molecular models for molecular simulation and the study of thermodynamics and mechanical properties. Chapter 6, consists of building modified molecular models of asphalt with silica nanoparticles and studying the improvement on the thermodynamics and mechanical properties. Finally, in Chapter 7, a summary of the key findings of the thesis and perspectives for further studies are

presented.

CHAPTER 2

LITERATURE REVIEW

In this chapter, we provide a review of the most relevant studies on the molecular modeling of asphalt. Many studies have been previously carried out to identify the asphalt molecular structure and their physical properties at the atomic level aiming to improve the performance of the road pavement [10, 11, 12, 13, 14, 15]. Those studies are mainly based on experimental methods with only a few studies focusing on molecular simulations. Firstly, we will review the simulation of asphaltene (which is the heavier component of the asphalt) and its aggregates, and then, we will introduce the molecular models of asphalt that have been developed so far. Finally, we will review some previous works on the silica nanoparticles application to the Oil & Gas industry.

2.1 Molecular simulation of asphaltene models

In recent years, many studies employing molecular simulation on the study of asphaltene aggregates have been carried out [38, 39, 40, 41, 42, 43, 44, 45]. There is a consensus that the asphaltene aggregates have around 6 nm, and are built of at most 10 molecules [38, 39, 40, 41, 42, 46, 47]. Murgich *et al.* [39] have investigated the aggregation of resins and a highly aromatic asphaltene model (24 aromatic rings) using molecular mechanics. An initial

configuration was specified and the inter-atomic distances and bond angles were adjusted, using Insight II and Discover 2.2 package [48] until the minimum energy configuration was obtained. The aggregate of the dimers, trimers, and tetramers showed that the interaction is mainly in the aromatic planes and the alkyl parts of the model asphaltene limit the growth of aggregates through steric interference.

Rogel [49] studied the aggregation and the solubility of two different asphaltene molecules in toluene and heptane with a broad range of aromatic rings (8-22) using molecular mechanics and dynamics, as implemented in the Discover 2.0 module of Biosym [48]. The results of the molecular dynamics (MD) on the aggregation process showed that the solubility parameter was reduced with an increased number of molecules in the aggregates (from dimer to tetramer). The distance between the layers of the calculated aggregates varied between 3.60 and 3.80 Å and the interaction energy in the vacuum between -47 and -427 kcal/mol. In 2000, Rogel E. [50] used molecular mechanics and dynamics to study the forces that determine the aggregation process of 8 models asphaltenes and resins in crude oils. The stabilization energies of the dimer aggregates are in part governed by the van der Waals forces between the molecules. Molecules with higher aromaticity are energetically more favorable. While the one with lower aromaticity destabilizes the association of the asphaltene and resin.

The simulations of asphaltene dimers performed by Carauta *et al.* [51] containing two types of asphaltenes molecules showed that the intermolecular distances are greater than that of Rogel [50]. The aggregation process occurred with the formation energy of -58.91 and -45.07 kcal/mol depending on the asphaltene molecule. Headen *et al.* [46] have conducted classical MD simulations of four asphaltenes models, a model resin, and their mixtures in toluene and heptane. The classical potentials OPLS-AA force-field together with GROMACS MD simulation code (version 4.6) [52, 53, 54] was used to study the aggregation mechanism. It was found that the average aggregation number were 3.6 and 5.6, but the predominant species were monomers and dimers.

Very few studies have investigated asphaltenes from the first-principles point of view. Lima *et al.* [55] used a combined methodology of Molecular Mechanics (MM) and Density Functional Theory (DFT) to study the interactions and the role of the resin molecule in asphaltene nanoaggregates. The study on the dimers and trimers has shown that resins might be destabilizers on the nanoaggregation process. Besides, the trimers were found to be three

times energetically favorable than the dimers.

2.1.1 Quantitative Molecular Representation of asphaltene-A and resin-R

In this section, we discuss the work of Boek *et al.* [56] where they propose a quantitative molecular representation (QMR) of asphaltene structures based on experimental data [57, 58]. The experimental data include elemental analysis, molecular weight (MW), and nuclear magnetic resonance (NMR) spectroscopy (of both ^{1}H and ^{13}C). A nonlinear optimization procedure was used to select the samples of molecules that give the best match with experimental data. For the different MW used, it was observed that the QMR method gives significantly smaller values for the objective function in the case of MWs of 1028 and 750 g/mol. Giving rise to the best reliable representation.

A computer algorithm based on Monte Carlo was developed to generate the molecular representations of the asphaltenes. In this method, a broad set of paraffins, cycloparaffins, and aromatics building blocks are sampled randomly and linked together to form asphaltene-like molecules. The building blocks are generated manually or automatically during the simulation. They are composed of both aromatic building blocks (aromatic and naphthenic rings) and aliphatic building blocks, thus, forming a unit sheet. The aromatic building blocks are made up of small (one, two, and tree) and large (four, and five) rings and may contain heteroatoms such as S, O, and N. Whereas the aliphatic building blocks consist of n-alkanes from 1 to 50 C, a number of branched alkanes, and chains containing heteroatoms.

Each asphaltene molecule is described in terms of the number of the unit sheet which includes the number of aromatic rings, the number of naphthenic rings, the number of alkyl chains, and the length of each alkyl chain. Asphaltene structures are composed of relatively small unit sheets, each built from 8-10 aromatic cores and linked via alkyl chains. This approach used by Boek and collaborators to generate molecular representations of asphaltenes models leads to a more generic and realistic model in comparison with the models that were previously employed in the literature.

Obtaining an accurate molecular model for asphalt that reproduces a better road pavement is an important part of our work, because the performance of asphalt depends in part on its

chemical and elemental composition (mainly the asphaltene component). We therefore used in our work two of the asphaltene models obtained by Boek *et al.* [56] that are asphaltene A $C_{53}\,H_{58}\,S$ and resin R $C_{26}\,H_{42}\,S_2\,N$ represented in Figure 2.1.

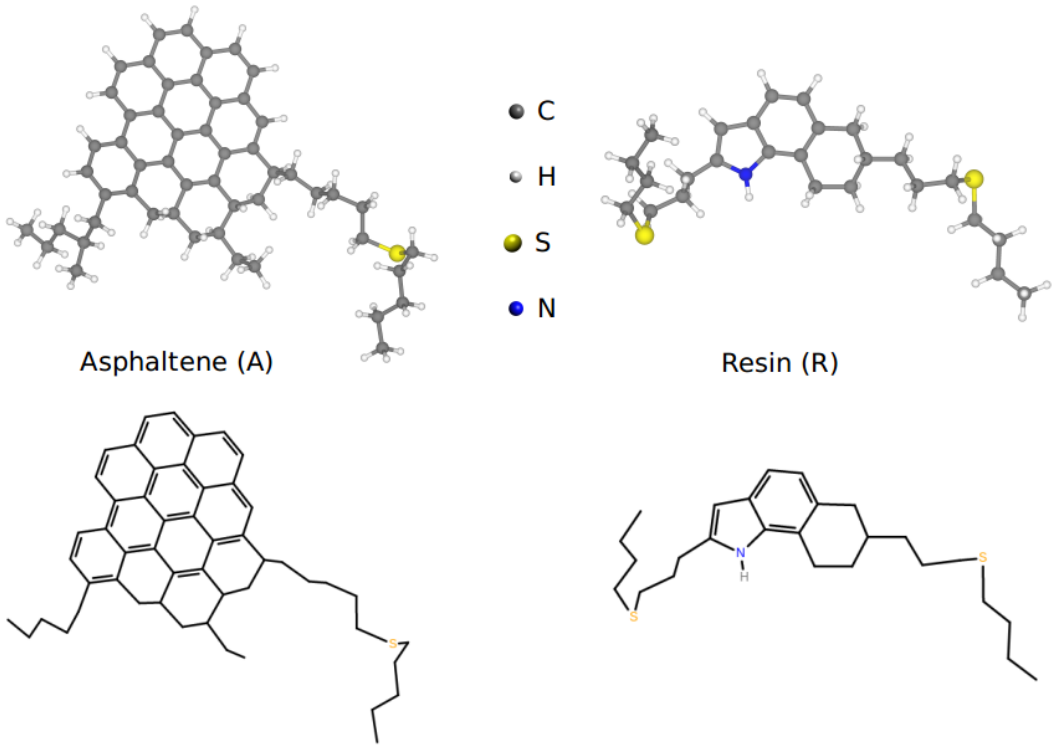

Figure 2.1: Ball-and-stick representations of asphaltene (A) $C_{53}\,H_{58}\,S$ and resin (R) $C_{26}\,H_{42}\,S_2\,N$ on top; down is the chemical structure

We selected these two molecules because they are the ones that show the best concordances with the experimental data [57, 58]. In particular, the asphaltene A has MW 726 g/mol with one heteroatom of S, 87.6 % mass of C, 8.0 % mass of H, and 4.4 % mass of S. Whereas the resin R has MW 431 g/mol with two S and one N atoms, 72.4 % mass of C, 9.5 % mass of H, 14.9 % mass of S, and 3.2 % mass of N. These elemental compositions typically correspond to the experimental data [59, 60].

2.2 Atomistic Models and Molecular Simulation of Asphalt

Three types of molecules are present in the asphalt: aliphatic, aromatic, and naphthenic. These molecules interact with each other and directly affect the physical and chemical behavior of asphalt. There is no exact structure of asphalt, however, its components can be grouped into four parts which are asphaltenes, polar-aromatics/resins, naphthene-aromatics/aromatics, and saturates. Up to now, only a few models of asphalt for molecular simulation have been developed and each of them differs on the number of components, the fraction of components, and the type of components (mainly the asphaltene part).

Among them, three-component asphalt models were built by Zhang and Greenfield [10, 12, 13] and classified into saturates, naphthene aromatics, and asphaltenes. They proposed two models of asphalt named asphalt1 and asphalt2 and that differ only on their asphaltene part. The saturates and naphthene aromatics were represented by the docosane ($C_{22}H_{46}$), 1,7-dimethylnaphthalene ($C_{12}H_{12}$) respectively. Whereas the asphaltene part was represented by the so-called asphaltene 1 ($C_{64}H_{52}S_2$) and asphaltene 2 ($C_{72}H_{98}S$) thus, representing the asphalt1 and asphalt2 model respectively. The asphaltene 1 is taken from Nuclear Magnetic Resonance (NMR) studies by Artok *et al.* and has a large aromatic core and few side chains. While the asphaltene 2 came from the fluorescence depolarization studies of Groenzin and Mullins [61] has few rings and larger branches.

They have chosen the overall mixture composition of asphalt based on measurements by Storm and collaborators [59]. An asphaltene mass fraction of 21 % was selected, 20 % of naphthene aromatics, and 59 % of saturates. The concentrations of the docosane and 1,7-dimethylnaphthalene were chosen based on the "alkane:aromatic" carbon ratio (72.2:27.8 or 8:3) of the oil components reported by Storm *et al.* [60]. In the asphalt1 model, 5 molecules of asphaltene 1, 27 molecules of 1,7-dimethylnaphthalene, and 41 molecules of docosane were used. The asphalt2 model is composed of 5 molecules of asphaltene 2, 35 molecules of 1,7-dimethylnaphthalene, and 45 molecules of docosane. The overall composition of molecules in both asphalt models is shown in Table 2.1.

A more complex model was developed later by Zhang and Greenfield [14, 62] using

Table 2.1: Overall composition of mixtures of asphalt1 and asphalt2 [10]

	mixture	number of molecules	mass fraction
asphalt1	asphaltene 1	5	20.7
	1,7-dimethylnaphthalene	27	19.7
	docosane	41	59.6
asphalt2	asphaltene 2	5	21.1
	1,7-dimethylnaphthalene	30	19.8
	docosane	45	59.1

a six-component model targeted toward the elemental ratios found in the SHRP core asphalt AAA-1 (Canadian/Lloydminster): Asphaltene 2, docosane, 3 types of polar aromatic (Ethylbenzothiophene, 3-pentylthiophene, and 7,8-benzoquinoline) and Ethyltetralin (naphthene aromatics) were used. Computer simulations were used to combine chemicals that form asphalt-like mixture whose physical properties are predicted to be representative of SHRP core asphalts. Compared to their previous three-component model, the density and thermal expansion coefficient of the six-component AAA-1 model agreed better with experimental data [63].

To improve further the previous models, a twelve-component molecular model of asphalt was proposed by Li and Greenfield [64]. This model asphalt contains 3 types of asphaltenes, 2 types of saturates, 2 types of naphthene aromatics, and 5 types of polar aromatics to represent the Canadian/Lloydminster AAA-1, Venezuelan/Boscan AAK-1, and USA/West Texas AAM-1 crude oils sources from SHRP [14]. The characterizations of the models' asphalt systems matched elemental analyses, molecular classes, and components found in the SHRP asphalt cores. The AAA-1 model has a mass fraction of [10.7:30.8:41.9:16.6] for the saturates, aromatics, resins, and asphaltene respectively compared to the experimental value [10.6:31.8:37.3:16.2]. The densities of the AAA-1 model asphalt system were closer to experimental data [63] compared to previous model systems.

2.3 Physical properties of asphalt

In this section, we review the physical properties of the different asphalt molecular models realizable at the atomic level (nanoscale level) and that strongly affect overall highway

performance and durability. Macroscopic level or highway level properties, such as cracking, require additional information about road design and structure and, therefore, can not be computed using molecular simulation. The properties of interest to highway usage of asphalts that may be investigated at the molecular level are among others: *i*) The density which is a basic property of a material defined as the ratio of the mass over the volume; *ii*) asphalt stiffness or bulk modulus which is a measure of its stress-strain behavior; *iii*) isothermal compressibility which is the inverse of the bulk modulus and is related with the cohesion loss within asphalt; *iv*) viscosity which measures the resistance of the asphalt to gradual deformations caused by shear or tensile stress.

Wang *et al.* [17] performed MD simulations using the LAMMPS package [65] with the consistent valence force field (CVFF) [66] to study the thermodynamic properties of the two asphalt models suggested by Zhang and Greenfield [12]. The properties of interest were density, thermal expansion coefficient, isothermal compressibility, and bulk modulus. Five different temperatures (-35, -5, 25, 85, and 170 ^{o}C) were simulated to analyze the variation of thermodynamic properties with the temperature. In all the simulations, the densities were calculated at 1 atm pressure using the constant pressure and temperature (NPT) ensembles with 3D periodic boundary conditions. The result of their simulations showed similar trends in the density, bulk modulus, isothermal compressibility, and thermal expansion coefficient compared to the Zhang and Greenfield [12] results. However, the densities for both asphalt models were slightly smaller than the results from Zhang and Greenfield [12]. Whereas the isothermal compressibility was slightly lower and the corresponding bulk modulus was slightly greater than the results obtained by Zhang and Greenfield [12].

Yao *et al.* [18] have used MD and experimental studies using the Amber Cornell Extension Force Field (ACEFF) [67], canonical ensemble (NVT ensemble), and isothermal-isobaric ensemble (NPT ensemble) at 1 atm pressure and 298.15 K temperature. They simulated the asphalt1 model of the common three-component by Zhang and Greenfield [12, 13], and predict the physical properties of asphalt material including density, glass transition, viscosity, and the bulk modulus. The viscosity of the molecular asphalt model was calculated using the Muller-Plathe algorithm [68]. The bulk modulus of the molecular asphalt model was determined and obtained by applying the infinitesimal strain in the model boundaries. They found the asphalt model's physical properties were closer to the laboratory testing data [24, 69]

compared to the reference work from Zhang and Greenfield [12].

2.4 A review on asphalt nano additives and silica nanoparticles

Few works were already done combining the asphalt models interacting with nanomaterials at the molecular simulation level [70, 71, 17, 72]. These studies are based on nanoparticles' interaction properties with asphalt, including interfacial adhesion of silica with the fluid. Among them, Yao *et al.* [70] have simulated the three-component asphalt binder and modified asphalt with exfoliated multi-layered graphite nanoplatelets (xGNP). Using the MD, they analyzed the mechanical properties of the systems, such as density and bulk modulus. It was found the density and bulk modulus of the xGNP modified asphalt binder model was higher than that of the neat one.

Xu *et al.* [71, 73] investigated the interaction energy and the work of adhesion on asphalt-silica and asphalt-calcite aggregate interface model. Also, Du and Zhu, in their work[72], analyzed the interaction mechanism of asphalt with the mineral surface. Five types of mineral aggregates were considered in that work, including MgO, CaO, Al_2O_3, Fe_2O_3, and SiO_2. Another study was conducted by Long *et al.* to investigate the interface adhesion of nano-silica modified asphalt mixtures [74]. The modified nano-silica asphalt was built at the ratio of [9.7:27.9:38.1:15.1:9.2] for the saturates, aromatics, resin, asphaltenes, and nano-silica respectively. The authors found the density increases with the oxidation level, and the nano-silica reduces the susceptibility of the asphalt mixture to moisture-induced damage.

Besides, experimental studies were done to investigate the improvement of the abrasion resistance and flexural fatigue of asphalt pavement with SiO_2 nanoparticles (NPs) [21, 22, 20]. It was found that the abrasion resistance and the flexural fatigue performance of the asphalt mixture containing nanoparticles improved as the abrasion resistance of asphalt mixture increases with compressive strength.

In their works, Miranda *et al.* [26, 27, 28, 29, 30, 31] developed several studies involving the use of hydroxylated silica nanoparticles in interfaces of interest to the Oil & Gas industry. As a natural extension of these investigations, given the advantages of synthesis, cost, and

stability, we shall use hydroxylated SiO_2-NPs to represent the ideal aggregate of asphalt in MD simulation and study their effects on the thermodynamic and mechanical properties of the asphalt model. The mechanical properties of modified asphalt with SiO_2-NPs have not yet been studied with MD simulations. This approach may predict the asphalt's thermodynamic and mechanical properties resulting from specified interactions and structures at the molecular level. Thus correlating the fluid physical properties to the macroscopic properties for engineering applications. This work investigates the effects of hydroxylated SiO_2-NPs on the thermodynamic and mechanical properties of asphalt through MD simulations.

CHAPTER 3

COMPUTATIONAL METHODS

Because of the complexity of asphalt, to describe this material from the nano to the macro-scale, the use of complementary methodologies becomes necessary. At the most fundamental level, we have the first-principles calculation, which is based on very strict physical laws, such as quantum mechanics and statistical mechanics, and does not need any experimental data beforehand, except atomic numbers and electronic configurations.

To investigate the interactions by the first-principles approach, the DFT with plane waves basis set will be used. Our research group has been successfully using this procedure to describe similar systems [55, 75, 76, 77, 78]. Despite the accuracy, treating our systems completely by first principles is still prohibitive from the computational point of view. To overcome this limitation, systems will also be studied using molecular docking and MD. Molecular docking and classical MD, use computationally cheaper inter-atomic potentials, allowing us to explore larger systems and sample phase space for longer simulation times. From MD, it is possible to obtain the thermodynamic, and mechanical properties of asphalt.

3.1 Density Functional Theory and electronic structure problem

Considering a system formed by ions and electrons, the so-called many-body system, to study the properties of the system from the microscopic point of view, we need to solve the Schrödinger equation. However, the wave function in the Schrödinger equation is a complex object and the wave function methods to solve this problem are expensive. DFT can be used to solve such a problem and achieve similar results using just the electronic density rather than the wave function. DFT is a methodology widely employed to investigate the structural, magnetic, and electronic properties of atoms, molecules, and solid-state materials. In this work, we have used the DFT as implemented in Quantum Espresso. To describe the DFT method, we present first the electronic structure problem in the many-body system.

3.1.1 Electronic structure problem

Let $\mathrm{N_{at}}$ being the number of atoms or ions in a system with the mass $\{M_\nu\}_{\nu=1,2,3,\ldots,\ N_{at}}$ and charge $\{Z_\nu e\}_{\nu=1,2,3,\ldots,\ N_{at}}$. N_{el} is the number of the electron in the system with the mass m and charge -e. Then, the system can be described by the following Hamiltonian

$$\begin{aligned} H &= \sum_\nu \frac{P_\nu^2}{2M_\nu} + \sum_i \frac{p_i^2}{2m_i} + \frac{1}{2}\sum_{\nu\neq\mu} \frac{Z_\nu Z_\mu e^2}{|R_\nu - R_\mu|} + \frac{1}{2}\sum_{i\neq j} \frac{e^2}{|r_i - r_j|} - \sum_{\nu,i} \frac{Z_\nu e^2}{|r_i - R_\nu|} \\ &= T_n\left(\{P\}\right) + T_e\left(\{p\}\right) + W_{nn}\left(\{R\}\right) + W_{ee}\left(\{r\}\right) + W_{en}\left(\{R\},\{r\}\right). \end{aligned} \tag{3.1}$$

Where ν and μ are the parameter of the ions, i and j that of the electrons. p and P are the momenta of electron and ion respectively; r electron position; R ion position. $T_e\left(\{p\}\right)$ and $T_n\left(\{P\}\right)$ is the kinetic energy of the electrons and ions respectively; $W_{nn}\left(\{R\}\right)$ represent the potential energy of the ion-ion interaction and $W_{ee}\left(\{R\}\right)$ one of the electron-electron interaction; $W_{en}\left(\{R\},\{r\}\right)$ correspond to the potential energy of the ion-electron interaction.

The properties of the system can be obtained by solving the following Schrödinger equation:

$$H\left(\{r,p\},\{R,P\}\right)\Psi\left(r,R\right) = E\Psi\left(r,R\right). \tag{3.2}$$

Electrons and ions are very different:

► The mass of ions is lager order of magnitude than the mass of electrons ($M >> m$). Example of the Hydrogen atom, $M_H \approx 2000\ m_e$.

► The excitation energy of the ion is described by the phonon frequency; $\hbar\omega_{ph} \sim mev$. The excitation energy of the electron is given by the optical frequency; $\hbar\omega_{opt} \sim ev$. It is the energy to move one electron from the valence to the conduction band.

► The period of the ionic vibration is very large compared to that of the electronic excitation ; $\tau_{ph} >> \tau_{el}$ since the frequency $\omega_{el} >> \omega_{ion}$.

Therefore, the motion of the electrons is very large compared to the motion of the ions. This means that in the time scale of electronic motion, the ions can be considered static. This is the so-called Born-Oppenheimer approximation in which we consider the ion fixed and neglect the ionic dynamics in the electronic wave function. By considering this assumption, we can separate the ionic motion from the electronic one in the Schrödinger equation.

$$\Psi\left(r,R\right)=\Phi\left(r;R\right)\chi(R). \tag{3.3}$$

Then we have

$$\begin{aligned} H\Psi\left(r,R\right) &= H\Phi\left(r;R\right)\chi(R) \\ &= T_n\Phi\left(r;R\right)\chi(R)+\chi(R)\left[T_e+W_{ee}+W_{en}+W_{nn}\right]\Phi\left(r;R\right) \\ &= \Phi\left(r;R\right)T_n\chi(R)+\chi(R)\left[T_e+W_{ee}+W_{en}+W_{nn}\right]\Phi\left(r;R\right) \\ &= E\Phi\left(r;R\right)\chi(R). \end{aligned} \tag{3.4}$$

Dividing the two last equality by $\Phi\left(r;R\right)\chi(R)$, we have

$$\frac{T_n\chi(R)}{\chi(R)}+\frac{\left[T_e+W_{ee}+W_{en}+W_{nn}\right]\Phi\left(r;R\right)}{\Phi(r;R)}=E. \tag{3.5}$$

The first term on the left-hand side of the equation is a function of R, then the second term must be also a function of R as well since the right-hand side is a constant. Let us call it

$E(R)$. Then reorganizing the equations, we have;

$$\begin{cases} [T_e + W_{ee} + W_{en} + W_{nn}]\,\Phi_\alpha\,(r;R) = E_\alpha(R)\Phi_\alpha\,(r;R) \\ [T_n + E_\alpha(R)]\,\chi_{\alpha\nu}(R) = E_{\alpha\nu}\chi_{\alpha\nu}(R) \end{cases} . \tag{3.6}$$

The separation of the ionic motion to the electronic motion in the previous equations allows us to use different methods to solve the two parts. The ionic part can be treated classically for example by solving Newton's equation of motion. The electronic part can only be treated by the use of quantum mechanics. The electronic part is harder to solve, mainly due to the electron-electron interactions. This is the so-called electronic structure problem. There exist many methods to solve the electronic part such as the Hartree-Fock method and DFT. In the DFT approach, the primary equations are cast in terms of the electron density rather than the wave functions. This is possible due to the Hohenberg and Kohn theorems, discussed below.

3.1.2 Density functional theory

Density functional theory is based on the Hohenberg and Kohn (HK) theorems. Hohenberg and Kohn in their paper published in 1964 [79] have stated the following: 1) The ground state (GS) density $n(r)$ can solely determine the properties of a system. 2) There is a functional of the density $F[n(r)]$ that satisfies a variational principle for the GS energy.

We want to solve the electronic part of Equation 3.6

$$[T_e + W_{ee} + W_{en} + W_{nn}]\,\Phi\,(r;R) = E_{GS}(R)\Phi\,(r;R)\,. \tag{3.7}$$

Where $E_{GS}(R)$ and $\Phi\,(r;R)$ are the ground state energy and wave function respectively which depend only parametrically on R. The last term of the left-hand side can be taken as constant and therefore put in the ionic part of Equation 3.6. By considering the system as an independent particle in an effective potential, we can rewrite the Hamiltonian as follow:

$$H_{GS} = [T_e + V_{ext}(r) + V_H(r) + V_{xc}(r)] \tag{3.8}$$

where $V_{ext}(r) \equiv W_{en}$ is the external potential, $V_H(r)$ the free-electron potential, and V_{xc} the

exchange-correlation potential ($W_{ee} \equiv V_H + V_{xc}$). Replacing Equation 3.8 into Equation 3.7, we can rewrite the Schrödinger equation as following

$$\left[T_e + V_{ext}(r) + V_H(r) + V_{xc}(r)\right] \Phi_i(r) = E_{GS}\Phi_i(r). \tag{3.9}$$

In quantum mechanics, if we have the external potential V_{ext}, we can solve the Schrödinger Equation 3.9 to find the GS wave function and then the density of the GS which is given by

$$n(r) = \sum_{i}^{N} |\Phi_i(r)|^2. \tag{3.10}$$

In the HK framework, $n(r) \longrightarrow F\left[n(r)\right] = min\langle\Phi_{GS}|\left[T_e + W_{ee}\right]|\Phi_{GS}\rangle$.

A more practical implementation of the HK is the Kohn-Sham (KS) framework [80] in which they proposed to split the functional $F\left[n(r)\right]$ into three parts so that the GS energy will be

$$E_{GS} = T_s\left[n\right] + E_H\left[n\right] + E_{xc}\left[n\right] + \int V_{ext}(r)n(r)dr. \tag{3.11}$$

Where $T_s\left[n\right]$ is the kinetic energy, $\int V_{ext}(r)n(r)dr$ the external potential, $E_H\left[n\right]$ the electrostatic energy, and $E_{xc}\left[n\right]$ the exchange-correlation energy. Equations 3.8, 3.9, and 3.10 are the so-called *Kohn Sham self-consistent equations*.

There are many methods to describe the ground state density and therefore the exchange-correlation functional part. The exact exchange-correlation functional is not known, thus, approximations are required. One common approach is to use numerical approximations to the exchange-correlation energy taken from simulations of gas of electrons. For example, the Local Density Approximation (LDA) [81] assumes that the exchange-correlation energy for a point in the crystal can be replaced by the corresponding energy for gas of electrons with the same electron density at that point as described in Equation 3.12.

$$E_{xc}[n] = \int d^3r \; e_{xc}^{hom}(n[r]). \tag{3.12}$$

Where e_{xc}^{hom} is the exchange-correlation energy of the uniform homogeneous electron-gas at the corresponding density $n(r)$. The LDA is appropriated for the slowly varying densities and fails in the case when density undergoes rapid changes.

Another class of the exchange-correlation functional are the so-called Generalized Gradient Approximation (GGA) which are more appropriated to describe molecules and systems in which density undergoes rapid changes [82]. In the GGA, the exchange-correlation energy is a functional of the gradient and electron density (see Equation 3.13). In comparison with LDA, GGA tends to improve the total energies, energy barriers, and structural energy differences. However, GGA can sometimes overcorrect the LDA.

$$E_{xc}^{GGA}[n] = \int d^3r \; f(n(r), \Delta n(r)). \tag{3.13}$$

In all the calculations in this work, the exchange-correlation revised by Perdew, Burke, and Ernzerhof (revPBE) [82, 83] was utilized. The PBE exchange-correlation energy functional was used because it corresponds to a GGA in the case of a large molecule and delocalized electrons in the uniform gas. However, the PBE functional have a mixed history of successes and failures for solids. The revPBE corrects the missing feature of the LDA in the PBE and evaluates the exchange-correlation hole surrounding an electron.

Even though the revPBE improves the original version of PBE, the functional still provides a poor description of the Van der Waals (vdW) long-range interaction. To improve this description, we modified it with vdW dispersion forces (vdW-DF) [84, 85] as it can be properly applied in the revPBE. The modified vdW-DF consist of adding a nonlocal effective core potential term to the exchange-correlation potential in order to restore the lack of vdW-DF within the GGA DFT calculations. In this method, instead of approximating the attractive long range interaction by an atom-atom interaction, the vdW-DF is modeled by an atom-electron interaction, which is represented by an appropriate effective atom-centered nonlocal potential obtained from an optimization process.

To solve the Kohn-Sham self-consistent equations for real systems, we need to expand the KS orbitals in terms of a basis set, and treating the core electrons can be computationally expensive, therefore we have used further approximations:

1) Choice of the basis set and cutoff

We have used plane waves to describe the delocalized electrons in solids with periodic boundary conditions [86]. To describe this problem, we use Bloch's theorem [87, 88] which

allow writing the wave function as the combination of the plane wave function as given in Equation 3.14:

$$\Phi_n(r) = u_n(r)e^{ik.r}. \tag{3.14}$$

Where k is the wave vector in the first Brillouin zone and the periodic condition $u_n(r+R) = u_n(r)$ with R been the Bravais lattice vector. In general (numerically), the problem is described in term of the reciprocal lattice (reciprocal space) rather than Bravais lattice as follow

$$u_n(r) = \sum_G c_n e^{iG.r}. \tag{3.15}$$

Where c_n are plane wave coefficients and G the reciprocal lattice vectors. Replacing Equation 3.15 into Equation 3.14, the wave function can be rewritten in terms of the reciprocal lattice as

$$\Phi_n(r) = \sum_G c_n e^{i(k+G).r}. \tag{3.16}$$

Bloch's theorem allows us to replace the integrals in real space with integrals over the reciprocal space vectors within the first Brillouin zone. In practice, we have to choose a cutoff such as only a certain number of plane waves will be evaluated. This allows us to reduce the computational cost. The energy cutoff satisfies the following inequality:

$$\frac{\bar{h}^2}{2m}|k+G|^2 \leq E_{cut} \tag{3.17}$$

2) Pseudopotential

The valence electrons are the ones that contribute directly to the chemical bonds and the electronic properties of the system whereas the core electrons near the nuclei do not. Therefore to describe the screening effect imposed by the core electrons to the valence ones, we have used the pseudopotentials [89].

A good choice of pseudopotential has to be made in order to lower the computational cost and provide an accurate description of the system. In this work, we used Vanderbilt's ultrasoft pseudopotential [90]. Vanderbilt's method to build ultrasoft pseudopotential is very useful for our system because it decreases the set of plane waves used and therefore reduces the calculation time. This pseudopotential is used to replace the exact all-electron wave function

with a suitable "soft" pseudo wave function and thereby describe the scattering properties of the core electrons near the nuclei.

3.2 Classical Molecular Dynamics Simulations

In classical MD, we do not have information about the electronic structure, however, we can access thermodynamic properties of the system and not just GS properties. The idea behind MD is to integrate the equations of motion to obtain the trajectories and velocities of all atoms. The equations of motion are given by the classical Newton's equation

$$a_i(t) = \frac{F_i}{m_i} = \frac{\partial v_i(t)}{\partial t} = \frac{\partial^2 r_i(t)}{\partial t}. \tag{3.18}$$

Where $a_i(t)$, F_i, and m_i are the acceleration at time t, the force acting on the atom i and the mass of the atoms i respectively; $v_i(t)$ and $r_i(t)$ are the velocity and position of the atoms i at time t respectively. The forces in the Newton equation of motion 3.18 are defined by the potential energy as follow

$$F = -\nabla U(r_1, r_2, ..., r_N). \tag{3.19}$$

Where $U(r_1, r_2, ..., r_N)$ is the combination of intramolecular and intermolecular potentials. The potential $U(r_1, r_2, ..., r_N)$ of the system of N atoms with an interaction described by an empirical potential can be expanded in many-body terms 3.20:

$$U(r1, r2, ..., rN) = \sum_i U_1(r_i) + \sum_{i,j} U_2(r_i, r_j) + \sum_{i,j,k} U_3(r_i, r_j, r_k) + ... \tag{3.20}$$

where U_1 is the one-body term, due to an external field or boundary conditions; U_2 is the two-body term or pair potential. The interaction of any pair of atoms depends only on their spacing and is not affected by the presence of other atoms. U_3 is the three-body term that arises when the interaction of a pair of atoms is modified by the presence of a third atom. For a many-body system, Equations 3.18, 3.19 became difficult to solve analytically and can be solved by numerical methods.

Using finite difference methods, the acceleration can be combined with information on the current and previous atomic positions and velocities to predict the position of each atom at an

infinitesimal time interval Δt. This requires an integration algorithm to generate trajectories (positions and velocity) and update energy. We have used the Velocity Verlet algorithm [91] in which the position and velocity of atom i at time $t + \Delta t$ are determined using the second-order Taylor expansions:

$$\begin{aligned} r_i(t + \Delta t) &= r_i(t) + v_i(t)\Delta t + \frac{1}{2}a_i(t)dt\Delta t^2 \\ v_i(t + \Delta t) &= v_i(t) + \frac{1}{2}[a_i(t) + a_i(t + \Delta t)]\Delta t \end{aligned} \tag{3.21}$$

MD simulation requires atom velocities to calculate the thermodynamic, dynamic, and structural properties such as temperature, kinetic energy, pressure, etc... at each time step. We need to specify an ensemble to link the macroscale (statistical mechanics) of the system to the nanoscale or atomistic scale. This link can be established because the time averages are equivalent to the statistical ensemble averages of the system due to the ergodic hypothesis. In this work, the Canonical Ensemble (NVT ensemble) and Isothermal-isobaric Ensemble (NPT ensemble) were used to bring the system to equilibrium and calculate the average properties of the system.

Since the natural ensemble provided by the integration of Equation 3.18 is the microcanonical ensemble in which the total number of particles (N), the volume (V), as well as the total energy (E) in the system are conserved, we need to couple our system to an external bath to simulate in the NVT and NPT ensembles. The thermal bath is called thermostat and give or take energy to the system in order to maintain the temperature (T) constant. To maintain the pressure constant, the box size fluctuates according to a barostat. Details of the used thermostat and barostat are given in Chapter 5.

In this work, calculations of classical MD will be performed using the Large-scale Atomic/Molecular Massively Parallel Simulator (LAMMPS) software [65] where the interactions of silica nanoparticles and the hydrocarbons that make up the asphalt will be investigated. To use the MD method, we have to define the rules that are governing the interaction of atoms in the system. These rules are often expressed in terms of potential functions also called Force Field.

3.2.1 Force Field

The Force Field is a mathematical function used to describe the interatomic potential and compute the potential of a system of atoms or molecules. It describes how the total potential energy of a system of N atoms depends on the coordinates of the atoms. In molecular mechanics, the interactions of the system can be grouped into bonded and non-bonded interactions as shown in Equation 3.22.

$$U(r1, r2, ..., rN) = E_{bond} + E_{non-bond}. \tag{3.22}$$

The bonded term includes the bond lengths, bond angles, and torsion angles. While the terms for non-bonded interaction are the van der Waals, electrostatic, and other interactions. Several force fields have been developed to simulate molecular systems, such as the AMBER, CHARMM, OPLS-AA, CVFF, PPPM, and COMPASS [52, 53, 92, 67, 93, 66, 94] force fields. Depending on the force field, different potential functions and parameters are used for each atom type.

The correct description of atomic interactions through effective potentials needs to be used to ensure accurate results from simulations. In this thesis, the CHARMM force field [94] is used to describe the interactions of atoms in the asphalt. The functional form of the CHARMM Force Field is shown in Equations 3.23, 3.24, and 3.25.

$$U(r_1, r_2, ..., r_N) = U_{bond} + U_{ang} + U_{di} + U_{LJ} + U_c. \tag{3.23}$$

The interactions between chemically bonded nearest neighbors are handled by the bonded energy terms which are: the bond stretching U_{bond}, angle bending U_{ang}, and dihedral energy terms U_{di} giving in Equation 3.24.

$$\begin{aligned} U_{bond} &= \sum_{r} K_r(r - r_0)^2 \\ U_{ang} &= \sum_{\theta} K_\theta(\theta - \theta_0)^2 \\ U_{di} &= \sum_{\phi} K_\phi(1 + cos(n\phi - \delta)). \end{aligned} \tag{3.24}$$

The interactions beyond nearest neighbors are represented by the non-bonded energy terms: Lennard-Jones U_{LJ} and Coulomb U_c interactions in Equation 3.25.

$$U_{LJ} = \sum_{ij} 4\epsilon \left[\left(\frac{\sigma}{r_{ij}} \right)^{12} - \left(\frac{\sigma}{r_{ij}} \right)^{6} \right]$$
$$U_c = \sum_{ij} \frac{q_i q_j}{\epsilon r_{ij}}. \tag{3.25}$$

The values of the various force constants $r_0,\ \theta_0,\ \delta,\ K_r,\ K_\theta,$ and K_ϕ, as well as partial charges q_i, and the Lennard-Jones parameters σ, ϵ are taken from the last version of the CHARMM General Force Field (CGenFF) [95, 96].

To describe the interaction of the atoms in the SiO_2 nanoparticles, we employed the CHARMM-based interatomic potential by Cruz-Chu *et al.* [97]. In the Cruz-Chu potential, the bonded parameters are taken from the work of Hill Jörg-R. and Sauer Joachim [98] and adjusted to fit the terms CHARMM Force Field. Whereas the nonbonded parameters are optimized based on the macroscopic wetting properties of amorphous silica surfaces. Details of the Force Field's parameters are given in Appendix A.

3.3 Molecular docking simulation

Molecular Docking is a molecular modeling technique that predicts the conformation of a small molecule bound to a macromolecule with a substantial degree of accuracy [99]. This technique is based on simulation which aims to achieve optimized conformation of the molecules, and it can be used to model the interaction between two molecules at the atomic level. Docking is a growing field applying to biological molecules and pharmaceutical research. Docking is widely used in the literature for systems such as enzymes, proteins, and drug discovery [100, 101, 102, 103]. However, docking can be well used for the macro-molecule system in materials science and chemistry. In this thesis, we have explored the docking methodology for the first time in asphalt materials.

Barry L. Stoddard and Daniel E. Koshland [101] reported substrates analysis of isocitrate dehydrogenase, where isocitrate and derivatives were docked to the crystallographic structure of an isocitrate-Mg2'-enzyme complex using AutoDock software [102]. Docking of isocitrate

yielded several conformations, placing the three similar carboxyl groups in favorable hydrogen-bonding sites. The lowest energy conformation matched the observed electron density for isocitrate. Since the electron density was reported as somewhat ambiguous, so this result was used as validation of their choice of isocitrate binding conformation. Docking of D-malate yielded one conformation of higher energy: -36 kcal/mol for D-malate vs -92 kcal/mol for the best isocitrate conformation. These energies were closed to the experimental values, suggesting that AutoDock may be a valid method for ranking similar molecules relative to one another.

Morris *et al.* [102] showed that even for ligands with a large number of degrees of freedom, root-mean-square deviations (rmsd) of less than 1 Å from the crystallographic conformations can be obtained for the lowest-energy dockings. They used AutoDock 4.2 to test benzamidine binding to β-trypsin. There were no torsional degrees of freedom. 100 % of the docked conformations found the crystallographic conformation. They found that the lowest energy docked conformation had an energy of -51.01 kcal/mol and a rmsd of 0.23 Å, and an energy of about 4 kcal/mol lower than that of the crystal structure (-47.27 kcal/mol). They tested also camphor binding to cytochrome P-450 cam. Camphor is a fused-ring system, so it was docked as a rigid body and, therefore, clustered into the same rank. However, this cluster contained two sub-clusters, one contained 76 members and matched the crystallographic conformation with the lowest energy -36.95 kcal/mol and rmsd from the crystallographic coordinates of 0.95 Å, while the other contained 24 members and placed the carbonyl oxygen in the correct hydrogen-bonding position, but rotated the cage-like body of the molecule by 180 °C.

Julie R. Schames and Richard H. Henchman [103] studied the docking of the 5CITEP inhibitor to snapshots of a 2 ns HIV-1 integrase. HIV-1 integrase (IN) is the enzyme responsible for the integration of viral DNA into the host genome, and it represents a promising and yet unexploited target for the treatment of HIV infection. Combining molecular dynamics with flexible-ligand docking, they have shown the existence of a new and possibly important binding region, the trench. This open protein conformation was noted in a majority of the snapshots, suggesting that it is energetically stable. The energy was ranking from -13 kcal/mol to -8 kcal/mol.

In our work, we examined molecular docking strategies to minimize and evaluate the binding energy and then, select the optimal conformations of the asphaltene nanoaggregates. Molecular docking is based on two ingredients which are the scoring function and the search

algorithm. The docking assessment and reliability have a link within these ingredients.

3.3.1 Scoring function and energy evaluation

The scoring function is a class of methods that are employed in docking to evaluate the interactions between molecules [104]. In this work, we use the force-field-based scoring function to simulate asphaltene nanoaggregation. It is based on the assumption that the change in the binding free energy (ΔG_{bind}) of the small molecule (the one that is being inserted) to its target macromolecule can be decomposed into a sum of individual free energy contributions as follow

$$\Delta G_{bind} = \Delta G_{vdw} + \Delta G_{hbond} + \Delta G_{elec} + \Delta G_{conform} + \Delta G_{tor} + \Delta G_{desolv}. \tag{3.26}$$

Where the first four terms are Van der Waals dispersion/repulsion (ΔG_{vdw}), hydrogen bonding (ΔG_{hbond}), electrostatics (ΔG_{elec}), and deviations from covalent geometry ($\Delta G_{conform}$) respectively. ΔG_{tor} represents the restriction of internal rotors and global rotation and translation (torsional free energy), and ΔG_{desolv} is the desolvation upon binding and the hydrophobic effect (solvent entropy changes at solute-solvent interfaces).

The binding energy can be understood as the energy difference between bound and unbound state based on a structured ensemble including six pairwise potentials (V) and an estimation of the conformational entropy lost upon binding (ΔS_{conf}) as given in Equation 3.27

$$\begin{aligned}\Delta G_{bind} = (V^{S-S}_{bound} - V^{S-S}_{unbound}) + (V^{M-M}_{bound} - V^{M-M}_{unbound}) \\ + (V^{M-S}_{bound} - V^{M-S}_{unbound} + \Delta S_{conf}).\end{aligned} \tag{3.27}$$

Where S and M represent respectively the small molecule and macromolecule. The term for the loss of torsional entropy upon binding (ΔS_{conf}) is directly proportional to the number of rotatable bonds in the molecule (N_{tors}):

$$\Delta S_{conf} = W_{conf} N_{tors}. \tag{3.28}$$

The weighting constants W_{conf} is optimized to calibrate the empirical free energy based on

a set of experimentally characterized complexes. Each of the pairwise energetic terms in Equation 3.27 includes evaluations for dispersion/repulsion, hydrogen bonding, electrostatics, and desolvation with the parameters taking from the general AMBER force field describes by the following equation:

$$E_{AMBER} = \sum_{bonds} K_r(r - r_{eq})^2 + \sum_{angles} K_\theta(\theta - \theta_{eq})^2 + \sum_{dihedral} \frac{V_n}{2}\left[1 + \cos(n\phi - \gamma)\right] + \sum_{i,j}\left(\frac{A_{ij}}{r_{ij}^{12}} + \frac{B_{ij}}{r_{ij}^{6}} + \frac{q_i q_j}{\epsilon(r_{ij}) r_{ij}}\right). \tag{3.29}$$

where K_r, r_{eq}, K_θ, θ_{eq}, V_n, n, γ, A_{ij}, and B_{ij} are the empirical parameters of the system which are obtained either from fitting to experimental data or ab initio data. r, θ, and ϕ refer respectively to the distance, angle, and torsional angle between atoms. r_{ij} stands for the distance between macromolecule atom i and small molecule atom j and q_i and q_j are the atomic charges. We consider the macromolecule as fixed, so its bound state is identical to the unbound state and the difference in their intramolecular energy being zero.

3.3.2 Search algorithm: Genetic and Lamarckian genetic algorithm

The search algorithm is used to explore the potential energy surface and search for a putative global minimum free energy. In our work, we have used AutoDock (which is free software that automated docking of small molecules to macromolecules) as implemented in AutoDockTools (ADT) [102, 105, 106] graphical user interface. There are three search methods incorporated in ADT: Monte Carlo simulated annealing, genetic algorithm (GA), and the Lamarckian genetic algorithm (LGA). We have used the LGA for our simulation because is pointed to as the most efficient, reliable, and successful method for docking [107].

A genetic algorithm is a heuristic search that is inspired by Charles Darwin's theory of natural evolution. This class of algorithms reflects the process of natural selection where the fittest individuals are selected for reproduction in order to produce offspring of the next generation. LGA is a search heuristic that is inspired by Lamarck's theory of evolution.

Lamarck is best known for his theory of inheritance of acquired characteristics, which asserts that phenotypic characteristics acquired during an individual's lifetime can become heritable traits. A classical implementation of the GA (respectively LGA) can be subdivided into 4 (respectively 5) steps as shown in Figure 3.1.

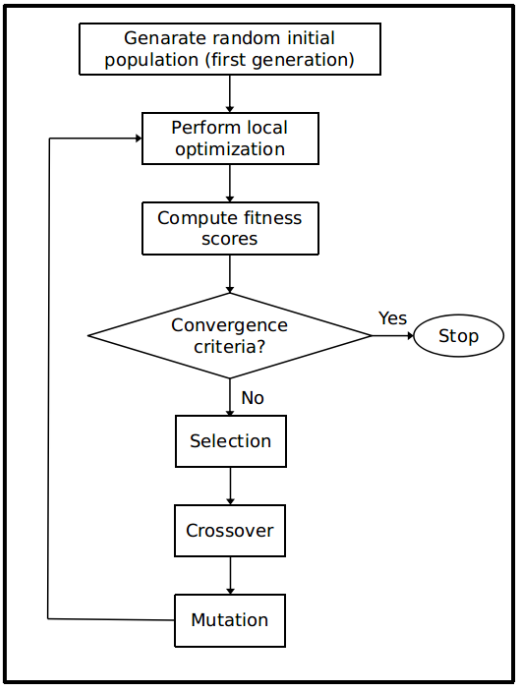

Figure 3.1: Steps describing pseudocode of the Lamarckian genetic algorithm

1) Initial population

A set of individuals (called chromosomes) carrying a gene, are selected to form the initial population (first generation). The population is randomly chosen and has a defined size denoted by the keyword `ga-pop-size`. The small molecule state variables (translation $x_i,\ y_i,\ z_i$, orientation/rotation $\alpha_x,\ \alpha_y, \alpha_z, \theta$, and conformation/torsion ω_j) correspond to a gene and the atomic coordinates represent the chromosome [107].

2) Lamarckian adaptation

The Lamarckian adaptation (or the inheritance of acquired characteristics during the lifetime) consists of making a local search in a proportion of the population in each generation

before starting the global search (the GA). In AutoDock, the local search is based on the Solis and Wets local search method [108, 109]. The maximum number of iteration of Solis & Wets local search is defined by the keyword `sw-max-its` and the probability of performing a local search on the individual is denoted by the keyword `ls-search-freq`.

3) Fitness function and selection

This step consists of computing the free energy (fitness score) of each individual, and then select a number of individuals based on their fitness scores. A total number of free energy defined by the keyword `ga-num-evals` may be computed to achieves convergence. Here, the fitness score corresponds to the free energy evaluation of each individual. The individuals that have energies lower than the average energy are then selected. The amount of the individuals to be selected is given by the keyword `ga-crossover-rate`.

4) Crossover and mutation

The crossover corresponds to a fraction of the selected individual (in the previous step) in which there is gene transfer. The proportion of the population defined by the keyword `ga-crossover-rate` will exchange their gene. The crossover and mutation are performed on a randomly chosen individual. The mutation is applied by adding to the gene that has undergone crossover (denoted by the keyword `ga-mutation-rate`), a random real number that has a Cauchy distribution of the following form $C(\alpha, \beta, x) = \beta/(\beta^2 + (x - \alpha^2)^2)$.

5) Population restructuring with new generations

This step consists of reconstructing a new population (generation) by evaluating the free energy of the individuals mutated and replace them in the population by killing the same number of individuals that have the smallest fitness score (highest free energy). The algorithm will run until the convergence criteria (either the total number of the energy evaluation or the number of the generation defined by the keyword `ga-num-generation`) is reached. The parameters of the keywords used in our work can be found in Section 4.2 of Chapter 4.

CHAPTER 4

SIMULATION OF ASPHALTENE NANOAGGREGATION

4.1 Introduction

Asphalt is a material of ancestral origin, however, there are several disagreements as to its composition, in particular asphaltene structures. Asphaltene is the crude oil part that is insoluble in n-alkanes such as heptane and soluble in aromatic solvents such as toluene. Its composition includes polyaromatic and polycyclic rings with heteroatoms such as sulfur, nitrogen, and oxygen. Asphaltenes are challenging molecules because they have no exact structure and it is often difficult to establish the slight difference between them. Several models of asphaltenes have been proposed in the literature and the molecules used in this thesis were taking from the work of Boek *et al.* [56] .

There is a size of aggregates in which asphaltene precipitates. Due to its precipitation behavior, asphaltene builds up deposits in the pipeline and oil reservoir and thus, reduces the rate of oil extraction. The understanding of the molecular interactions in asphaltene aggregates has an important impact on the separation processes of the crude oils. It can help either to separate the lighter from the heavier part of the crude oil before the refining process or to

avoid its precipitation behavior such that the wellbore plugging and the deposit in the pipeline reservoir are refrained from. Separating the heavier parts from the lighter parts of the crude petroleum improves the rate of asphalt production and therefore, overcome the demand in asphalt pavement.

Although it is known empirically that asphaltene molecules form aggregates, there is not yet a proposal of the mechanism at the nano-level that explains such phenomenology. In this chapter, the description of the dimer to hexamer interaction of the A and R molecules was investigated in subsequent steps. Molecular Docking was used to obtain the binding free energy, the aggregates' size, and to select the more favorable conformations for further relaxation. DFT was used to analyze the energetic, electronic, and structural properties of the asphaltene nanoaggregates.

It is important to explore the different sites and elements involved in the interaction which help in the separation process of the crude petroleum. To achieve this, we have investigated the stability and the sizes of aggregates. Then, we have analyzed highest occupied molecular orbital (HOMO), the lowest unoccupied molecular orbital (LUMO), and the projected density of state (PDOS).

4.2 Computational Details

4.2.1 Molecular docking simulation

AutoDock as implemented in AutoDockTools [105, 106, 102] was used to conduct docking of of asphaltenes. The Lamarckian genetic algorithm [110] and the force-field-based scoring which took parameters from the AMBER force field [67] were used to minimize and evaluate the binding free energy. We have performed rigid docking of A and R mixtures of 2, 3, 4, 5, and 6 molecules with grid parameters $60 \times 60 \times 70$ Å^3 and the default value of the grid point spacing 0.375 Å. We did several docking trials, energies evaluation, and population to find the convergence of the search's parameters. Table 4.1 gives the details of the search parameters used for the local and global search. In total, GA run (denoted by the keyword `ga-run`) of 150 test was performed.

Table 4.1: Genetic algorithm and local search parameters.

`ga-pop-size`	150
`ga-num-evals`	2500000
`ga-num-generations`	27000
`ga-mutation-rate`	0.02
`ga-crossover-rate`	0.8
`sw-max-its`	300
`ls-search-freq`	0.06
`ga-run`	150

4.2.2 Density functional theory

The interaction mechanism in asphaltene nanoaggregates was studied using molecular docking and DFT. The combination of these two methodologies is very interesting because docking uses computationally cheaper inter-atomic potentials and can evaluate millions of local minima in a reduced time, whereas DFT explores the interaction mechanisms and the electronic properties at the atomic level although it is computationally expensive. The DFT as implemented in Quantum Espresso [111, 112] was used to investigated the electronic and structural properties of the single-molecule of A and R, and the dimers, trimers, tetramers, pentamers, and hexamers obtained from the Docking simulation.

Vanderbilt's ultrasoft pseudopotential [90] was used to describe the core region of the plane-wave functions. We used the exchange-correlation functional revised by Perdew, Burke, and Ernzerhof (revPBE) [82, 83] modified with vdW dispersion (vdW-DF) [84, 85]. Plane-wave basis set [86] and periodic boundary conditions were used. A systematic convergence study was first done to select the values of the cutoffs and cell parameters. For the monomers, dimers, and trimers, the wave function energy cutoff of 47 Ry and charge density energy cutoff of 323 Ry were used. The monomers and dimers were placed in a supercell with dimensions $(29.94 \times 23.48 \times 38.63)$ Å and $(38.63 \times 24.5 \times 30.25)$ Å respectively. The trimers, tetramers, pentamers, and hexamers were placed into an orthorhombic P cell with a minimum distance of 8.00 Å between the periodic image. In order to lower the computational cost, the wave function and charge density energy cutoff of 45 Ry and 180 Ry respectively were employed for the tetramers, pentamers, and hexamers.

To investigate the dimensions of the aggregates around the center of mass, we have

calculated the radius of gyration (R_g) as given in Equation 4.1

$$R_g^2 = \frac{1}{M}\sum_{i=1}^{N} m_i(r_i - r_{cm})^2, \tag{4.1}$$

where M is the total atomic mass of the system, r_i is the atomic position, and r_{cm} is the center of the mass coordinate of the system and m_i is the atomic mass.

To study the measure of the separation of negative and positive charges in a system, we have calculated the intensity of the electric dipole moment defined by the following Equation 4.2

$$\mu = \sum_{i=1}^{N} q_i(r_i - r_{cm}), \tag{4.2}$$

where q_i is the effective charge of the atom, which is obtained by the difference between the atomic number and the Bader electronic charge. The Charge analysis was carried out using the Bader charge analysis [113, 114, 115, 116], which is obtained by partitioning the total molecular electron density into individual atomic contributions.

We have also investigated the formation energy (E_{for}) of the aggregates which is the difference between the total energy of the aggregates (E_{tot}) and the isolated molecules' total energy E_i,

$$E_{for} = E_{tot} - \sum_i E_i. \tag{4.3}$$

4.3 Molecular docking simulation results

We used molecular docking to study the interaction mechanism of A, R, and their respective mixture. The properties of interest were the binding energy; the aggregates' size and the structure/conformation. Figure 4.1 shows how we obtained the aggregates from the molecular docking process.

We have obtained a total of three (3) conformations of the dimer, five (5) trimers, six (6) tetramer, six (6) pentamer, and six (6) conformations of the hexamer. The prime $'$ in the molecule indicates a translation and rotation of 180^o around the z-axis (system with lower energy cluster). The macromolecule is represented by the combination of the first letters and the small molecule is the last letter (either A or R molecule). Our simulation results are

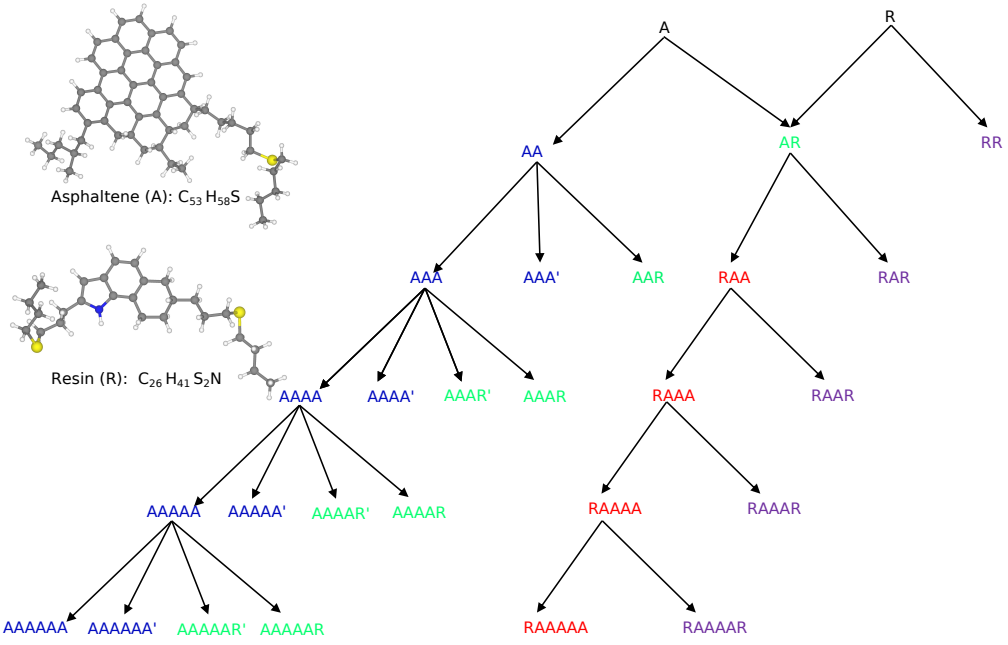

Figure 4.1: Formation process of the aggregates from the dimer to the hexamer: the blue and red color represent the aggregates with A being the small molecule and the green and purple color are the conformations with R as the small molecule.

summarized in Figure 4.2. The intermolecular distance is the measurement of the distance between the aromatic cores. Since we did not allow movement of the macromolecule, the distance between the aromatic parts in the latter remains fixed. So, in the end, the aggregate size is just the sum over the intermolecular distances between the aromatic cores in the aggregate.

All structures with A as a small molecule have similar energies whereas the ones with R as a small molecule have similar energy. The aggregates with A as a small molecule are energetically more stable than that with R as small molecules. This is related to the number of aromatic rings in the small molecule. The results also show that the structures with a larger aromatic compound have lower binding energy due to the vdW contribution to the energy. The stability of the aggregates depends on the small molecule. In general, the aggregate is more stable when the A is taking as the small molecule rather than the R.

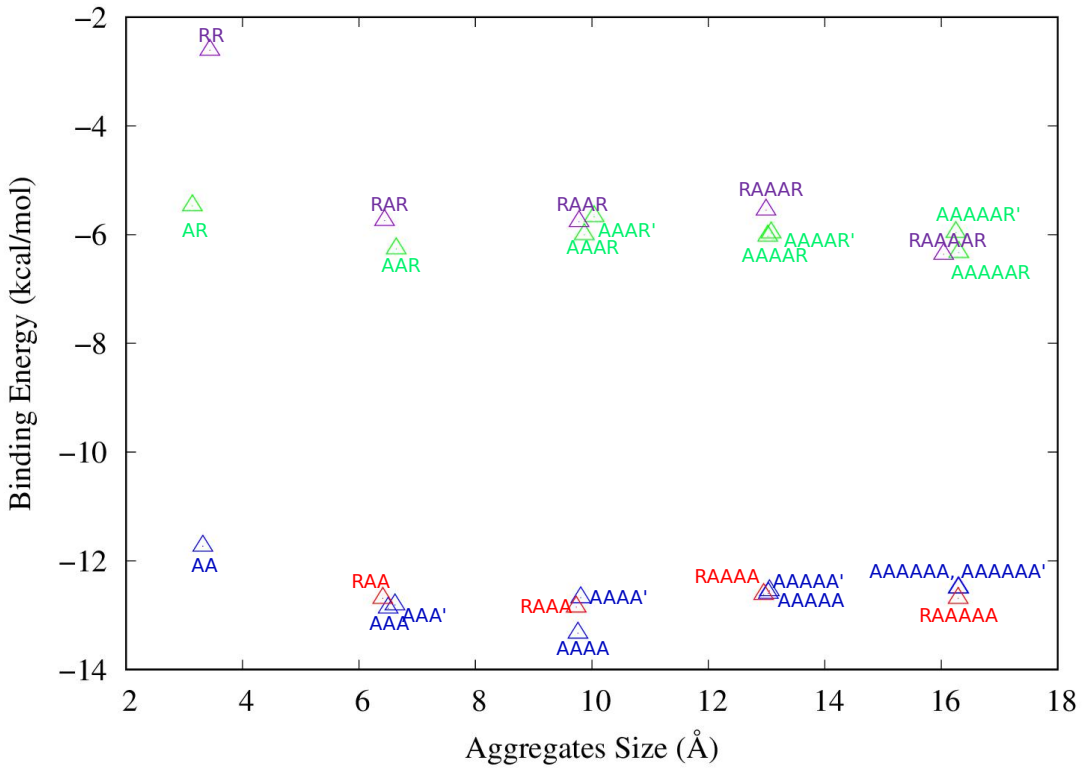

Figure 4.2: Binding energy vs aggregates size results from molecular docking: the blue and red color represents the aggregates with A been the small molecule and the green and purple color are the conformations with R as the small molecule.

The combination of A molecules shows a slight decrease in the binding energy from the dimer to tetramer owning values $-11.73\ kcal/mol$, $-12.87\ kcal/mol$, and $-13.33\ kcal/mol$ respectively as shown in Figure 4.2. Which implies the increasing stability of the aggregates from the dimer to the tetramer. The binding energies of the pentamer $-12.60\ kcal/mol$ and hexamer $-12.50\ kcal/mol$ (see Figure 4.2) in the A molecule combination are slightly different from the previous case, showing a possible disaggregation. However, the sizes of the aggregates are less than those obtained by Headen *et al.* [46, 38], which implies more stable aggregates.

In the combination of A and A' molecules, the binding energy increases from the dimer to hexamer (Figure 4.2) and remains upper than the A combination alone. In the mixture of A molecule with the R molecule, the aggregate is always more stable (lowest binding energy) when A is taking as the small molecule rather than R. For this last case, the same observation can be made as in the case of A combination alone. Our simulation results confirm that the

interactions between aromatic cores of asphaltenes are the major driving force as the binding energy decreases substantially with the number of aromatic rings (see Figure 4.2).

4.3.1 Aggregation of the dimers

We have obtained three conformations of the dimer: asphaltene-asphaltene AA, asphaltene-resin AR, and resin-resin RR. The ball-and-stick models are shown in Figure 4.3.

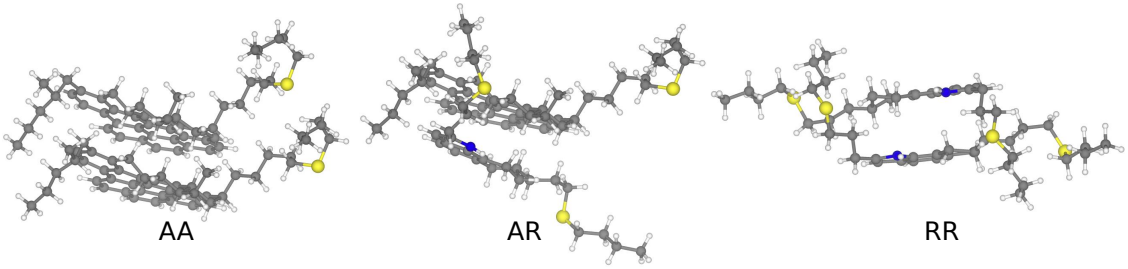

Figure 4.3: Ball-and-stick representation of the asphaltene (A) and resin (R) dimers. Atomic colors: C = gray, N = blue, H =white, and S =yellow.

The binding energy of the AA (-11.73 kcal/mol) is lower than the binding energy of AR (-5.47 kcal/mol) and RR (-2.61 kcal/mol) mainly due to the larger number of aromatic rings in the A molecule. The intermolecular distances, which are around 3.5 Å, show a good agreement with the reference work of Rogel [49, 50] although he used different asphaltene and resin structures in the solvent. Our results lead to dimers structure more stable than the one obtained by Headen *et al.* [38, 46]. They obtained AA dimer in toluene and heptane with binding energy 12.1 kj/mol and 11.9 kj/mol respectively.

4.3.2 Aggregation of the trimers

The trimers were obtained from the dimers AA and AR which are the most stable structures. We, therefore, use the latter as the macromolecule. The small molecule is A and R successively. We obtained five conformations as shown in Figure 4.4.

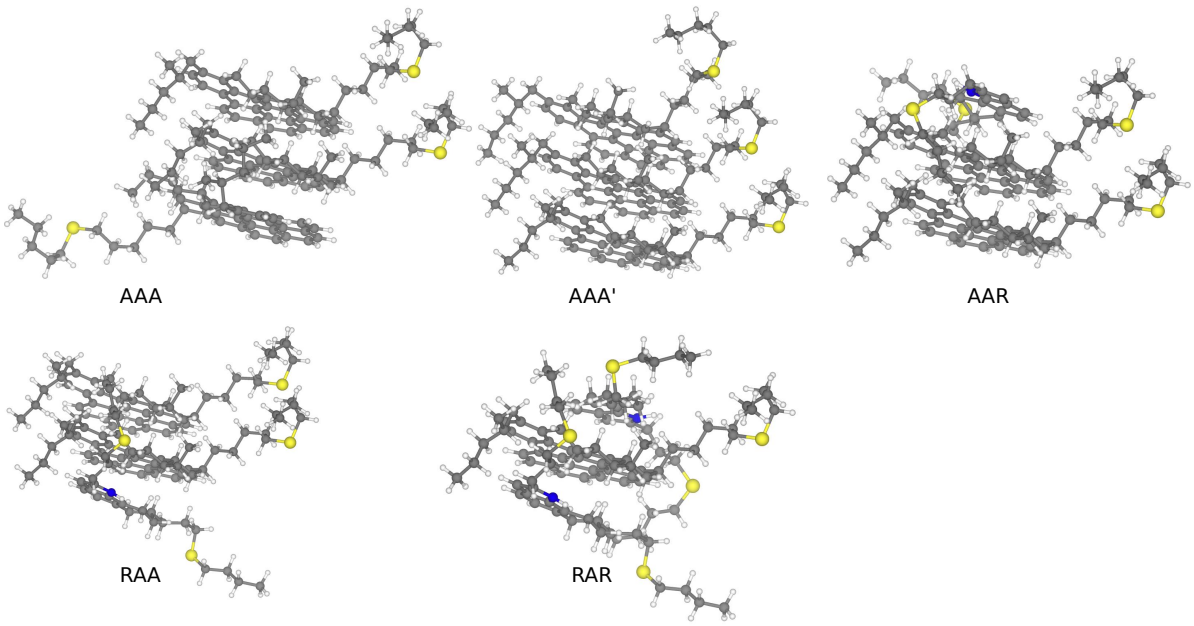

Figure 4.4: Ball-and-stick representation of the different conformations obtained from the A and R trimers with the corresponding binding energy. Atomic colors: C = gray, N = blue, H =white, and S =yellow.

Two conformations of the asphaltene-asphaltene-asphaltene aggregates were clustered. One with the lowest energy $E_B = -12.87\ kcal/mol$ name AAA in which the aromatic regions are on top of each other while the side chain of one molecule is more extended. The other one AAA' with all the sulfur chains ranging in one side having energy $E_B = -12.81\ kcal/mol$ is less stable than the previous. As in the dimer case, the AAA molecule is more stable than the RAA and RAR respectively due to the large aromatic ring. The binding energy of the AAR aggregate ($E_B = -6.26\ kcal/mol$) is greater than the binding energy of RAA ($E_B = -12.69\ kcal/mol$) because of the structure of the small molecule.

4.3.3 Aggregation of the tetramers

The tetramers were obtained from the trimer using the same procedure that we used to obtain this latest. The two most stable conformations of the trimer (AAA and RAA) were taking as the macromolecules. We obtained six (6) conformations in total (see Figure 4.5).

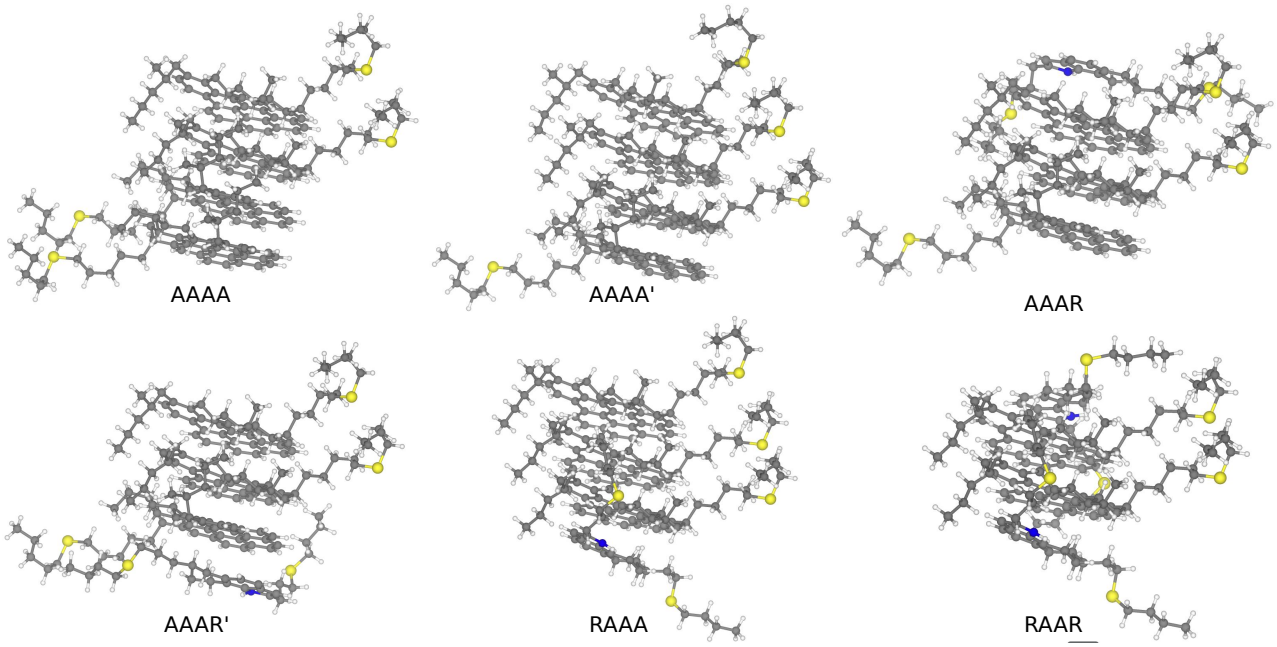

Figure 4.5: Ball-and-stick representation of the different conformations obtained from the A and R tetramer with the corresponding binding energy. Atomic colors: C = gray, N = blue, H =white, and S =yellow.

Two from the asphaltene alone, three with one molecule of resin, and the last one with two molecules of resin. The energies of the tetramers are lower than the corresponding trimer. Thus, indicating a more stable structure. Our result shows that the structures with a larger aromatic compound have lower binding energy.

4.3.4 Aggregation of the pentamers

When going to the pentamer, we start to observe a slight increase in the binding energy. However, the size of aggregates keeps values between 12.95 Å and 13.08 Å, thus remaining in

the range of the reference work [46, 50, 51]. The ball-and-stick model of all the conformations is given in Figure 4.6.

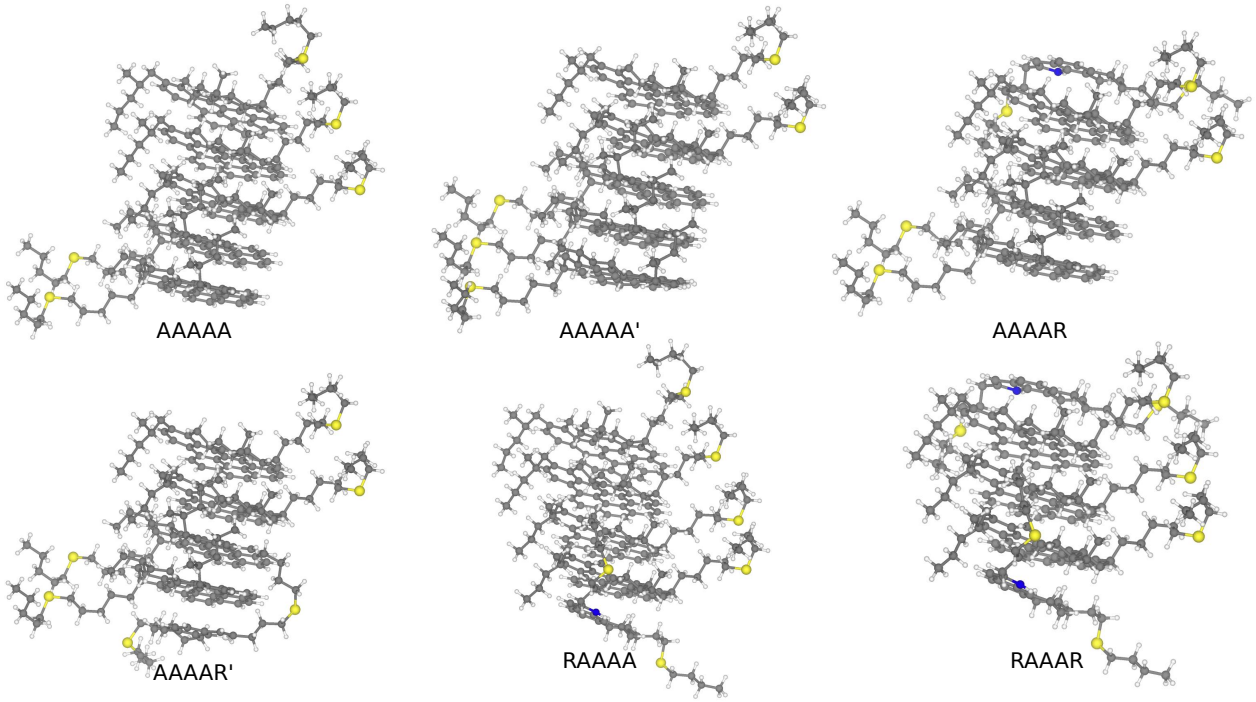

Figure 4.6: Ball-and-stick representation of the different conformations obtained from the A and R pentamer with the corresponding binding energy. Atomic colors: C = gray, N = blue, H =white, and S =yellow.

The binding energy of the pentamers AAAAA $-12.60\ kcal/mol$ and RAAAA $-12.62\ kcal/mol$ are greater than the binding energy of the tetramers AAAA ($-13.33\ kcal/mol$) and RAAA ($-12.85\ kcal/mol$) respectively from which these aggregates were built, showing a possible disaggregation.

4.3.5 Aggregation of the hexamers

As in the previous cases, we have chosen the two most energetically favorable conformations of the pentamer to build the hexamers. Figure 4.7 shows the six (6) aggregates model obtained. The binding energy of the hexamer RAAAAA ($E_B = -12.69\ kcal/mol$) is 0.19 $kcal/mol$ lower than the binding energy of AAAAAA. This shows a particular case where the resin molecule leads to a more favorable structure.

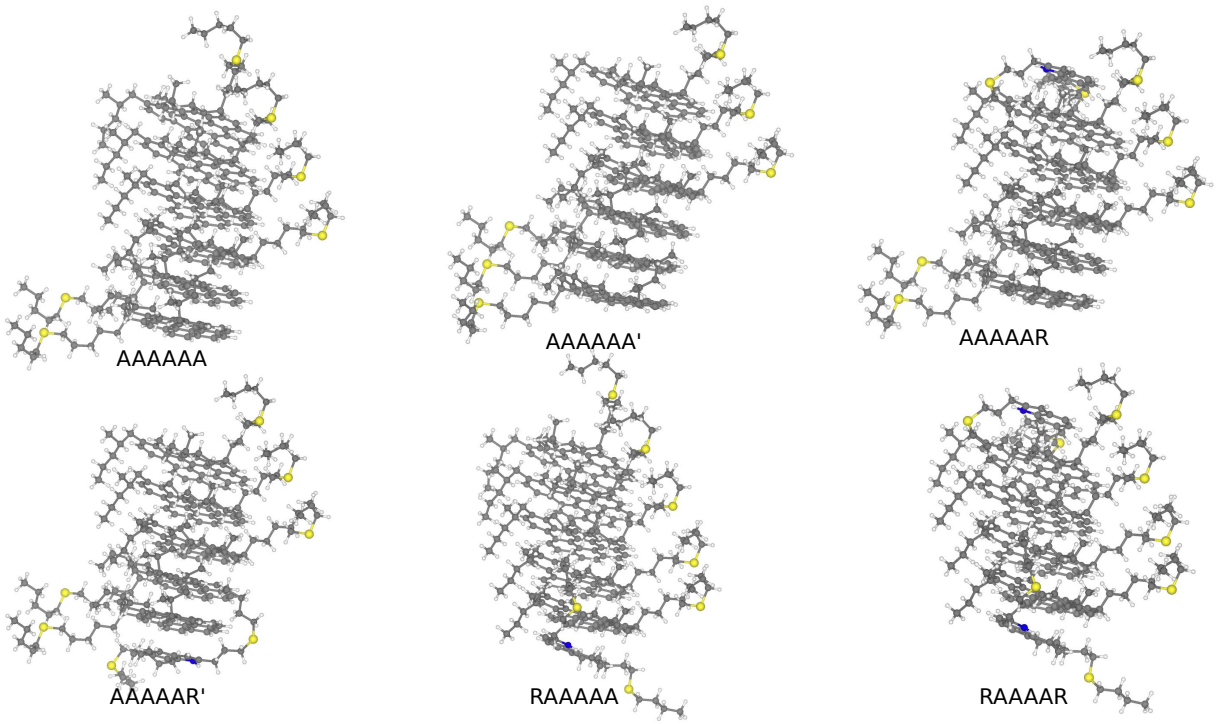

Figure 4.7: Ball-and-stick representation of the different conformations obtained from the A and R hexamer with the corresponding binding energy. Atomic colors: C = gray, N = blue, H =white, and S =yellow.

The sizes of the aggregates are smaller than those obtained by Headen *et al.* [38, 46] although they have used the same molecules in heptane and toluene. The binding energy decreased with the number of aggregates up to 4. From 5 aggregates, the binding energy seems to increase slightly, showing a possible disaggregation but does aggregate because the size of the aggregates is in the experimental range. Our simulation results confirm that the interactions between aromatic cores of asphaltenes are the major driving force for the association as the binding energy decreases substantially with the number of aromatic rings. The average intermolecular distance in the aggregates is 3.5 Å. This distance is slightly smaller than the reference value [49, 50]. The aggregates of the dimer, trimer, tetramer, pentamer, and hexamer have shown a sandwich shape with the aromatic rings on top of each other and the aliphatic arms with heteroatoms ranging in the same size. This geometry is due to the vdW stacking of the aromatic compound which leads to a good chemical representation of the aggregates.

4.4 Structural parameters: Formation energy, aggregates size, dipole moment, and radius of Gyration

To investigate the components involved in the aggregation process of asphaltene, we analyzed the energetic, electronic, and structural properties of the aggregates at the nano level. After the DFT relaxation, the aggregates remain in the sandwich configuration. The summaries of the structural parameters are presented in Figure 4.8 and Figure 4.9. The formation energy of the dimers AR ($E_F = -31.04\ kcal/mol$) and RR ($E_F = -25.85\ kcal/mol$) showed a better result than the reference value [55]. However, the formation energy of the dimer AA ($E_F = -40.44\ kcal/mol$) is slightly more positive than the one obtained by Camargo *et al.* [55] because of the initial configuration of the dimer AA which shows a difference in the bond angles.

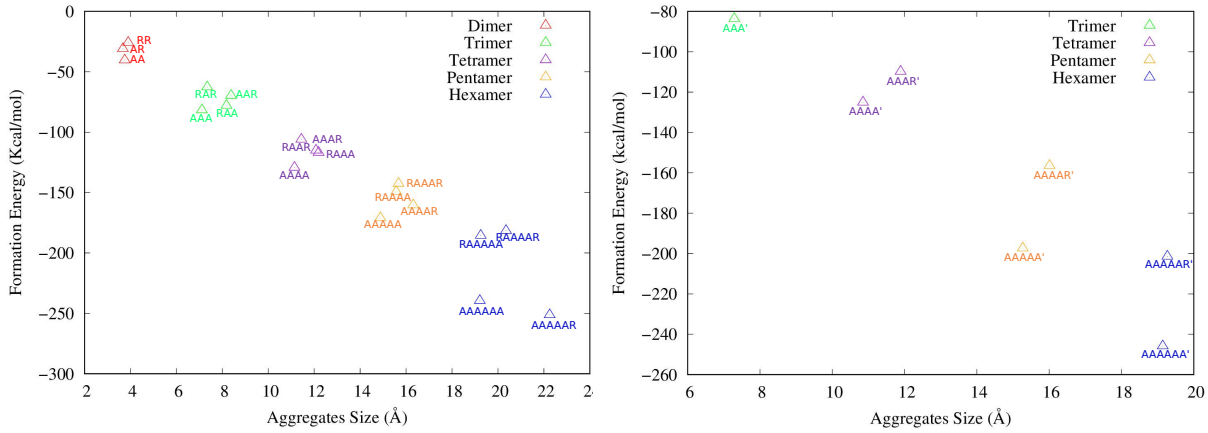

a) b)

Figure 4.8: Formation energy vs aggregates size of the dimer (red), trimer (green), tetramer (purple), pentamer (orange), and hexamer (blue) after DFT relaxation: a) systems with higher energy cluster; and b) systems with lower energy cluster.

The trimers are two times more energetically stable than the dimers. The formation energy of the AAA and AAA' are similar and smaller than that of the trimers containing the R

molecule. Regarding the tetramers, AAAA and AAAA' have similar formation energy as in the case of the trimer. The AAAR is energetically favorable than the AAAR' with a difference of 6 $kcal/mol$. We observe a remarkable difference in the formation energy of the pentamer RAAAA (-149.35 $kcal/mol$) and AAAAR (-160.41 $kcal/mol$), the hexamer RAAAAA (-185.61 $kcal/mol$) and AAAAAR (-251.34 $kcal/mol$) contrary to the case of trimer and tetramer as shown in Figure 4.8. This observation may be linked to the configurations of the aggregates. The overall analysis shows that the presence of the R molecule lower the stability of the aggregate as the systems with two R are energetically less favorable than others.

The aggregates' sizes of the system after the relaxation with DFT in Figure 4.8 show that the intermolecular distances slightly increased compared to the docking results with an average distance being 3.7 Å. However, remain in the experimental range [49, 50]. The intermolecular distances of the AA, AR, and RR were optimized to 3.75 Å, 3.67 Å, and 3.80 Å respectively. Our results show that the structures are more bounded than those obtained by Camargo *et al.* [55], with the same asphaltene and resin molecules.

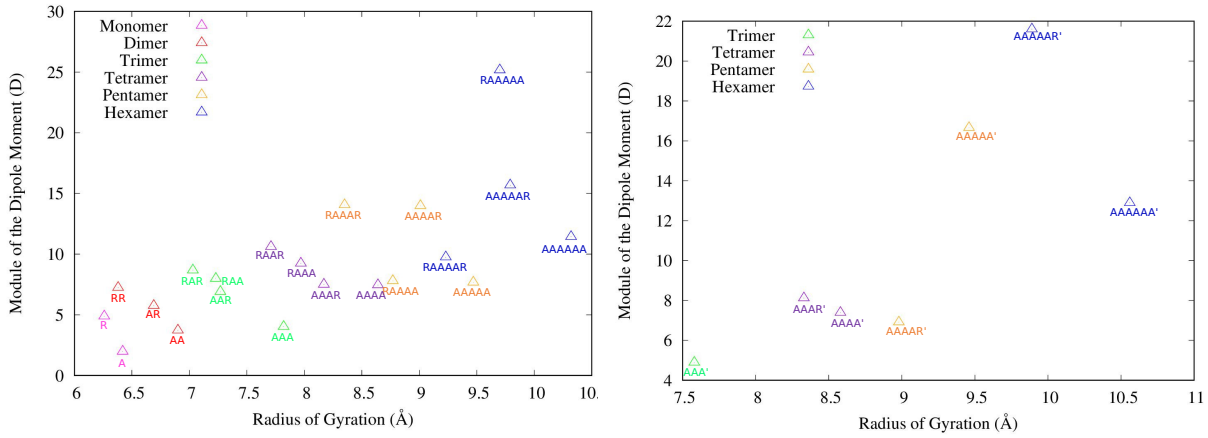

a) b)

Figure 4.9: Module of the dipole moment vs radius of Gyration of the monomers (pink), dimer (red), trimer (green), tetramer (purple), pentamer (orange), and hexamer (blue) after DFT relaxation: a) systems with higher energy cluster; and b) systems with lower energy cluster.

The dipole moment in Figure 4.9 shows a good agreement with the literature [40, 55]. There is a larger change in the module of the dipole moment of the A molecule 1.98 D and R

molecule 4.88 D. The AA dipole moment 3.72 D is almost twice the dipole moment of the single asphaltene molecule. The module of the dipole moment decreases with the number of aromatic cores in the aggregates except in the case of the hexamer RAAAAR. This finding is related to the number of heteroatoms in the system as they are more charged than carbon and hydrogen. Aggregates with a smaller number of heteroatoms S and/or N have the shorter dipole moment and so on (refer to Figures 4.9). However, there is a remarkable change in the module of the dipole moment of AAAAA (7.67 D) and AAAAA' (16.66 D) same for the hexamer RAAAAR (9.75 D) which has the lowest value opposite to the observation made previously. This observation may be due to the energy difference of these molecules.

The radius of Gyration describes a standard metric for the size of polymers or monomers and is shown in 4.9. The radius of gyration in the A molecule (6.41 Å) is greater than the R molecule (6.26 Å), leading to a more packed structure. The radius of Gyration has an opposite trend to the module of dipole moment for the aggregates of a polymer. The structures with the larger aromatic compound are more packed (larger radius of Gyration) and therefore have a shorter dipole moment. The radius of Gyration is ranged between $6.26 - 10.56$ Å from monomer to hexamer. These results are in agreement with the observation made in the formation energies which are related to the number of aromatic rings in the structure as well as the heteroatoms.

4.5 Kohn-Sham orbital: HOMO and LUMO

We studied the Kohn-Sham orbitals referring to the HOMO and LUMO to analyze the regions connected to the energy levels more easily accessible to molecular interactions. The HOMO and LUMO orbitals suggested the potential electron exchange regions of interaction during the aggregation process. We have analyzed the electronic properties of the isolated molecule for comparison reason with the aggregates. The frontier Kohn-Sham orbitals of A and R molecules are shown in Figure 4.10. The A molecule displays regions occupied by the orbitals from the center of the polyaromatic region, while the R molecule orbitals are spread between the small aromatic center in the nitrogen and the aliphatic group closest to the sulfur. The HOMO-LUMO energy difference of the A molecule (2.41 eV) is smaller than that of the R molecule (3.50 eV). Because of the smaller HOMO-LUMO energy difference in the asphaltene

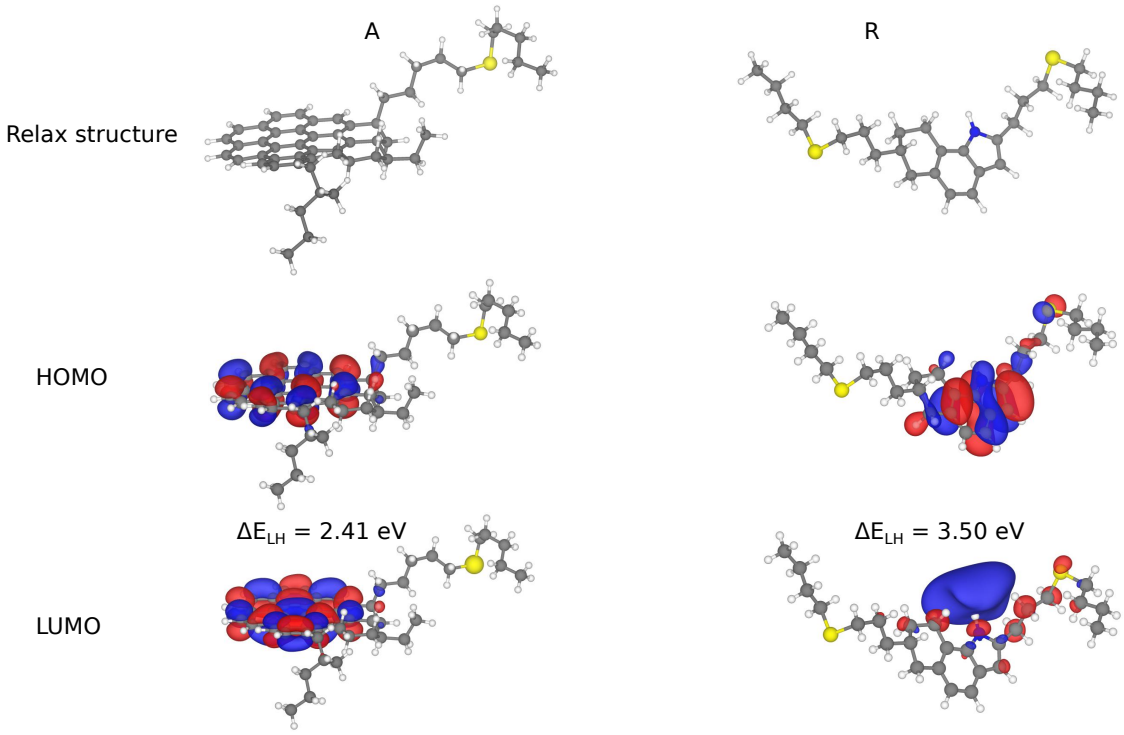

Figure 4.10: Molecular structures (top), HOMO (middle) and LUMO (down) orbitals of the A and R. The positive and negative parts of the wave functions are represented respectively by the blue and red spheroids near the atoms. Atomic colors: C (gray), N (blue), H (white), and S (yellow). Isosurface of -0.0005 *to* 0.0005 $electrons/Bohr^3$

molecule, this molecule should be more favorable to agglomerate.

As shown in Figure 4.11, the HOMOs of AA dimer are displayed around the aromatic region of both asphaltene molecules. Whereas, the LUMO is located only in one asphaltene molecule. The Kohn-Sham orbitals of AR of the valence band are located on the aromatic ring of the resin while the LUMO is located on the aromatic region of the asphaltene molecule. This result is related to the fact that the HOMO-LUMO energy difference of the AR ($2.34\ eV$) is very similar to the HOMO-LUMO energy difference of the asphaltene molecule ($2.42\ eV$). Comparing to the previous cases, the RR dimer displays a frontier orbital similar to the AA molecule (Figure 4.11). Although, the LUMO shows the positive part of the wave function concentrated in one part close to the aromatic ring, and the negative part is spread around the aromatic ring of both resin molecules.

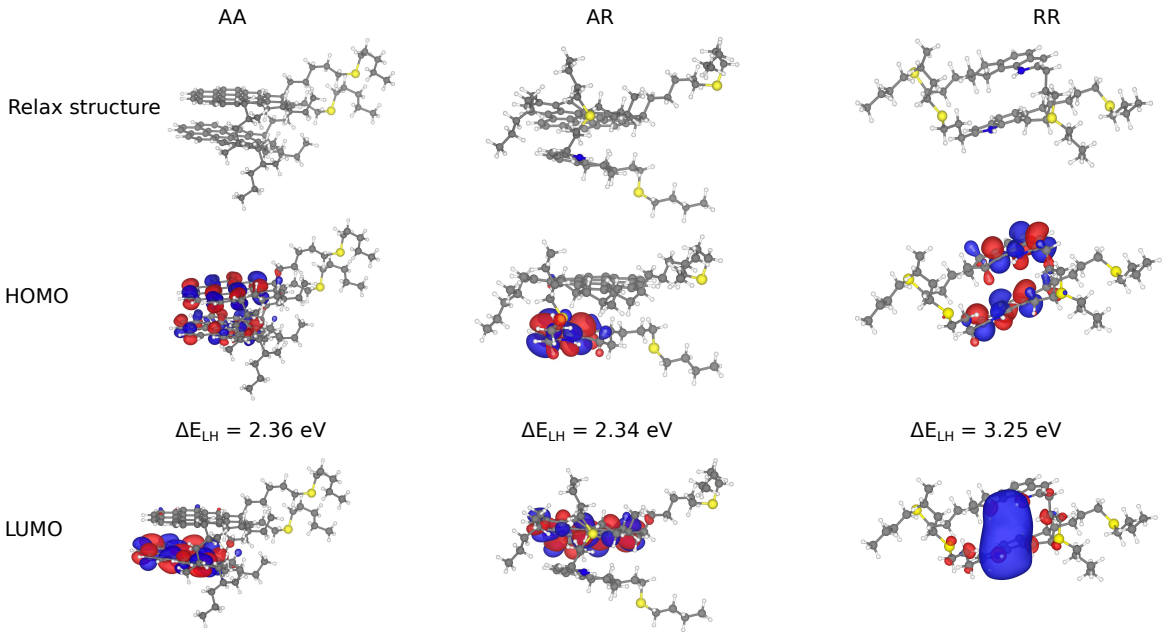

Figure 4.11: The optimized structure of the dimers AA, AR and RR (top), the Kohn-Sham orbital HOMO (middle) and LUMO (down). The positive and negative parts of the wave functions are represented by the blue and red spheroids respectively near the atoms. Atomic colors: C = gray, N = blue, H =white, and S =yellow. Isosurface of -0.0005 *to* 0.0005 $electrons/Bohr^3$

The results of the HOMO and LUMO of the trimers in Figure 4.12 ensure that the aromatic core remains favorable to the formation of the aggregates. In particular, the orbital of the conduction band (LUMO) in the AAA' is located only in one asphaltene molecule whereas the HOMO is visible in the other two A molecules. There is no difference in the HOMO-LUMO energy difference of the AAA' and RAA as it is 2.31 eV. This HOMO-LUMO energy difference is similar to that of asphaltene so that the RAA orbitals are present only in the asphaltene molecules.

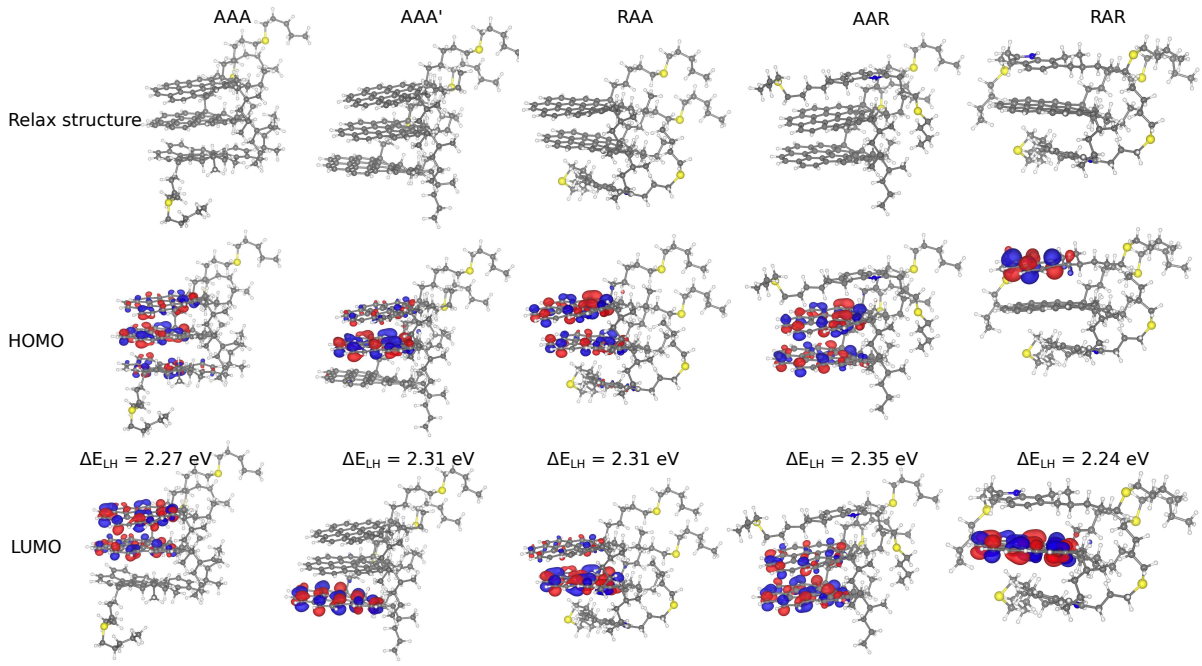

Figure 4.12: The optimized structure of the trimers AAA, AAA' RAA, AAR, and RAR (top), the Kohn-Sham orbital HOMO (middle), and LUMO (down). The positive and negative parts of the wave functions are represented by the blue and red spheroids respectively near the atoms. Atomic colors: C = gray, N = blue, H =white, and S =yellow. Isosurface of -0.0005 *to* 0.0005 $electrons/Bohr^3$

The Kohn-Sham orbitals of the tetramers represented in Figure 4.13 indeed show that the $\pi - \pi$ stacking was favored in the interaction process as it is located in the aromatic regions. The HOMO orbital is present in the two asphaltenes at the middle of the AAAA, while the LUMO is located on the last asphaltene of the end. The HOMO and LUMO of the AAAA' are well distributed in two A molecules with a few representations of the HOMO on a third molecule. The Kohn-Sham orbitals of the tetramers RAAA shown no orbital in the R molecule as the HOMO-LUMO energy difference of 2.27 eV is close to that of asphaltene.

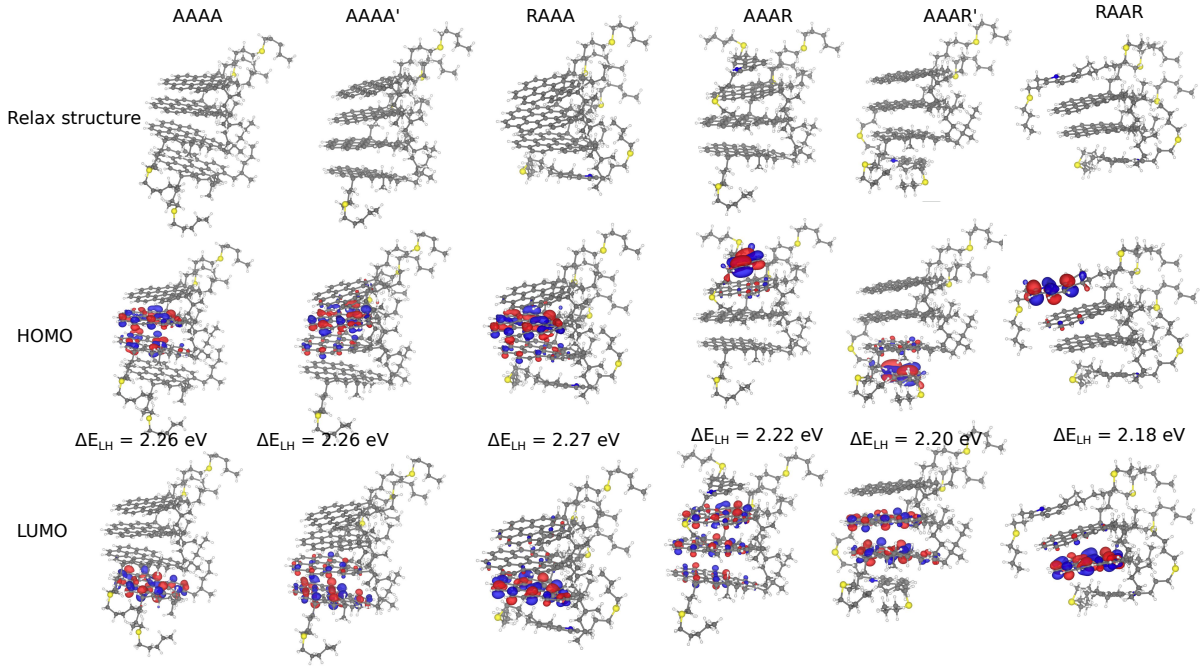

Figure 4.13: The optimized structure of the tetramers AAAA, AAAA' RAAA, AAAR, AAAR', and RAAR (top), the Kohn-Sham orbital HOMO (middle), and LUMO (down). The positive and negative parts of the wave functions are represented by the blue and red spheroids respectively near the atoms. Atomic colors: C = gray, N = blue, H =white, and S =yellow. Isosurface of -0.0005 *to* 0.0005 $electrons/Bohr^3$

As in the previous cases, the aromatic cores of the pentamers and hexamers are in the more reactive region, being indeed responsible for the formation of the aggregates (see Figures 4.14 and 4.15). In the AAAAA and AAAAA' aggregates, the HOMOs are present in two asphaltene molecules comparing to that of hexamers which can be found in three asphaltene molecules. The LUMOs of the RAAAA and RAAAAA are located only in one asphaltene molecule whereas the HOMOs are split into the A molecules in the middle of the aggregates.

The optimized structures of the aggregates with large aromatic rings are energetically more favorable due to the $\pi - \pi$ stacking in the aromatic cores as shown in the Kohn-Sham HOMO and LUMO. The HOMOs seem to move away from the resin as the number of aggregate increases, while LUMOs remain in the same position, in the asphaltene closer to the resin. The orbitals representation displays the regions of electronic states linked to molecular interaction and further formation of asphaltene nanoaggregation.

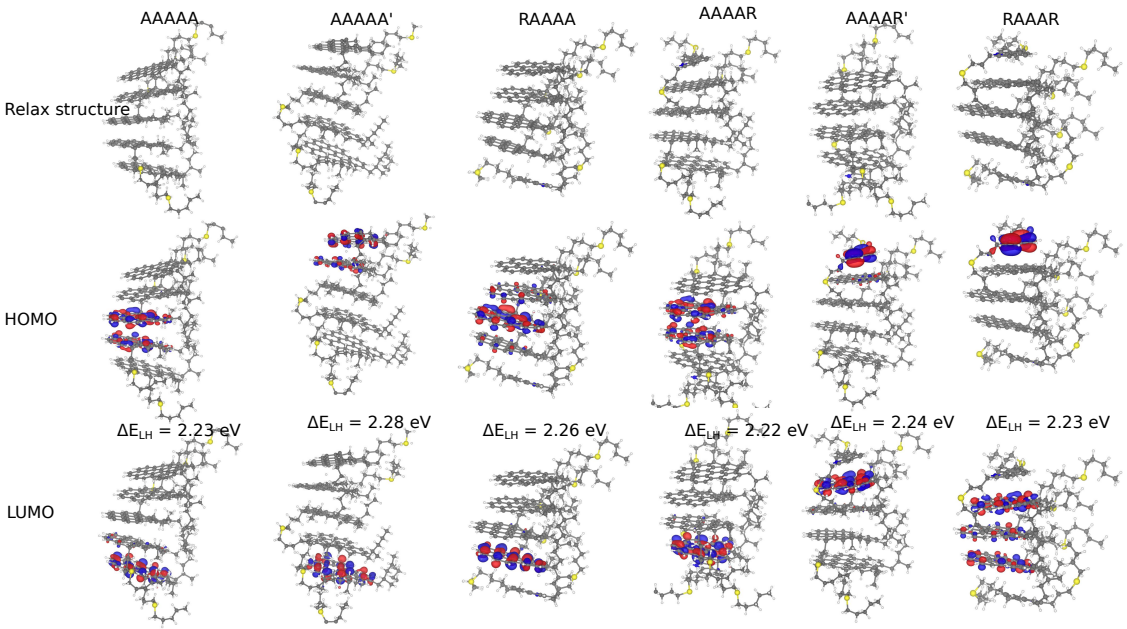

Figure 4.14: The optimized structure of the pentamers AAAAA, AAAAA' RAAAA, AAAAR, AAAAR' and RAAAR (top), the Kohn-Sham orbital HOMO (middle), and LUMO (down). The positive and negative parts of the wave functions are represented by the blue and red spheroids respectively near the atoms. Atomic colors: C = gray, N = blue, H =white, and S =yellow. Isosurface of -0.0005 *to* 0.0005 $electrons/Bohr^3$

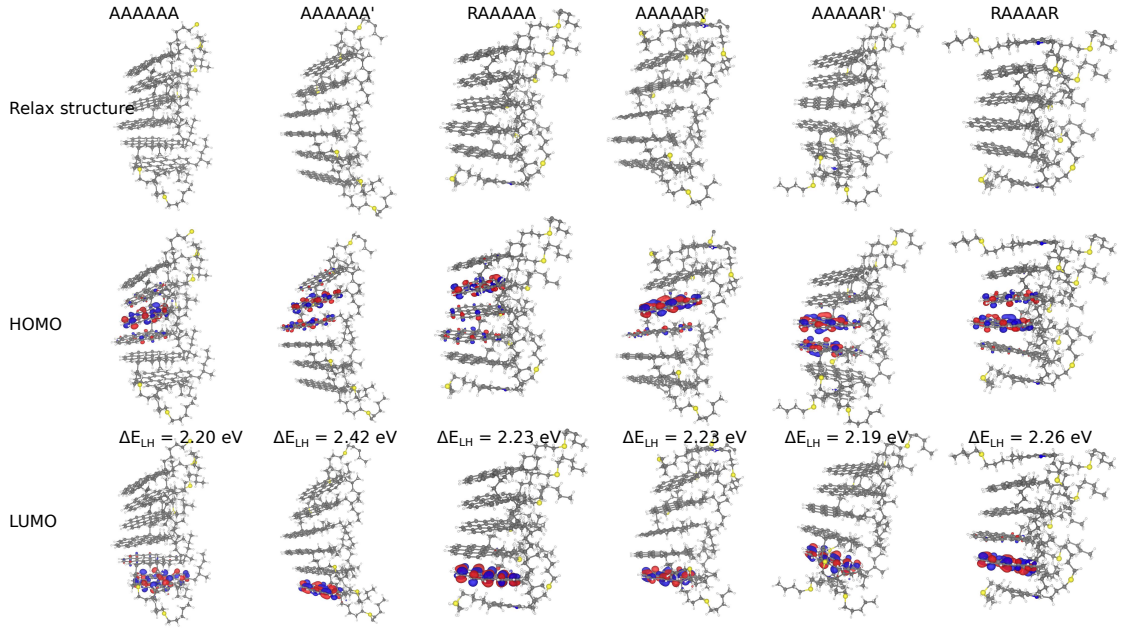

Figure 4.15: The optimized structure of the hexamers AAAAAA, AAAAAA' RAAAAA, AAAAAR, AAAAAR' and RAAAAR (top), the Kohn-Sham orbital HOMO (middle), and LUMO (down). The positive and negative parts of the wave functions are represented by the blue and red spheroids respectively near the atoms. Atomic colors: C = gray, N = blue, H =white, and S =yellow. Isosurface of -0.0005 *to* 0.0005 $electrons/Bohr^3$

4.6 Projected density of state (PDOS)

To analyze the contribution of elements involved in the interaction, the PDOS was plotted. The PDOS gives information about the different contributions of the different orbitals. It allows verify the role of each orbital on the total state of charge and we can then know which states (sp) contribute to which energy. The calculus of the PDOS was done by projecting the densities of states onto specific orbitals. From the PDOS shown in Figure 4.16, we observe that the sulfur sites display a significant contribution, which is mainly near the valence band of the A and R molecules.

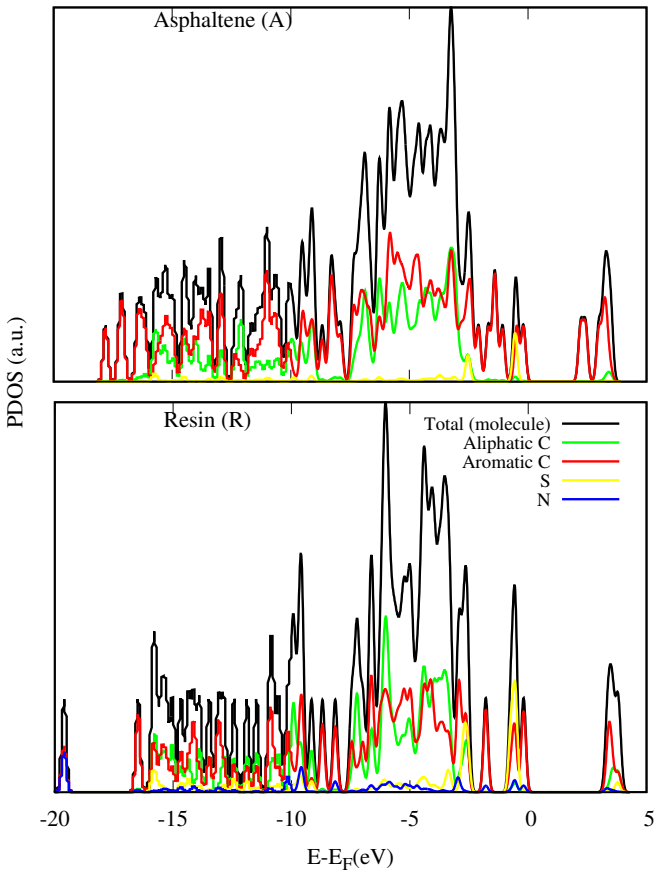

Figure 4.16: Projected density of states (PDOS) obtained for the isolated asphaltene (top) and resin (down) molecule.

The aromatic carbon sites contribute along in the valence and the unoccupied states in

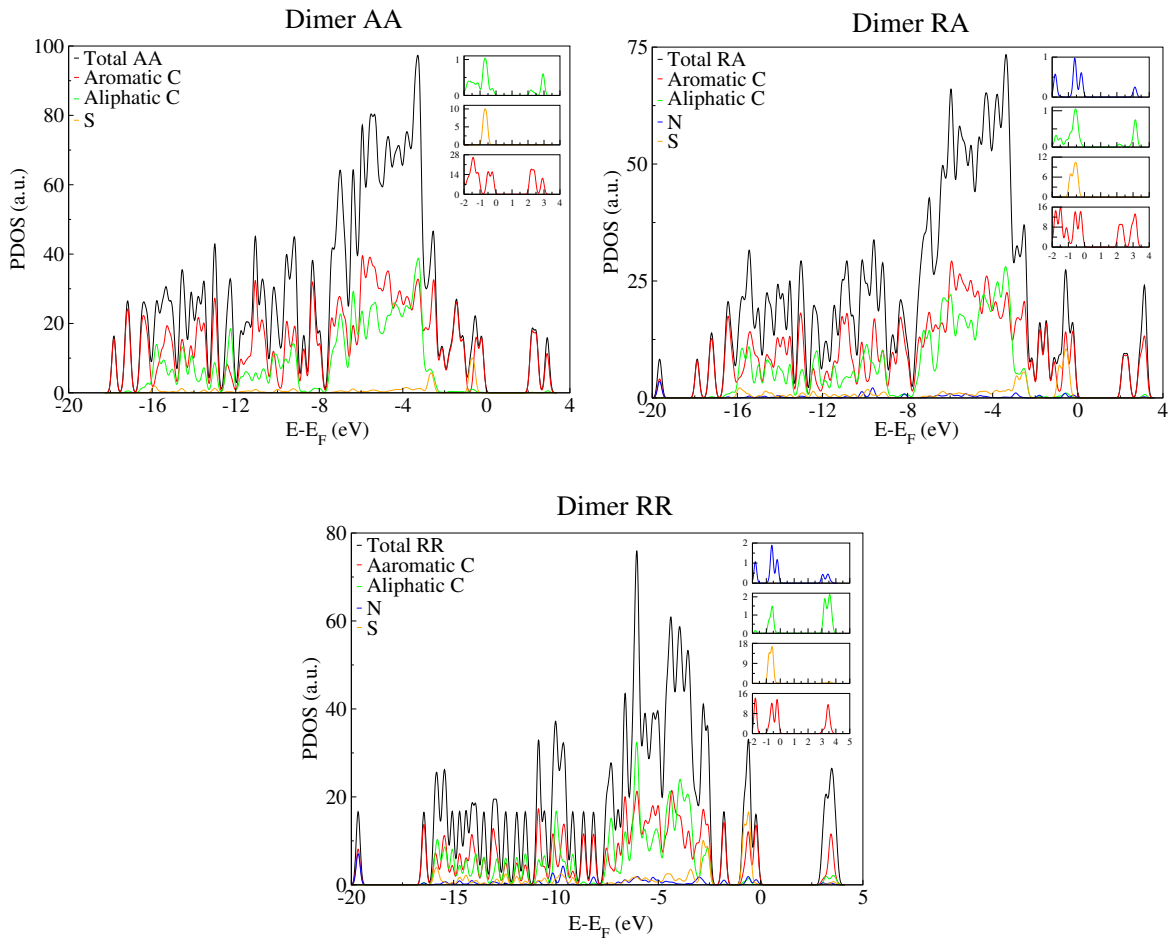

Figure 4.17: Projected density of states (PDOS) of elements in the dimers AA (top-left), AR (down-left) and RR (top-right)

the A and R molecules. As for the aliphatic carbon, their contribution is not remarkable in the occupied site of both A and R molecules. This analysis shows that sulfur and mainly aromatic carbon may be the most contributed during the interaction processes inducing A and R molecules.

Figure 4.17 shows the PDOS of the dimers AA, AR, and RR. The electronic states of the aromatic carbon are more affected in the valence and conduction band region of AA, AR, and RR dimer. There is a significant peak of the sulfur near the valence band. Indicating the contribution of this element during the aggregation process. There is a very small contribution of the N to the HOMO but not in the LUMO part except in the LUMO+2 in the dimer AR and RR.

As we move to the trimers, we observe the presence of the S peak mainly near the valence band as shown in Figure 4.18. However, we can see the reducing impact of the N in the AAR, RAA, and RAR molecule.

The PDOS of the tetramer is shown in Figure 4.19. Comparing to the previous cases, we can now observe that N does not have an impact on the aggregates' formation. However, aromatic carbon and sulfur do play a major role in the aggregation process. According to the PDOS of the pentamers shown in Figure 4.20, the electronic states are more affected in the HOMO and HOMO-1 bands.

As in the case of pentamers, the PDOS of the elements in the hexamers (see Figure 4.21) shows that N does not contribute to the formation of the aggregates. From the PDOS analysis, it is possible to confirm that aromatic carbon sites display a significant contribution as the results showed on the orbitals with the $\pi - \pi$ stacking in the aromatic cores. The heteroatom S contributes to stabilizing the aggregation.

The PDOS analysis shows a significant contribution of the aromatic carbon to the HOMO and LUMO. The S and aliphatic C do not appear to be representative in the HOMO but the HOMO-1. As we move to HOMO-1, we observe a significant representation of the S and aromatic C compared to the N and aliphatic C. As the agglomerate size increases, the aromatic and aliphatic C contribution to LUMO+1 vanishes, while the aliphatic C and S contribution goes from HOMO-1 to HOMO-2. The aromatic Carbon remains the most contributed to the HOMO and LUMO. Whereas the S and aromatic C are the most contributed to the HOMO-1. Aromatic carbon and S have the highest peak near the conduction and valence band while N and aliphatic C are less significant.

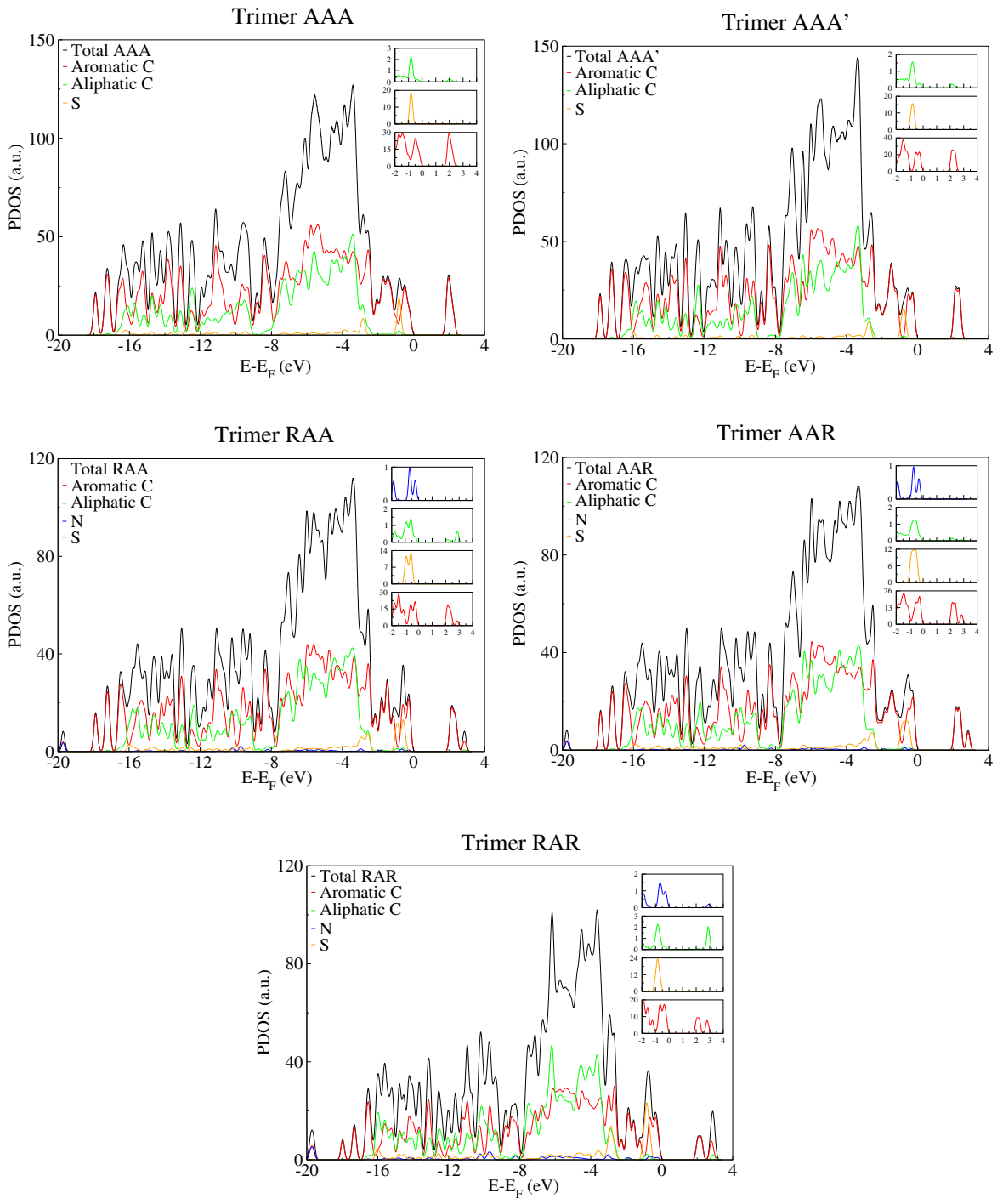

Figure 4.18: Projected density of states (PDOS) of elements in the trimers AAA (top-left), AAA' (middle-left) RAA (down-left), AAR (top-right) and RAR (middle-right)

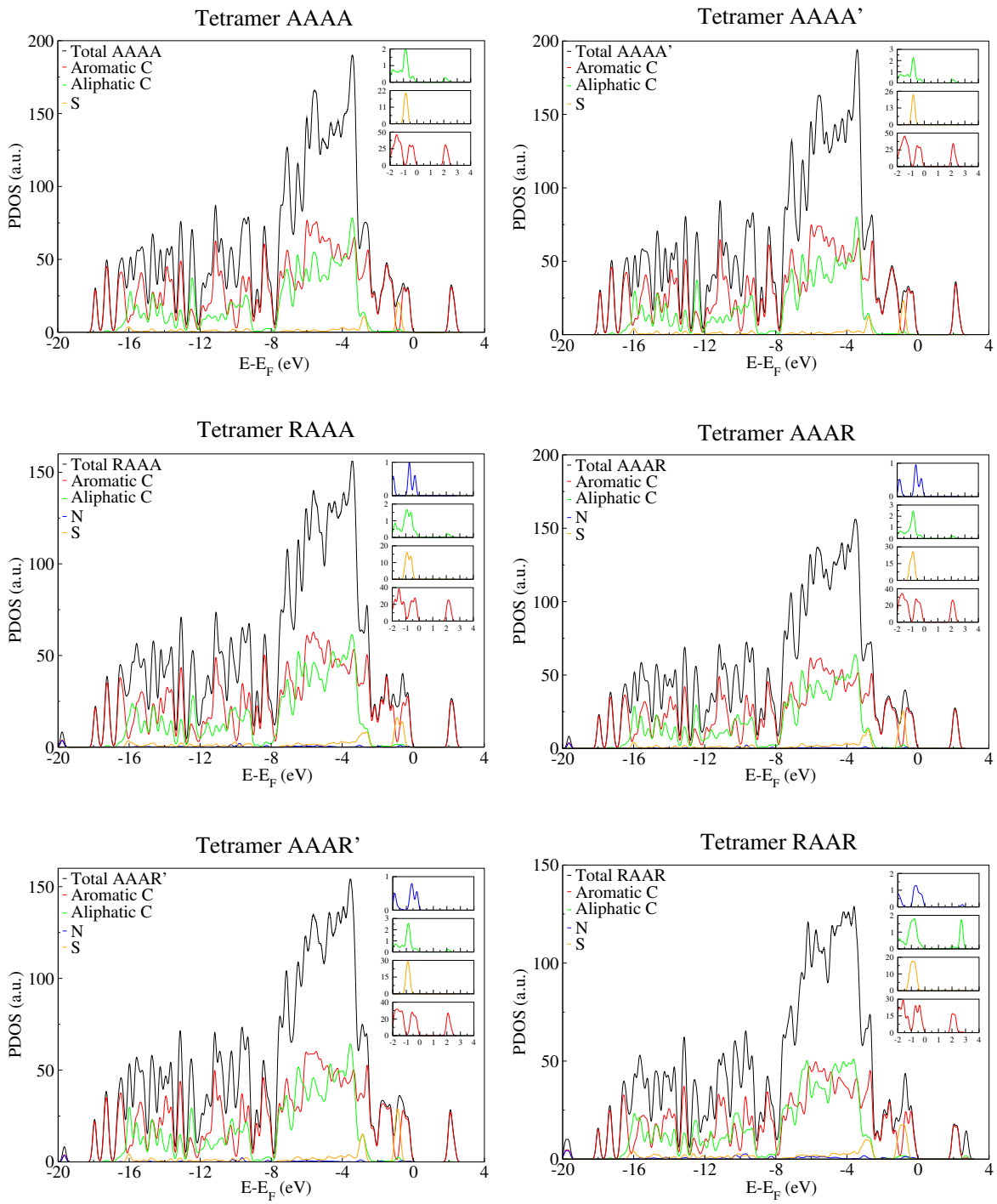

Figure 4.19: Projected density of states (PDOS) of elements in the tetramers AAAA (top-left), AAAA' (middle-left) AAAR (down-left), AAAR' (top-right), RAAA (middle-right) and RAAR (down-right)

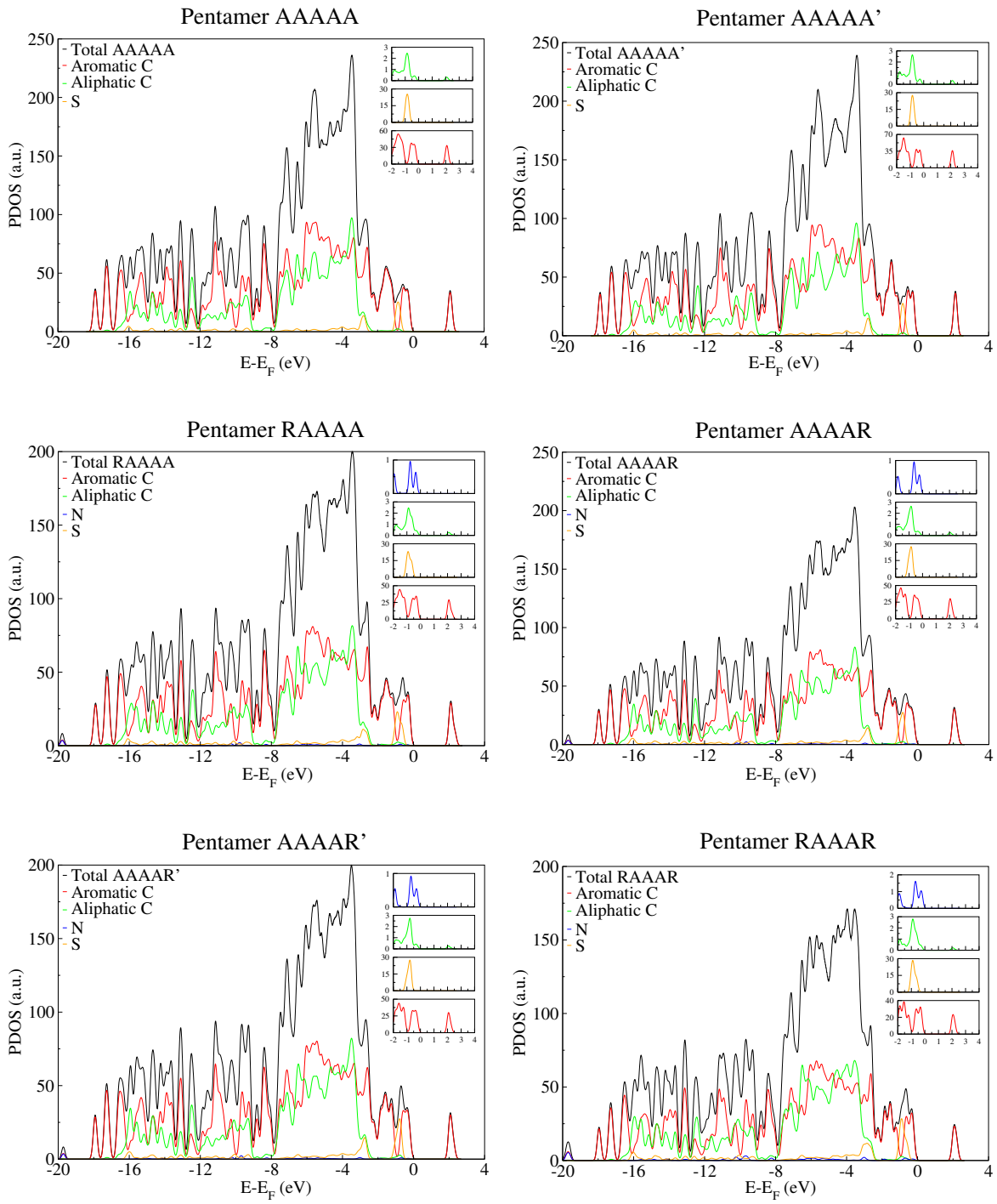

Figure 4.20: Projected density of states (PDOS) of elements in the pentamers AAAAA (top-left), AAAAA' (middle-left) AAAAR (down-left), AAAAR' (top-right), RAAAA (middle-right) and RAAAR (down-right)

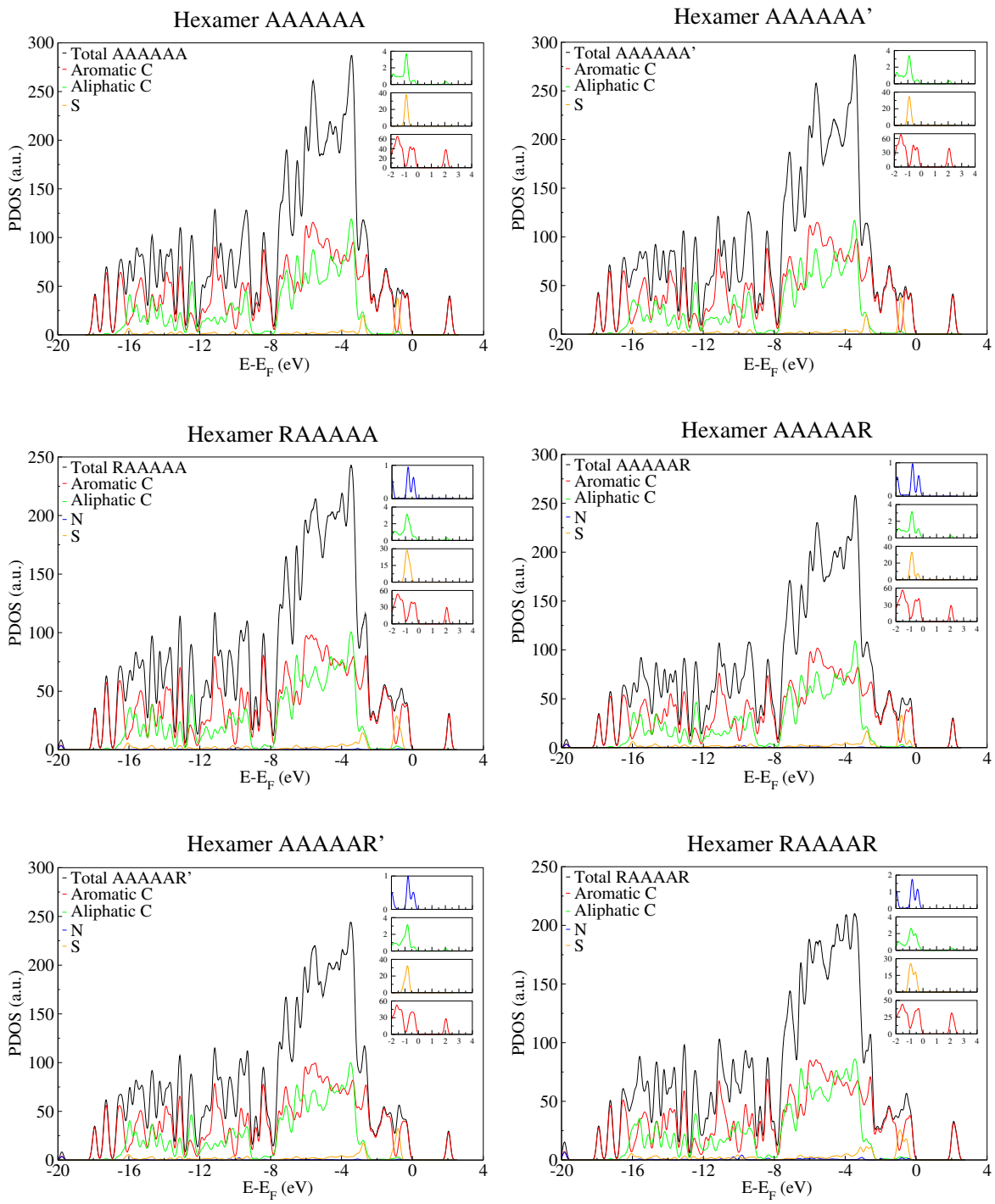

Figure 4.21: Projected density of states (PDOS) of elements in the hexamers AAAAAA (top-left), AAAAAA' (middle-left) AAAAAR (down-left), AAAAAR' (top-right), RAAAAA (middle-right) and RAAAAR (down-right)

4.7 Summary and Conclusions

The simulation of asphaltene aggregation in vacuum using a combined methodology based on molecular docking and DFT was done to obtain aggregates with up to 6 molecules. We have investigated the electronic properties and conformational structure point of view. The docking analysis was based on the structural parameters and we found that the average intermolecular distance in the aggregates was 3.5 Å, which is slightly smaller than the reference values [50, 49]. The aggregates of the dimer, trimer, tetramer, pentamer, and hexamer have shown a sandwich shape with the aromatic rings on top of each other.

From the DFT structural properties analyses, we found that the dipole moment increases with the presence of the R molecule, and the structures containing A molecule alone are more packed than the one with the R molecule as the decrease in radius of Gyration shows. Our work provided the analysis of the electronics interaction properties and the intermolecular distances from specific interaction on the formation of the dimers, trimers, tetramers, pentamers, and hexamers aggregates. After the DFT calculation, all the asphaltene aggregates obtained from the docking keep the sandwich arrangement. The intermolecular distances of the aggregates from the DFT calculation slightly increased on average 0.2 Å. The Kohn-Sham state showed a displacement of the HOMO-LUMO around the aromatic ring and the heteroatom S in the isolated R. The heteroatom S are more reactive than N in the interaction process as shown in the peak of the PDOS near the valence and conduction band.

We have shown the possibility of obtaining reduced size aggregates with a large number of molecules in the aggregates and investigate the elements involving in the asphaltene aggregation process. It was found that the aromatic carbon and sulfur do play a major role in the aggregation process while the sizes of the aggregates were smaller than the reference values with up to six (6) molecules forming the aggregates. The sulfur appears to be consistently present near the valence band with an increase in the number of aggregates. This shows that sulfur has a significant role in the formation of the asphaltene aggregates. Nitrogen and aliphatic carbon do not impact much in the aggregation process as their contribution to the PDOS near the valence and conduction bands are less significant. The main driving interaction is carried out by the aromatic carbon which induces the presence of the $\pi - \pi$ staking in the aromatic cores of the asphaltene. Asphaltene aggregates with larger aromatic cores are stable

than those with resin molecules. Asphaltene with few aromatics rings together with nitrogen is less favorable to form aggregate and may be a good candidate to destabilize the aggregation process in the crude oil. However, to improve the production of asphalt, we need to form more stable asphaltene aggregates such that we easily separate this part from the lighter part of the crude oil before the refinery process. In this case, the more stable the asphaltene aggregates, the better the separation process.

CHAPTER 5

DEVELOPING A MOLECULAR MODEL OF ASPHALT FROM A BRAZILIAN CRUDE OIL SOURCE

5.1 Introduction

To have a specific asphalt model for the Brazilian scenario, we developed a model composition to represent the Brazilian/Laguna ABG crude oil source. This model can be used to predict the rheological and mechanical properties of asphalt pavement. The properties of interest are the chemical composition of molecules in asphalt, the proportion of elements in the molecular model, and the thermodynamics and mechanical properties such as density, viscosity, bulk modulus, and isothermal compressibility.

Molecular simulations predict the macroscopic properties resulting from specified microscopic molecular interactions and structures. To do molecular simulations on a complex mixture, such as asphalt, building models' asphalt to provide input for simulation is needed. We developed a four-components asphalt with the chemical structures taking from the literature and that match elemental composition, mass fraction, molecular classes, and components

specific to the Brazilian/Laguna ABG asphalt. The chemical composition of molecules in the asphalt was grouped into four parts based on their polarity, solubility, and molecular weight: saturates, polar aromatics, naphthene aromatics, and asphaltenes.

Asphaltenes are hydrocarbons with larger aromatic rings and few side chains. They are polar molecules that are insoluble in straight-chain alkanes such as n-heptane or n-pentane and are soluble in aromatic solvents such as toluene, benzene, or pyridine. They are the heaviest component of asphalt, solid or semi-solid, black to brown hydrocarbon. The structure used to represent the asphaltene component in our model is asphaltene A ($C_{53}H_{58}S$) with a molecular weight of 726 g/mol (see Figure 5.1 a).

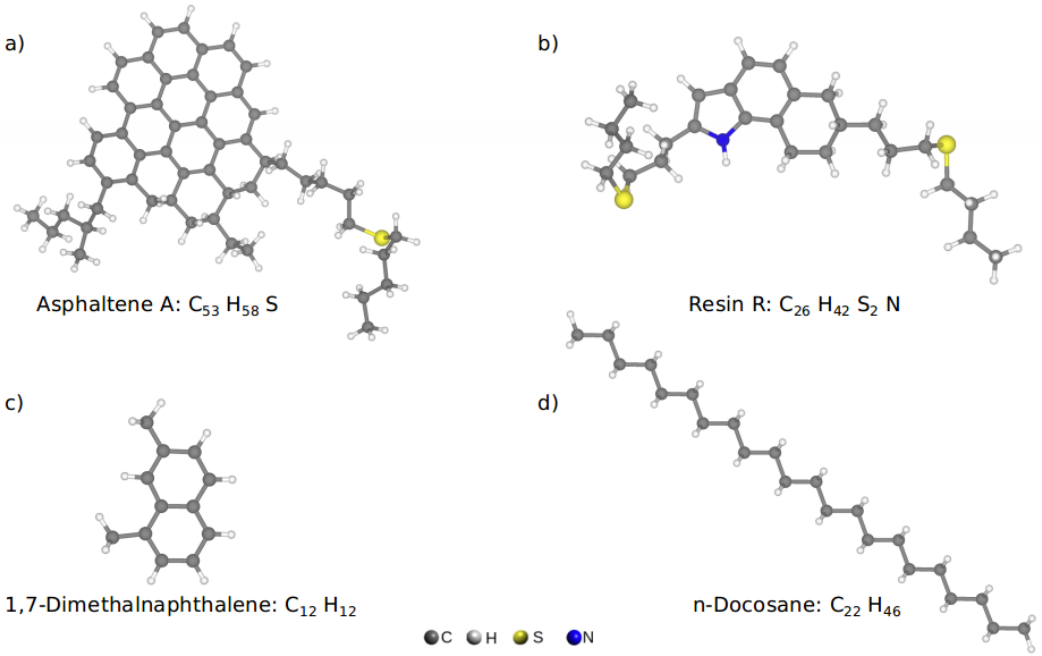

Figure 5.1: Top view representation of molecules in the asphalt model: a) Asphaltene A; b) Resin R; c) 1,7-Dimethylnaphthalene; d) Docosane

Polar aromatics are hydrocarbons derivatives of benzene that adsorb and elute when a polar solvent such as alcohol mixture is added. The resin R ($C_{26}H_{41}S_2N$) was chosen to represent the polar aromatics component, with a molecular weight of 431 g/mol (see Figure 5.1 b). Polar aromatics have a molecular weight between asphaltene and saturates. They are semi-solid or liquid hydrocarbons, less colored than asphaltene, and can contain heteroatoms such as sulfur and nitrogen. The asphaltene A and resin R molecules were previously established

by Boek and coworkers [56] using Quantitative Molecular Representation. We have chosen these molecules because it represents the structural models that show the best concordances with the experimental data from elemental analysis, nuclear magnetic resonance, and mass spectroscopy [57, 58].

Molecules that elute with an aromatic solvent such as benzene are called naphthene aromatics. We have chosen 1,7-dimethylnaphthalene ($C_{12}H_{12}$) to represent the naphthene aromatics (see Figure 5.1 c). Its size is relatively small with a molecular weight of 156.22 g/mol. The number of aromatic rings and aliphatic chains of 1,7-dimethylnaphthalene makes it intermediate between saturated and asphaltenes. However, its alkane:aromatic ratio of 16.7:83.3 is different from the overall resin balance reported by Storm David A. *et al.* [59, 60]. The two sets of aromatics (polar aromatics and naphthene aromatics) are soluble in n-heptane but insoluble in n-pentane.

Saturates are nonpolar straight chains hydrocarbon or cyclic hydrocarbon joined by a single bond. They are the lighter part of asphalt, soluble in alkanes, and are colorless fluids. The molecule used in our model to represent saturates is the docosane ($C_{22}H_{46}$) with a molecular weight of 310.6 g/mol. Docosane was chosen because it represents the normal alkane with the highest concentration in the asphalt model considered by Kowalewski *et al.* [117]. The molecular structure of $C_{22}H_{46}$ is shown in Figure 5.1 d).

5.2 Molecular model of asphalt by chemical composition

The pavement performance is governed in part by the chemical composition of asphalt although it depends on both asphalt and aggregate. Asphalts that differ in chemistry lead to a different performance in road pavement. Good molecular structure representation could be useful in correlating the physical properties to the engineering ones. The number of each type of molecule used in our asphalt model was adjusted manually to match experimental data of the ABG from the SHRP Asphalt Research Program [14]. Table 5.1 shows the chemical composition of elements in the docosane, 1,7-dimethylnaphthalene, resin R, and asphaltene A molecules. The percentage of the mass fraction of the sulfur (4.4) in the asphaltene A and the

nitrogen (3.2) in resin R molecules are in the range of the experimental [14].

Table 5.1: Chemical Composition of elements in the molecular classes of our ABG asphalt model.

molecules	formula	MW (g/mol)	$\%C$ (by mass)	$\%H$	$\%S$	$\%N$	$\%C$ aromatic (vs total C)	$\%C$ aliphatic
Asphaltene A	$C_{53}H_{58}S$	726	87.6	8.0	4.4	—	66.0	34.0
Resin R	$C_{26}H_{41}S_2N$	431	72.4	9.5	14.9	3.2	46.2	53.8
1,7-DMN	$C_{12}H_{12}$	156.22	92.2	7.7	—	—	83.3	16.7
Docosane	$C_{22}H_{46}$	310.6	85.0	14.8	—	—	—	100

The composition of the ABG from the Laguna crude oil source and our model is shown in Table 5.2. The overall mixture concentration of each component of our model was chosen to fit the experimental data [14]. Since molecular simulations require a precise number of molecules rather than the mass fraction, we have chosen the total number of atoms in the ABG basing on the computational resources. The ABG model is then composed of 51 molecules of docosane, 247 molecules of 1,7-dimethylnaphthalene, 36 molecules of resin-R, and 18 molecules of asphaltene-A.

Table 5.2: Overall composition of asphalt from Laguna crude oil and our asphalt model.

Asphalt		ABG (model)	ABG (SHRP[14])
Chemical component Analysis %	Saturates	19.1	19.1
	Naphtene aromatics	46.5	46.6
	Polar aromatics	18.7	18.7
	Asphaltenes	15.8	15.7
Elemental Analysis	C %	86.4	83.7
	H %	9.4	11.2
	N %	0.6	0.38
	S %	3.5	4.05

5.3 Computational Details

5.3.1 Construction of the bulk asphalt models

Packmol [118] was used to construct a 3D bulk model of the ABG asphalt with a cubic cell of $70 \times 70 \times 70$ (Å). The box size was chosen based on the 0.8 g/cm^3 bulk density such that it prevents the molecule chains from twisted with each other. During the process of the bulk model, the four types of molecules are randomly distributed in the cubic cell. The bulk model of the ABG asphalt is shown in Figure 5.2.

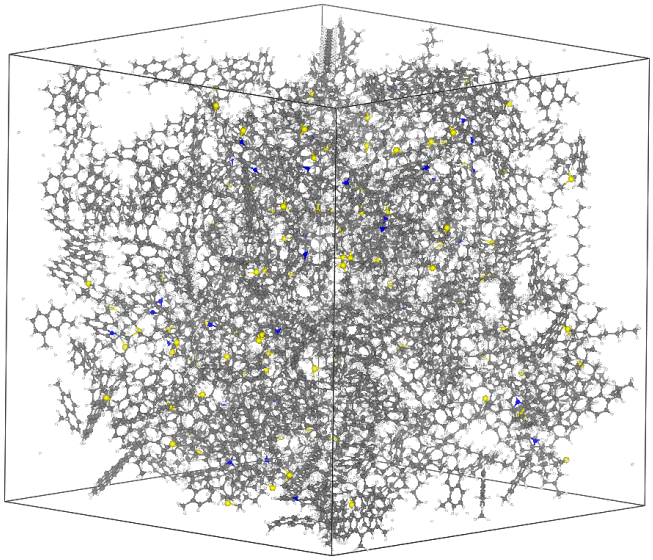

Figure 5.2: Bulk representation of the molecular structure of the ABG asphalt

5.3.2 Molecular dynamics simulation

To predict the macroscopic properties of ABG asphalt that result from microscopic molecular interactions and structures, we used MD simulation to investigate thermodynamics and mechanical properties. The LAMMPS [65] package was employed to conduct MD simulations and calculate the thermodynamics and mechanical properties referring to the density, viscosity, bulk modulus, and isothermal compressibility of the ABG asphalt. The CHARMM-based interatomic potential was used as described in section 3.2.1. The Force Field parameters are given in Appendix A. A time step of 0.5 fs was used for all simulations with

the long-range electrostatics based on the PPPM [93, 119].

Initially, the system was optimized and pre-equilibrated in the NVT ensemble for 200 ps simulation time. A periodic boundary condition with a cubic cell of $70 \times 70 \times 70$ Å was considered. To equilibrate the system, MD simulations were performed in the NPT ensemble at 1 atm pressure and a simulation time of up to 6 ns. To analyze how the properties of the ABG change with temperature, the system was simulated at six different temperatures which are 240, 270, 300, 330, 360, and 445 K (-35, -5, 25, 55, 85, and 170 ^oC respectively). This spans a range from the cold winter season to exceeding the hot-mix temperatures reached during paving operations.

5.4 Simulation results

5.4.1 Density

Density is a basic thermodynamic property and it is a direct indicator to see whether the model size and force field could yield reasonable and accurate simulation results. It is defined as the ratio of the mass over the volume. To ensure the accuracy of the simulation, we have chosen a random sample of ten (10) different initial configurations for the ABG asphalt model. The system was equilibrated up to 4 ns and then 2 ns for each configuration. Here we have presented the density dependence simulation time step of two configurations in Figure 5.3. The remaining configuration results can be found in Appendix B.

For the overall configurations, the convergence is reached at 3 ns simulation time step. The density converges faster when temperature increase and decreases monotonically with respect to temperature. The density converges slowly at low temperature although, for some configurations, this effect is more backward.

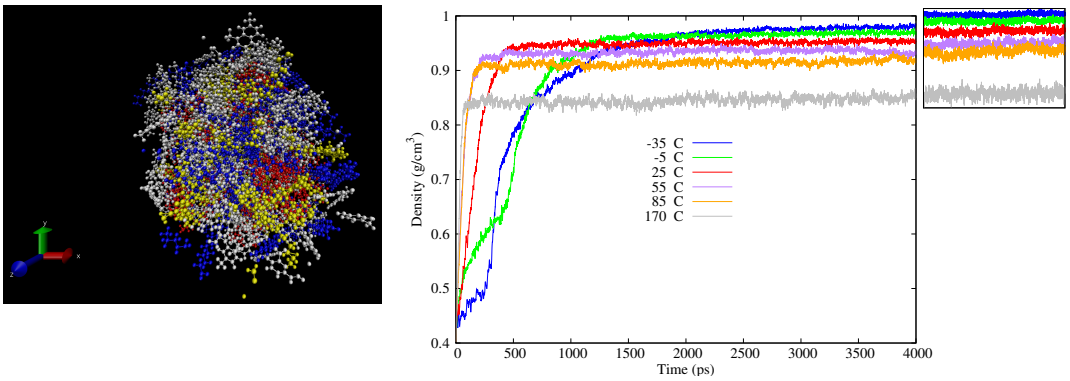

a) Configuration 1

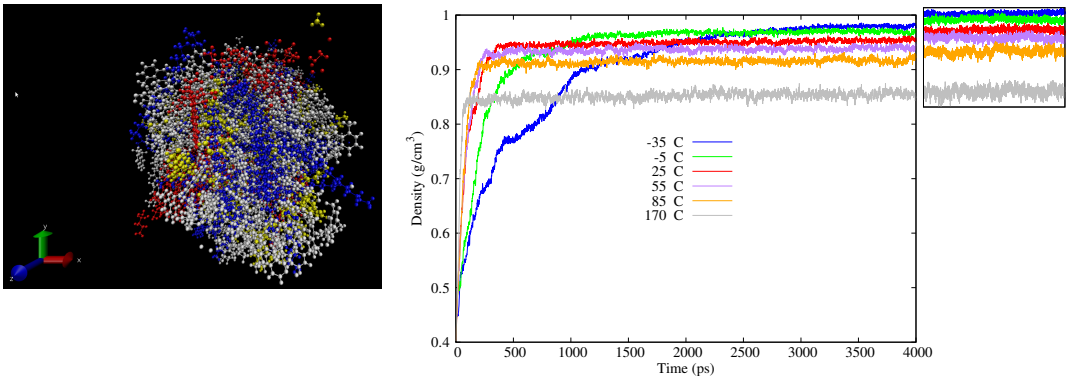

b) Configuration 2

Figure 5.3: Evolution of the density as function of the simulation time in the MD simulation for 10 initial different configurations: blue = docosane; white = 1,7-dimethylnaphthalene; yellow = resin; red = asphaltene

Figure 5.4 a) shows the results of the average density change with temperature for all the 10 initial configurations of the ABG asphalt model. The densities from the different initial configurations are compatible and the standard error of the average density is small ($\simeq 0.0006$) as shown in Figure 5.4 b). The density of the ABG asphalt decreases with the temperature and the highest predicted densities are at $-35\ ^oC$ with an average value of 0.98 g/cm^3 whereas the lowest densities are at 170 ^oC with an average value of 0.85 g/cm^3.

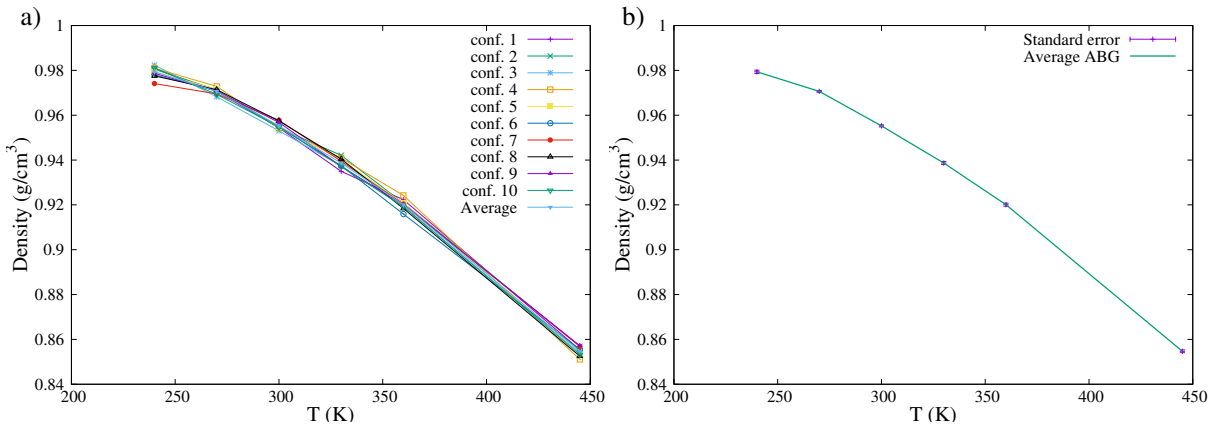

Figure 5.4: Density of the AGB model under different temperatures: a) density of the 10 different initial configurations; b) average density

Robertson *et al.* [63] have reported densities of several asphalt from the SHRP at 60 ^oC which was in a range of 0.99 $-$ 1.03 g/cm^3. Unfortunately, the densities of the ABG model were not reported. The mean value of the density of the ABG model is 0.94 g/cm^3 at 60 ^oC. The densities results of our ABG model are likely close to the real asphalt model compared with the densities from the molecular dynamics simulation of the models' asphalt reported in the literature [12, 10, 62, 64, 16, 18]. There is consistency in the trend of the density as it decreases when the temperature increase.

5.4.2 Viscosity

The viscosity of a fluid is its resistance to gradual deformations caused by shear or tensile stress. It can be understood as a measure of the susceptibility of a fluid to transmit momentum in a direction perpendicular to the velocity or momentum flow. There are at least four methods to determine the shear viscosity using various options in LAMMPS: The first method is based on non-equilibrium MD (NEMD) simulation in which the unit box is sheared in the simulation and the fluid thermostat is set via the SLLOD equations [120]. In parallel, there is a second method that uses moving walls to shear the fluid in between them and thermostat the non-shearing components of velocity to prevent heating. The third method, the Müller-Plathe, is a reverse non-equilibrium MD (rNEMD) simulation. The fourth methods are the Green and Kubo in which the shear viscosity is related to the correlation functions of tensor in thermal

equilibrium MD [121].

In this thesis, the viscosity was calculated using the Müller-Plathe method [68]. The advantage of this method compared to the others is linked to the fact that for a large system as asphalt, flux is hard to define and converge slowly microscopically. Also, the Müller-Plathe method can be used in the microcanonical ensemble in MD simulation without a thermostat, keeping the total energy and linear momentum conserved. As a rNEMD simulation method, the cause and effect in the Müller-Plathe method are reversed compared with the usual NEMD simulation. This implies imposing the momentum flux on the system and then the response is the shear velocity.

The shear viscosity giving in Equation 5.1 can be defined as the proportionality coefficient of the shear field (gradient of the x component of the fluid velocity with respect to the z-direction) with a flux of transverse linear momentum.

$$\begin{aligned} J_z(p_x) &= -\eta \frac{\partial v_x}{\partial z} \\ J(p_x) &= \frac{p_x}{2tA} \end{aligned} \tag{5.1}$$

where $J_z(p_x)$ is the momentum flux which is also the x component of the momentum flowing in the z-direction per given time t and per unit area A. The momentum flux is in units of momentum/area/time; $\frac{\partial v_x}{\partial z}$ is the velocity gradient of the fluid moving in the x-direction normal to the momentum flux, η is the shear viscosity of the fluid which thus has units of pressure-time ($kg.m^{-1}.s^{-1} = 1P$), p_x is the momentum, A is the area which is equal to the box length $Lx \times Ly$ and t is the simulation length. Factor 2 came from the periodicity of the system.

Among the 10 configurations, we have chosen six of them that converge more rapidly to evaluate the viscosity of the ABG. The simulation was performed up to at least 5 ns and the response of the shear velocity was recorded every 10000 steps. In LAMMPS, the unit for the viscosity is $gram/mol/angstrom/femtosecond$, while the rotational viscosity unit is $kilogram/meter/s = 1P$. The unit was then converted from $gram/mol/angstrom/femtosecond$ to cP.

Figure 5.5 a) shows the momentum transfer within the simulation of the third configuration at 445 K. During the momentum transfer simulation, the temperature range was kept around

20 K. The linear trend of the momentum transfer of a small amount of molecules in the MD simulation can be observed in Figure 5.5 b).

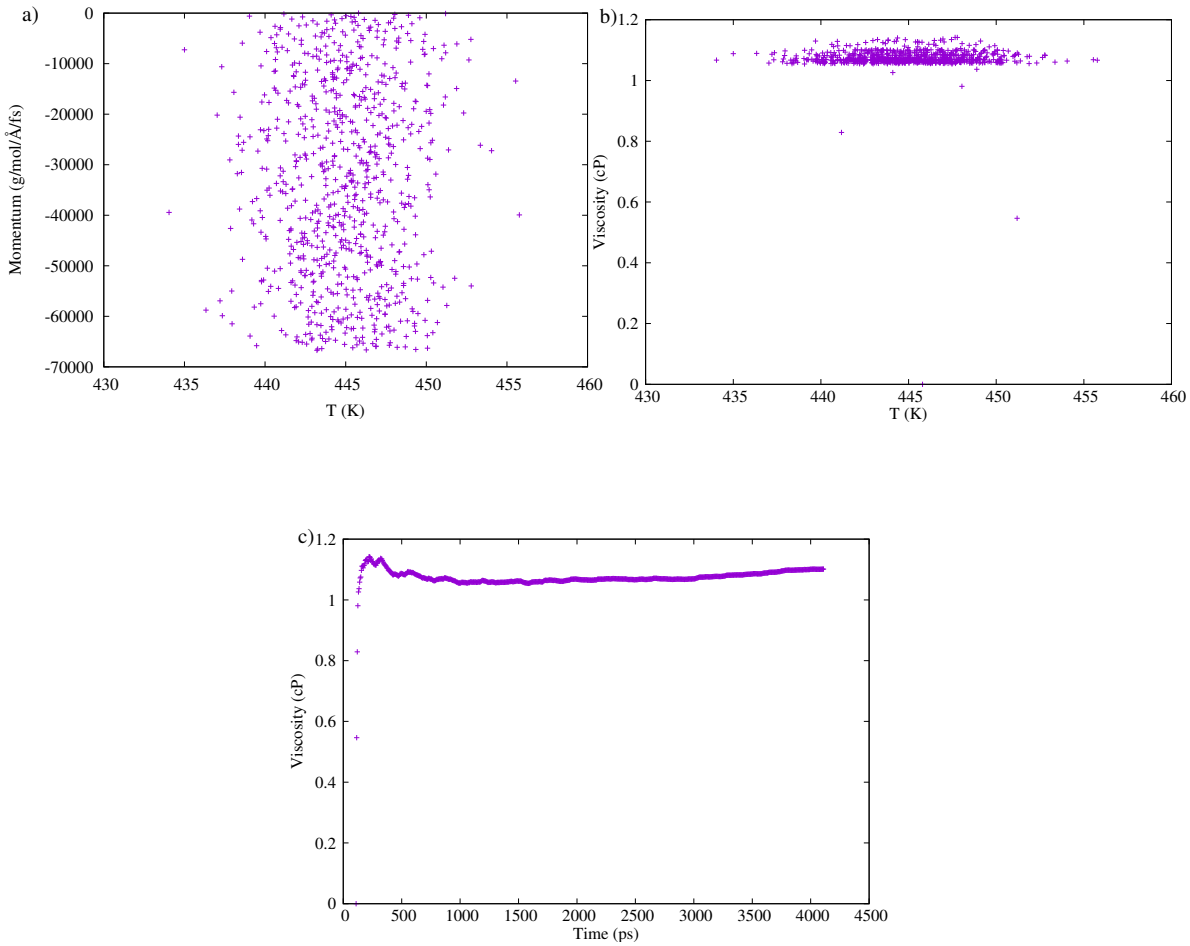

Figure 5.5: a) Momentum transferred in the ABG model at 445 K; b) Viscosity of ABG model at the temperature at 445 K; and c) Viscosity results as a function the simulation time at 445 K

As shown in Figure 5.5 c), the viscosity with respect to the simulation time reached the plateau after a sufficiently long time. In this work, we have shown only the change in the viscosity for the simulation time at 445 K. However, for the low temperature, we observed that there is an increasing noise in the plateau of the viscosity. The viscosity remains consistent with a certain magnitude. Yet, the fluctuation observed here is common due to the limited number of molecules used in the MD simulations compared to the macroscopic scale.

The viscosities at a given temperature were averaged to obtain the relationship between the temperatures and viscosity. Due to the limitation of MD simulation to compute viscosity at a low temperature, we have considered four temperatures which are 300, 330, 360, and 445 K. Six different initial configurations were chosen to verify the accuracy of the simulation results. The viscosities change with the temperature of the 6 initial configurations are shown in Figure 5.6 a).

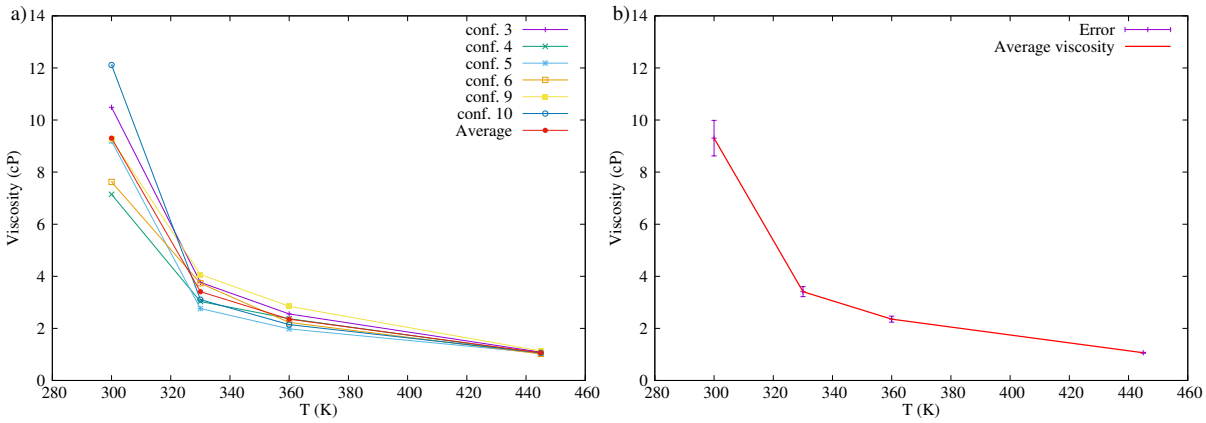

Figure 5.6: Viscosity of the ABG model under different temperatures: a) Viscosity of 6 different configurations; b) Average Viscosity.

The viscosity of the model ABG decreases as temperature increases and it has a similar trend with the other asphalt model in the literature [10, 18, 71]. For a complex system like asphalt, the viscosity at low temperature is hard to obtain numerically as it requires a very long relaxation time which usually exceeds the available simulation time. This is why the error viscosity in Figure 5.6 b) is higher when the temperature decreases.

5.4.3 Bulk Modulus and Isothermal Compressibility

One of the factors responsible for the failure of asphalt is the cohesion loss within the asphalt. It is related to the stress-strain change and is strongly linked to the chemical properties of asphalt. The bulk modulus is the basic property of materials to measure their resistance under compression or expansion. It refers to the compressibility of the material under uniform stress. The isothermal compressibility (β_T) is the inverse of the bulk modulus (K) and it is

calculated from the fluctuations in volume (V) within the simulation at a constant temperature (T) as shown in Equation 5.2.

$$\beta_T = \frac{1}{K} = -\frac{1}{V}\left(\frac{\partial V}{\partial P}\right)_T. \tag{5.2}$$

Where $\left(\frac{\partial V}{\partial P}\right)_T$ is the fluctuation in the volume to the stress P at a constant temperature T. The NVT simulation was performed using the Nose/Hoover thermostat [122, 123] with the SLLOD equations of motion [120, 124, 125] to update positions and velocities of the atoms at each simulation time step. The simulations were performed up to 4 ns.

During the MD simulation, an infinitesimal deformation of $\pm 1.25 \times 10^{-8}$ was applied to the ABG model boundaries at every simulation time step. The positive and negative strains ϵ in the three directions and the overall volumetric strain Δ was calculated as shown in Equation 5.3.

$$\begin{aligned} \epsilon_{xx} = \epsilon_{yy} = \epsilon_{zz} &= \pm\frac{L - L_0}{L_0} \\ \Delta &= \epsilon_{xx} + \epsilon_{yy} + \epsilon_{zz}, \end{aligned} \tag{5.3}$$

where L is the box length and L_0 the original box length. The stresses in the three directions σ_{xx}, σ_{yy} and σ_{zz} were computed and recorded during the stress-strain response cycle. The compressive and expansive volumetric stress was calculated using Equation 5.4

$$\sigma = \frac{\sigma_{xx} + \sigma_{yy} + \sigma_{zz}}{3} \tag{5.4}$$

The stress result in three coordinate directions was performed. To present this feature, we have chosen one result of the third configuration. However, the results of other configurations at a given temperature are similar. The stress change in the three directions and the overall strain-stress volumetric change under negative strain at the temperature of 300 K of the ABG model are shown in Figures 5.7 a) and b) respectively.

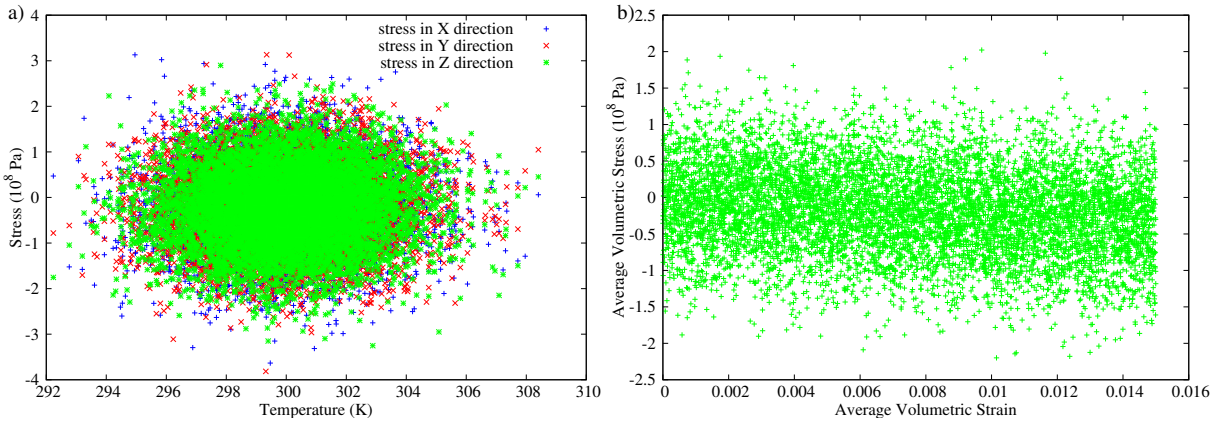

Figure 5.7: a) Stress change in the three direction and b) Relationship between the average volumetric stress-strain under the negative strain in the ABG model at the temperature of 300 K.

The average bulk modulus of the ABG model was computed by averaging the stress/strain ratio as shown in Equation 5.5

$$K = \frac{\sigma}{\Delta} \tag{5.5}$$

To obtain the relationship between the bulk modulus and the corresponding isothermal compressibility with the temperature of the ABG asphalt, MD simulations were performed for six different initial configurations that showed a rapid convergence among the ten configurations listed above. The results are shown in Figures 5.8 a), b) and 5.9 a), b) respectively.

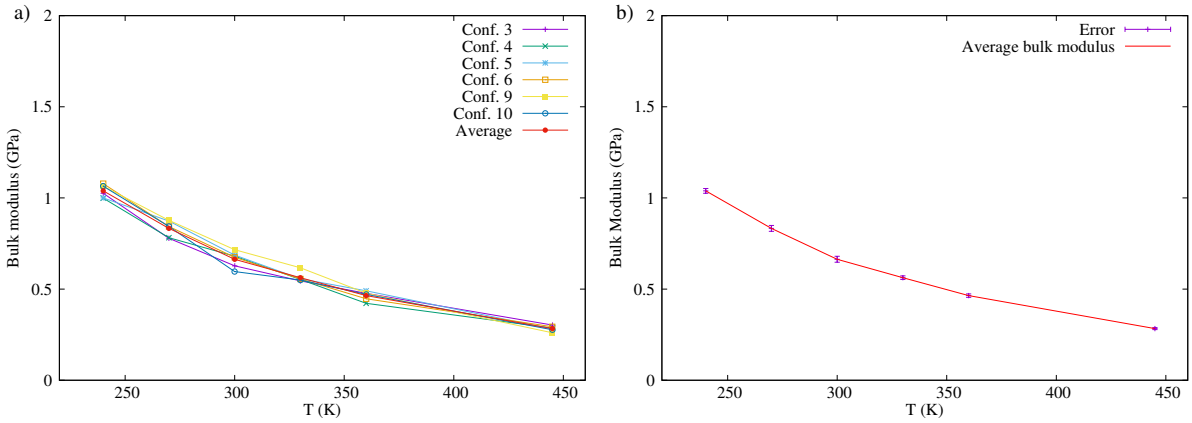

Figure 5.8: Bulk modulus of the ABG asphalt model under different temperatures: a) Bulk modulus of the six different initial configurations; b) Average bulk modulus

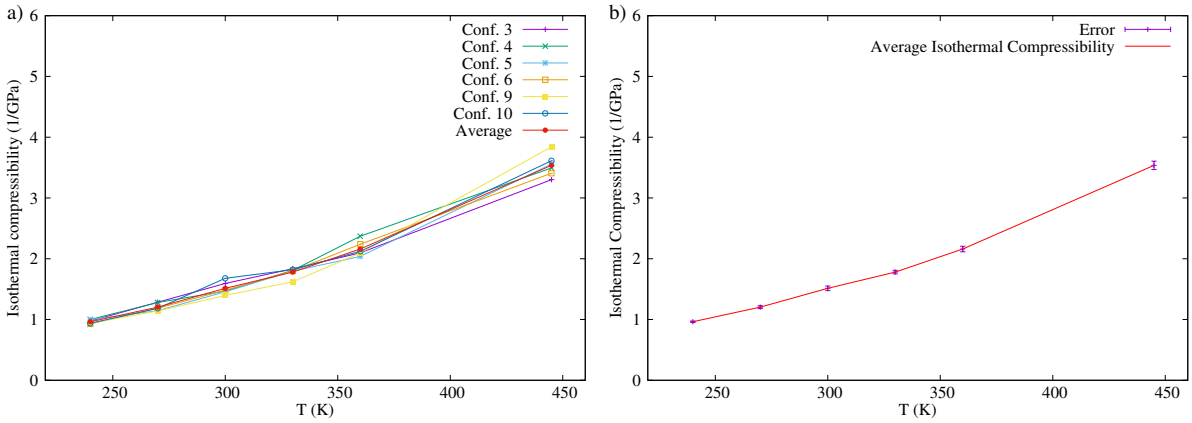

Figure 5.9: Isothermal compressibility of the ABG asphalt model under different temperatures: a) Isothermal compressibility of the six different initial configurations; b) Average isothermal compressibility

The trend of the bulk modulus and isothermal compressibility is compatible with the real asphalt model. The bulk modulus of the ABG decreases as temperature increases while the isothermal compressibility has a reverse effect. At high temperatures, asphalt is more easily compressed, and therefore, the resistance to uniform compression is low. Whereas at lower temperatures, asphalts are rigid and not easily compressed hence, the isothermal compressibility of the asphalt under uniform stress is low. Then, the isothermal compressibility tends to increase with the temperature.

5.5 Conclusion

We have developed a molecular model of asphalt for molecular simulation with chemical composition chosen to be reflective of compounds found in the Brazilian/Laguna ABG from SHRP Cores Asphalts. Molecular dynamic simulations were used to investigate the thermodynamics and mechanical properties of the model asphalt including density, bulk modulus, isothermal compressibility, and viscosity. The chemical composition of the model asphalt is subdivided into four groups: asphaltenes, naphthene aromatics, polar aromatics, and saturates. Four components were used to represent each group in the ABG asphalt model namely docosane $C_{22}H_{46}$, 1,7-dimethylnaphthalene $C_{12}H_{12}$, resin-R $C_{26}H_{41}S_2N$, and asphaltene-A $C_{53}H_{58}S$ in the proportions of [19.1:46.5:18.7:15.8] respectively.

The ABG asphalt model displayed properties in simulations that were qualitatively similar to those of real asphalt. The densities of the ABG model decrease with an increase in temperature. The density from the molecular dynamics simulation of the ABG model system is closer to that of some real asphalt compared to the models in the literature. The ABG model showed a decrease in viscosity as the temperature increase. The simulation results indicate that the temperature-modulus trends of the ABG models were compatible with that of real asphalt as it decreases with an increase in temperature. The isothermal compressibility of the ABG asphalt showed that the resistance to uniform compression is higher when the temperature decrease.

CHAPTER 6

MODIFIED ASPHALT MODELS WITH SILICA NANOSTRUCTURES

Silica is one of the most common chemical compounds found in aggregates used for asphalt pavement. It is common in sand and granite with a high percentage. SiO_2 nanoparticles are related significantly to the resistance of the asphalt to fracture, failure behavior, and durability [21, 22]. In this chapter, we shall use silica nanoparticles to represent the ideal aggregate of asphalt in molecular dynamics simulation and study their effects modification on the physical properties of the ABG asphalt model. Molecular Dynamics simulation provides insight to relate the chemical characterization of the asphalt at the nanoscale with its macroscopical properties.

6.1 Molecular models and MD simulation

6.1.1 Creation of silica nanoparticles and the modified asphalt models

A Monte Carlo scheme to generate realistic hydroxylated SiO_2-NPs atomistic models was previously developed [26, 29]. This algorithm can provide at the nanoparticle surface any percentage of silanol $Si(OH)$, and geminal $Si(OH)_2$. We generated three nanoparticle models with different hydroxylated terminal group distribution on the NP surface for this study. Following the previous work terminology[27, 29], the NP A rich in silanol, D rich in geminal, and the last model E has a balance in silanol and geminal group. The models are nearly spherical with an average diameter of 1.5 nm containing, respectively 183, 240, and 198 atoms. The overall compositions are shown in Table 6.1 and the molecular structures of the three generated SiO_2-NPs are shown in Figures 6.1 a), b), and c).

Table 6.1: Relative mass percentage composition of the hydroxylated group on the surface of the amorphous SiO_2-NPs.

NP model	$wt.\ \%\ Si(OH)$	$wt.\ \%\ Si(OH)_2$
A	83	17
D	17	83
E	50	50

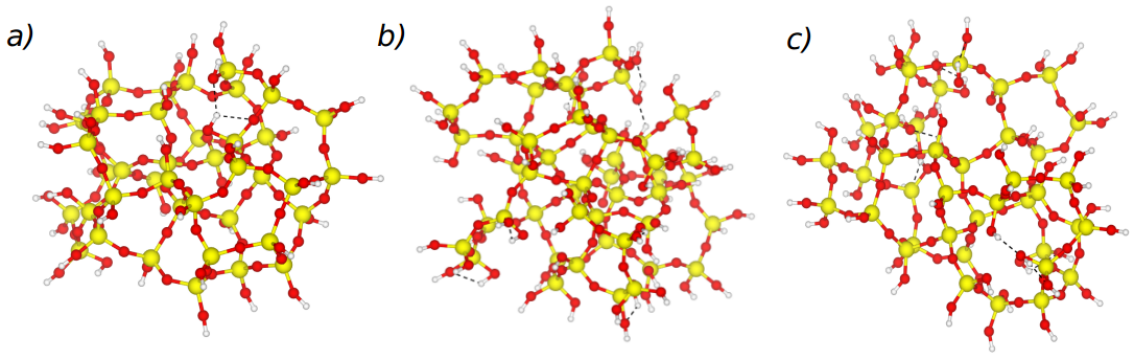

Figure 6.1: a) SiO_2-nanoparticles A: 83% silanol and 17% geminal group; b) SiO_2-nanoparticles D: 17% silanol and 83% geminal group; and c) SiO_2-nanoparticles E: 50% silanol and 50% geminal group: H = white, O = red and Si = yellow

The terminal group of the NPs makes them hydrophilic because the hydroxyl groups (OH) can form hydrogen bonds with water and other molecules. The NP A, rich in silanol, has no hydroxyl group next to another. In contrast, model D, rich in the geminal group, has some hydroxyl groups that can hydrogen bond (weakly) to neighboring hydroxyl groups. However, the two OH in the geminal are oriented so that there is no hydrogen bond between them.

To analyze the NPs impact on the asphalt, we have added NPs A, D, and E to the neat ABG asphalt model built in Section 5.2. We then formed three modified models of asphalt named ABG_A, ABG_D, and ABG_E, respectively. The mass fraction of the mineral phase was chosen such that the modified asphalt models have around 3.5 $wt.$ % of the NP.

Packmol was used to construct the 3D bulk model of the modified ABG asphalt models. A cubic cell of $75 \times 75 \times 75$ Å was chosen. The SiO_2 NPs were placed in the center of the box and the docosane, 1,7-dimethylnaphthalene, resin-R, and asphaltene-A molecules were randomly distributed in the cubic cell. The bulk models of the modified ABG asphalt are shown in Figure 6.2 a), b), & c).

6.1.2 Molecular dynamics simulation

To study the density properties of the ABG_A, ABG_D, and ABG_E, MD simulations were conducted using LAMMPS [65]. To model the atomic interactions of hydroxylated SiO_2 systems with asphalt, we have employed CHARMM-based interatomic potential by Cruz-Chu *et al.* [97] which includes bond stretching and bending parameters obtained by Hill Jörg-R. and Sauer Joachim [98] and Lorenz Christian D. *et al.* [126]. The parameters of the Force Field are given in Appendix A.

A cutoff radius of 10 Å was applied for the Lennard-Jones (LJ) potential in SiO_2, while for the ABG, an internal 8.5 Å and external 10 Å cutoff radii were assigned for the CHARMM energy switching function. The Lorentz-Berthelot combination rule was utilized to obtaining the LJ cross parameters of two different nonbonded atoms. The PPPM [93, 119] method was used to overcome the long-range electrostatic interactions.

Initially, the systems were optimized and pre-equilibrated in the NVT ensemble for 400 ps simulation time and a time step of 0.5 fs in a fully periodic boundary condition with a cubic cell of $75 \times 75 \times 75$ Å. To reach the equilibrium state, MD simulations were performed in the NPT

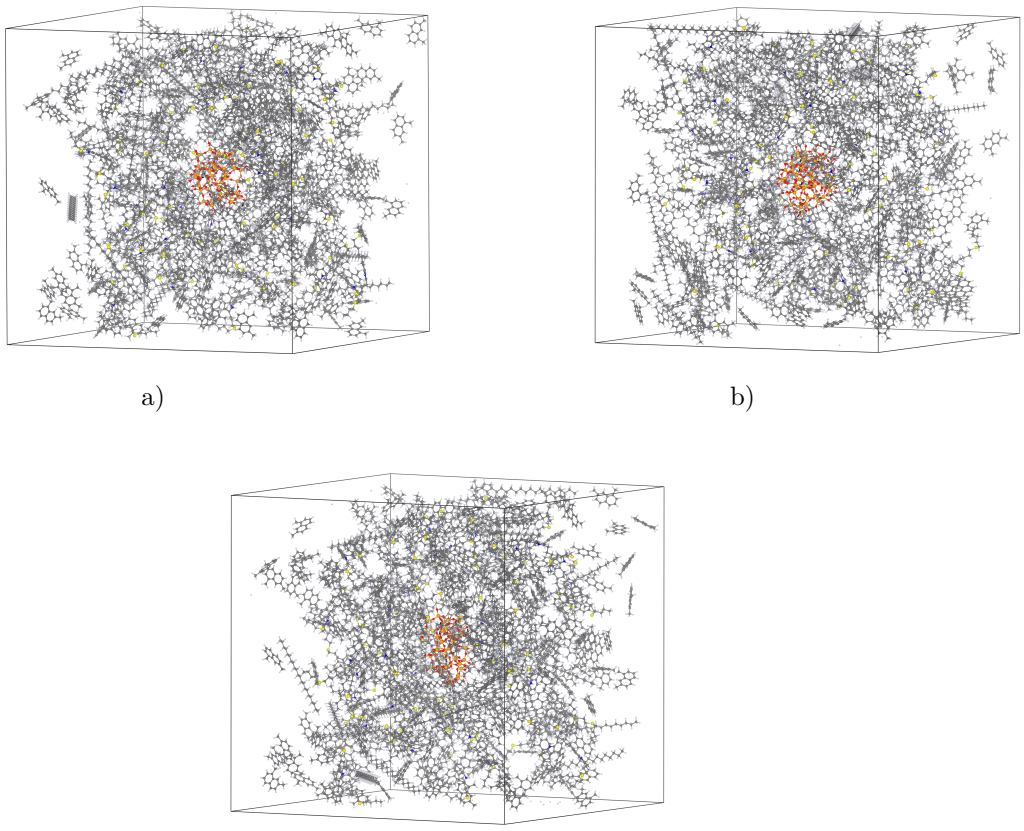

Figure 6.2: Bulk representation of the modified ABG asphalt model with SiO_2-NPs: a) ABG_A; b) ABG_D, and c) ABG_E. C = gray, H = white, N = blue, S = yellow O = red and Si = orange

ensemble at 1 atm pressure and a simulation time of 10ns. Controlled with the Nosé-hoover thermostat [122, 123] and the Parrinello-Rahman [127] barostat with the corrections proposed by Martyna *et al.* [128].

6.2 Densities of the modified ABG asphalt models

To validate the density calculations results, we have chosen a random sample of five different initial configurations for each of the modified asphalt models. The variation of density with respect to the simulation time step of two of the configurations of the ABG_A, ABG_D, and ABG_E models are shown in Figures 6.3, 6.4, and 6.5 respectively. The remaining configurations can be found in Appendix B.

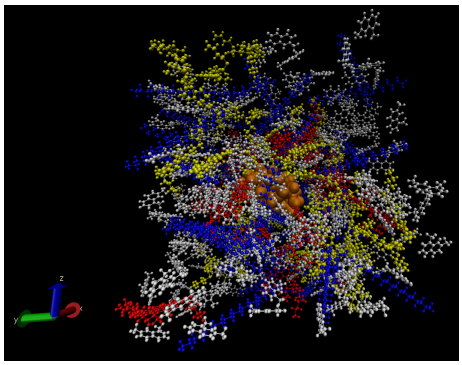

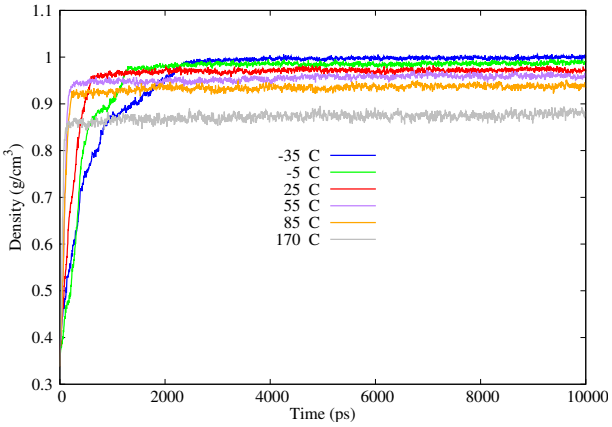

a) Configuration 1

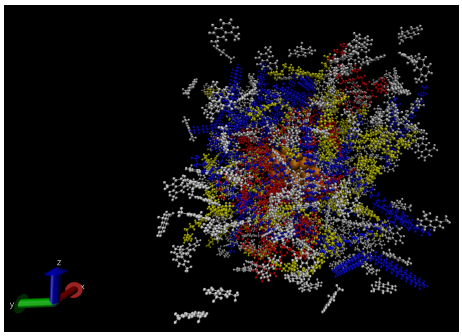

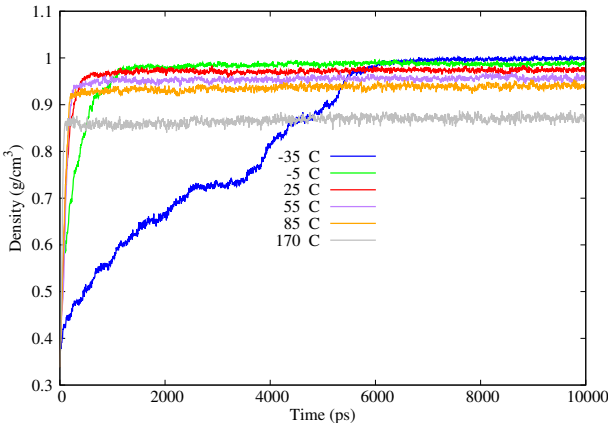

b) Configuration 2

Figure 6.3: Evolution of the density as a function of the simulation time in the MD simulation of five initial different configurations of the ABG_A asphalt model: blue = docosane; white = 1,7-dimethylnaphthalene; yellow = resin; red = asphaltene

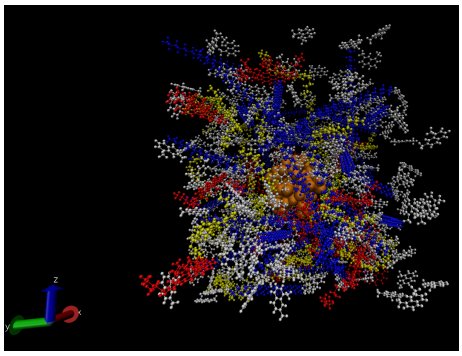

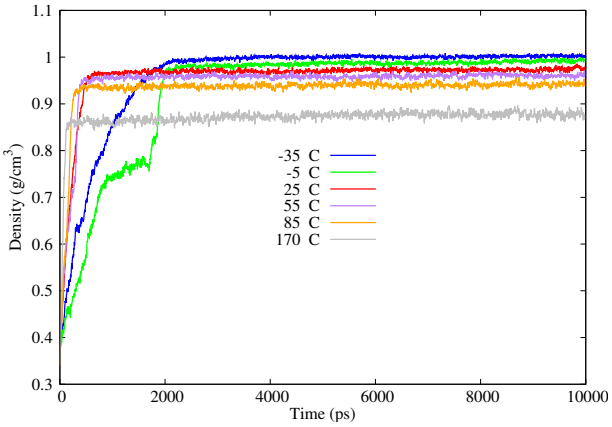

a) Configuration 1

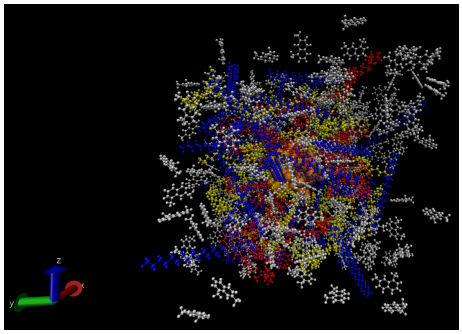

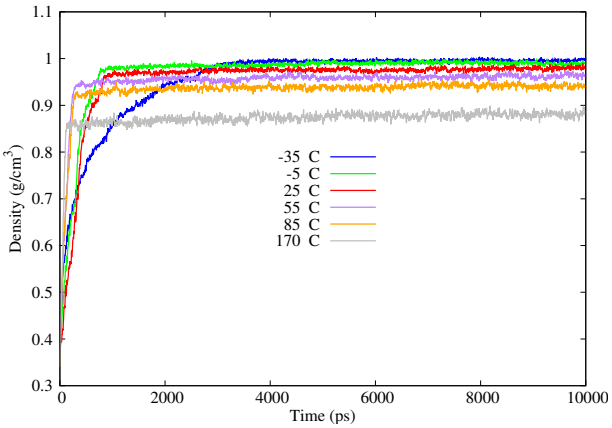

b) Configuration 2

Figure 6.4: Evolution of the density as a function of the simulation time in the MD simulation of five initial different configurations of the ABG_D asphalt model: blue = docosane; white = 1,7-dimethylnaphthalene; yellow = resin; red = asphaltene

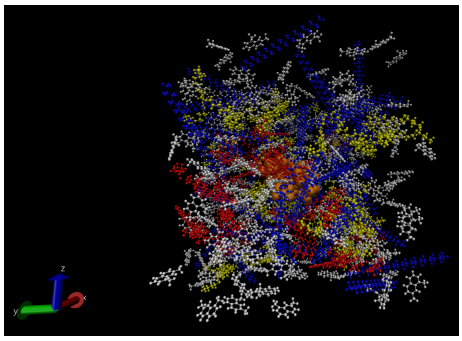

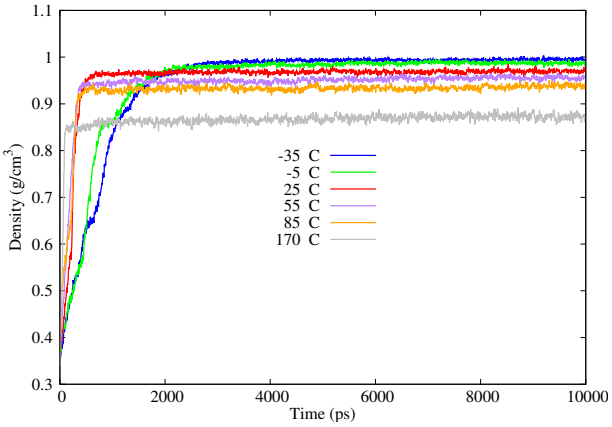

a) Configuration 1

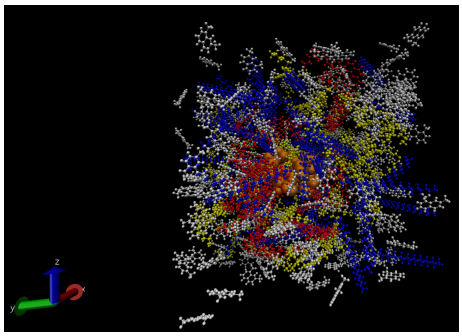

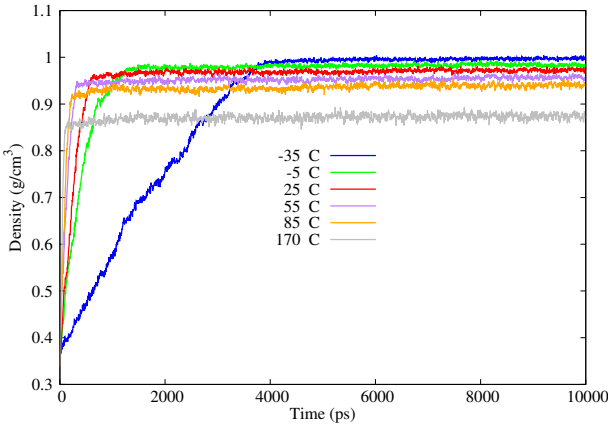

b) Configuration 2

Figure 6.5: Evolution of the density as a function of the simulation time in the MD simulation of five initial different configurations of the ABG_E asphalt model: blue = docosane; white = 1,7-dimethylnaphthalene; yellow = resin; red = asphaltene

The density converges faster when temperature increase and decreases monotonically with the temperature. The densities reached the plateau after a few simulations time for the higher temperatures. Whereas for the lower temperatures $-35\ ^oC$, we need more simulation time to reach the convergence. Because the system is denser, therefore, converges slowly.

To find out how the silica NPs modified the density property of the ABG model, we analyzed the temperature dependence of density. To calculate the densities at a given temperature, the densities were averaged in 10000 steps. The simulation results of the density change with temperature of the ABG_A, ABG_D, and ABG_E models are shown in Figures 6.6, 6.7, and 6.8 a) and b) respectively.

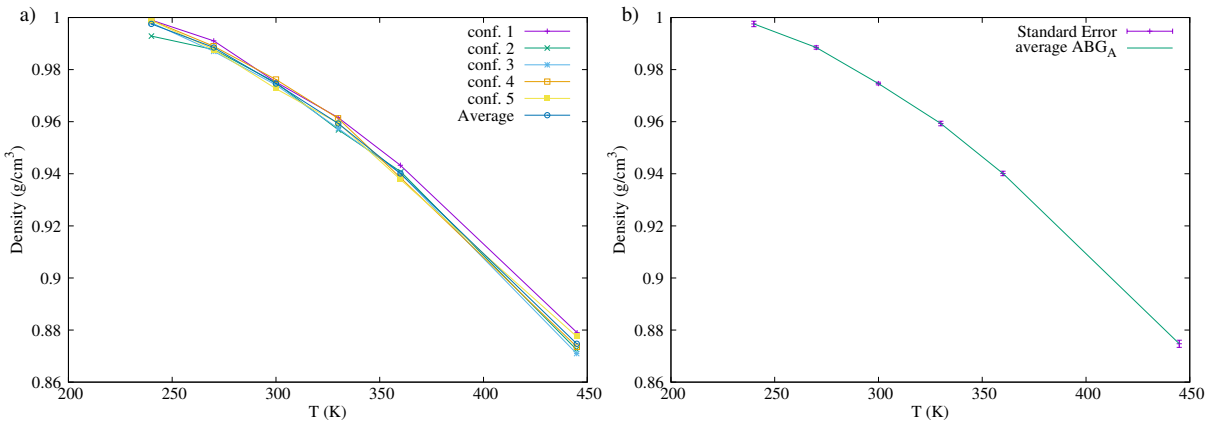

Figure 6.6: Density of the ABG_A model under different temperatures: a) density of the five different initial configurations; b) average density

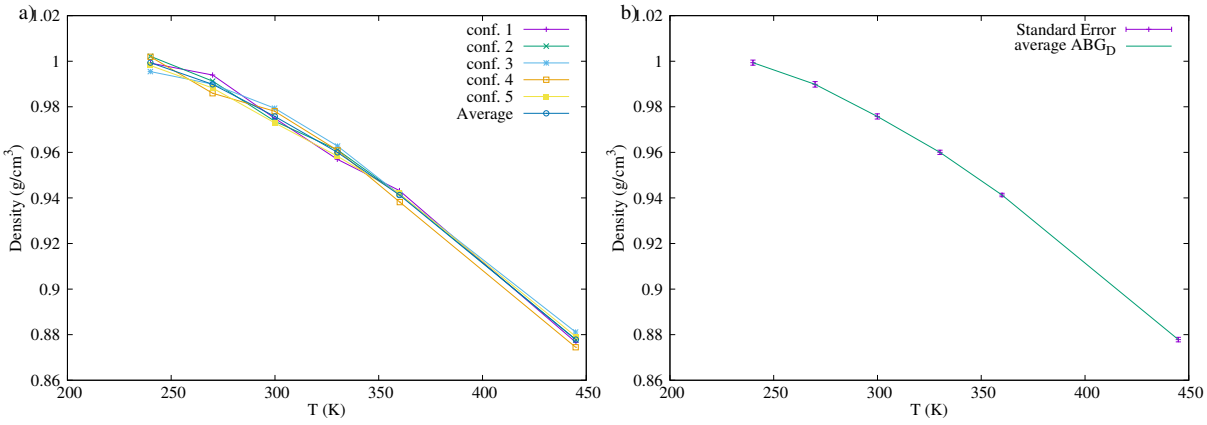

Figure 6.7: Density of the ABG_D model under different temperatures: a) density of the five different initial configurations; b) average density

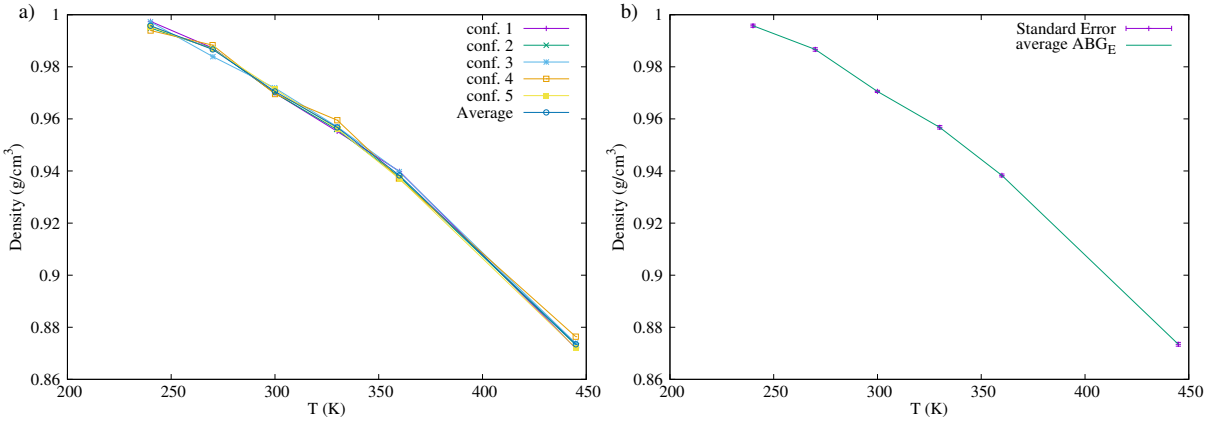

Figure 6.8: Density of the ABG_E model under different temperatures: a) density of the five different initial configurations; b) average density

The densities from the different initial configurations are similar as shown on the left-hand side of the Figures and also as the error of the average density on the right-hand side is very small. There is a consistency in the trend of the density for all the configurations as it decreases when the temperature increase. Figure 6.9 shows the change of the densities with the temperature of the ABG, ABG_A, ABG_D, and ABG_E.

The results indicate that the modified asphalt model's densities at different temperatures are higher than those of neat asphalt. We observed this property has just a slight dependence on the nanoparticles' surface coverage features. However, the modified asphalt with the SiO_2-NP that has the same amount of silanol and geminal group at the terminal has a slightly

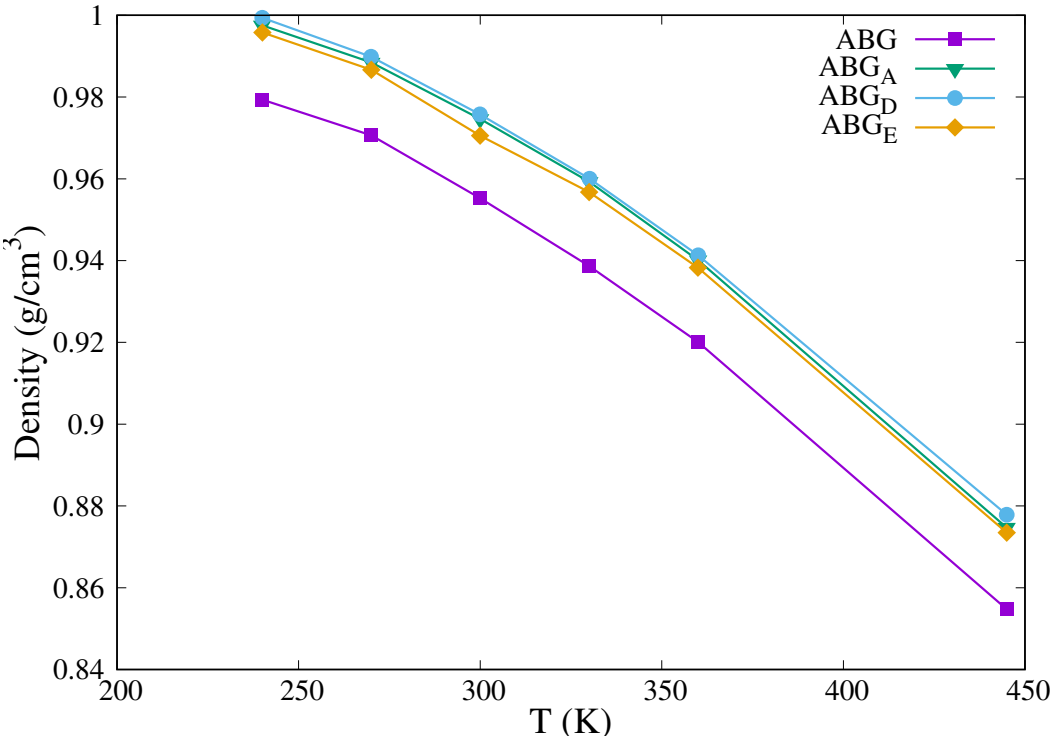

Figure 6.9: Density of the ABG and modified asphalt model ABG_A, ABG_D, and ABG_E under different temperatures.

lower density than that with different percentages of silanol and geminal groups.

6.3 Bulk modulus and Isothermal compressibility of the modified ABG asphalt models

The relationship between the bulk modulus and the temperature is depicted in Figure 6.10 a) with the corresponding isothermal compressibility in Figure 6.10 b). Asphalt is more easily compressed at high temperatures, i.e., its resistance to uniform compression is low. Whereas at lower temperatures, asphalts are more rigid and hence, its bulk modulus is high. Indeed, the isothermal compressibility increases with increasing temperature while the bulk modulus has an inverse behavior.

After the SiO_2-NPs were added, the bulk modulus of all the systems increased. Consequently, the isothermal compressibility decreased. In addition, for all cases studied, the bulk modulus of the neat phase is less than that of the modified ABG models i.e. the

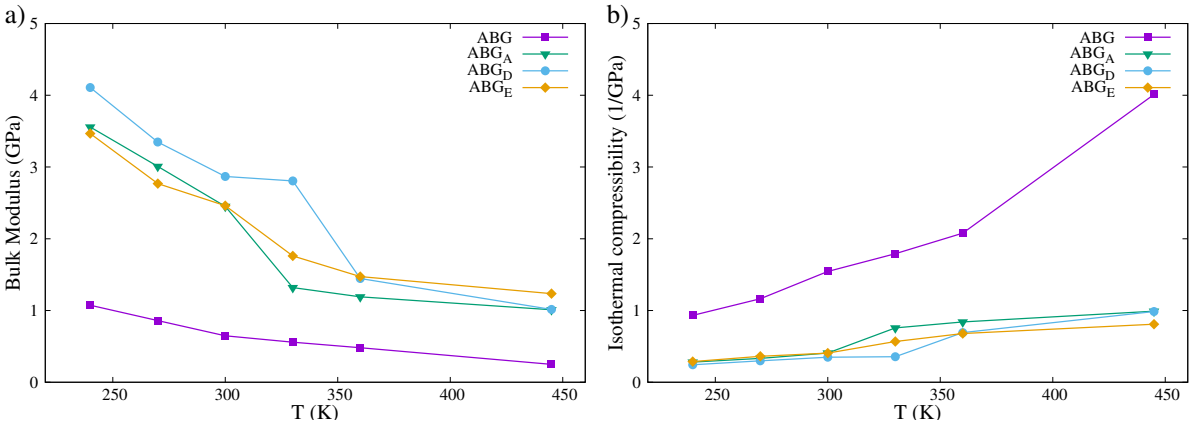

Figure 6.10: a) Bulk modulus and b) isothermal compressibility of the ABG and modified asphalt model ABG_A, ABG_D, and ABG_E under different temperatures in the MD simulations.

SiO_2-NPs significantly increase the compressive strength of the asphalt. This indicates that asphalts modified with silica nanoparticles are more likely to resist mechanical deformation in the road pavement. As a prevention against further deformation, the use of nanoparticles makes sense as it results in improved performance of asphalt. The bulk modulus and the isothermal compressibility trends with temperature remained the same for the three modified asphalt models.

As a result of our study, the addition of nanoparticles in asphalt modifies the physicochemical characteristics of the mixture. In particular, the bulk modulus increase plays a role in enhancing mechanical strength with an important impact on pavement roads by reducing plastic deformations. Besides, the SiO_2-NPs may be effective for tensile reinforcement of asphalt for wall junction purposes. Indeed, the capability of modifying the fluid mechanical properties with the addition of the nanoparticles and their relationship with the temperature may be essential to fine-tune the mechanical deformation rate in such applications.

6.4 Viscosity of the modified ABG asphalt models

The viscosity at a given temperature was averaged to obtain the relationship between the temperatures and viscosity. As shown in Figure 6.11, the viscosity of the ABG asphalt and modified models decreases as temperature increases and it has a similar trend with the other asphalt model in the literature [10, 18, 71].

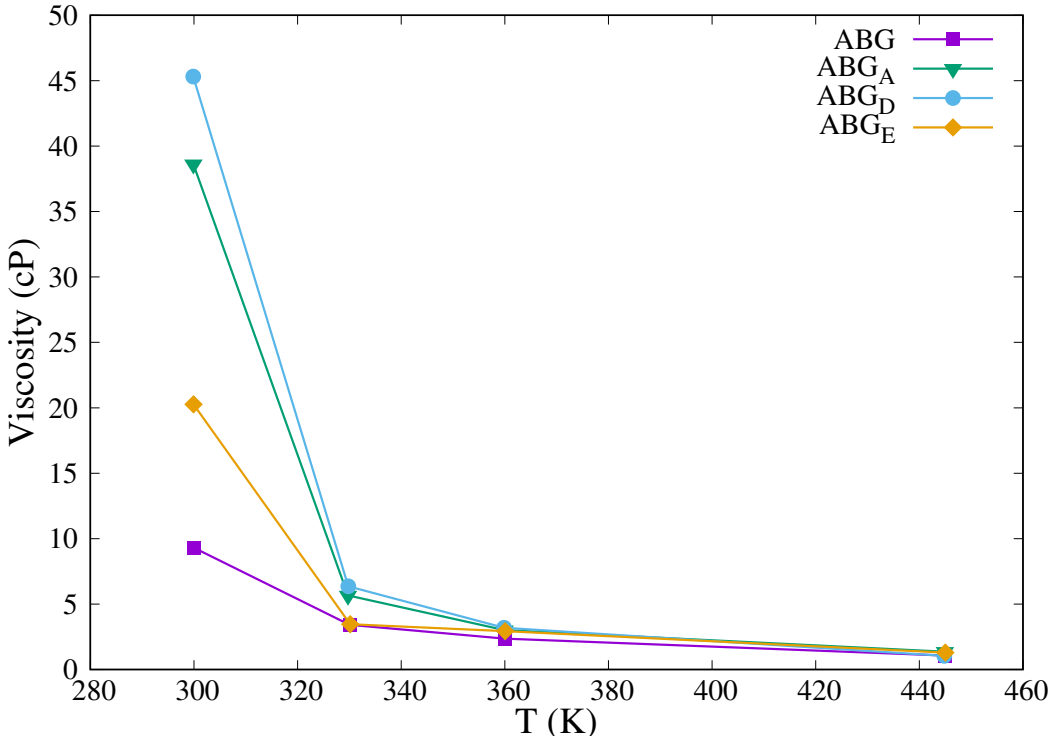

Figure 6.11: Viscosity of the ABG and modified asphalt model ABG_A, ABG_D, and ABG_E under different temperatures in the MD simulation.

The viscosities of all modified models displayed similar values as the neat asphalt at the typical pavement hot-mixing temperatures (see Figure 6.11). However, at lower temperatures, the nanoparticles play a central role by significantly increasing the viscosity. For instance, at the temperature of 25^oC, the modified asphalt with SiO_2-NP rich in the geminal group (ABG_D) has the highest viscosity (approximately 45.31 cP or four times higher than the pure phase). Regarding the nature of the nanoparticle, at room temperature, the viscosity of the modified asphalt is highly dependent on the hydrophilic coverage with the model containing a balance between silanol and geminal groups (ABG_E) displaying the lowest values compared to the other ones.

As seen, the ABG modified models' properties had significantly improved as the viscosity of the systems at a given temperature increased compared to the pure phase. Therefore, asphalt pavements containing nanoparticles are expected to be more resistant to gradual deformation at ambient temperature. Also, the NPs in asphalt can increase the cohesion effect, thus reducing the fluid segregation tendency. Since the silica nanoparticles tend to strongly

bind with the organic molecules, they may play an anti-stripping agent and possibly lower water's ability to penetrate the asphalt.

CHAPTER 7

CONCLUSIONS AND PERSPECTIVES

7.1 Conclusions

Motivated by the innovation on both production and performance of asphalt pavement, this thesis intended to use multi-scale atomistic simulations to model asphalt material and conducted studies of inorganic nanostructures to improve the physical properties of asphalt. Serving as a step toward more complex nanoaggregate studies with asphalt such as nanoclays. The asphalt description and properties were discussed in several steps. Firstly, the aggregation process of asphaltene and resin was carried out to understand the interaction mechanism in asphaltene aggregation which helps in the separation process of asphalt with the lighter part of crude oil. Next, different molecule types were chosen to represent the compounds found in real asphalts. Besides, the properties of asphalt including thermodynamic properties, and mechanical properties were investigated. Furthermore, the potential use of hydroxylated silica nanoparticles as additives for asphaltic material was conducted. The main findings and achievements of our work are summarized below.

Asphaltene and Resin simulations

Asphaltenes are molecules with large molecular size, high density, polar and active in certain fractions of petroleum. This set of molecules comprises one of the major problems within the oil industry. There is not yet a proposal of mechanism with first-principles calculations that explains the aggregation mechanism of asphaltene at the atomic-molecular level. Thus, we studied the electronic and structural properties of asphaltene and resin aggregates using DFT to explore this phenomenology. The possibility of obtaining reduced size aggregates with a large number of molecules in the aggregates and the understanding of elements involving in the asphaltene aggregation process in the crude oil is essential in the production of asphalt.

The description of the dimer to hexamer interaction of the asphaltene and resin molecule combinations was investigated in subsequent steps. In a first step, Molecular Docking was used for the first time in the asphaltene materials to determine the binding energy, the aggregates' size, and to select the more favorable conformational structures. Then, density functional theory (DFT) as implemented in quantum espresso was used to analyze the energetic, electronic, and structural properties of the aggregates.

The results provide aggregates with sizes between 3.67 Å and 22.25 Å which are less than the critical size of the asphaltene aggregates. The formation energy increases considerably from dimer to the hexamer with values between $-25.85\ kcal/mol$ and $-245.90\ kcal/mol$. The optimized structures of the aggregates with large aromatic rings are energetically more favorable because the interaction is mainly carried out by the $\pi-\pi$ stacking in the aromatic ring. The Kohn-Sham orbital highest occupied molecular orbital (HOMO) and lowest unoccupied molecular orbital (LUMO) are mainly localized in the aromatic ring with a small contribution near the sulfur (S) and nitrogen (N) in the isolated resin and the resin-resin dimer. The projected density of state (PDOS) analysis shows that aromatic carbon has the highest pick and the heteroatoms S are more reactive than N in the interaction process. The N seems to not affect the interaction with the increase of the aggregation.

This first part of our work contributes on one hand to the enhanced process of oil recovery by interacting some chemical composites with the different elements and sites which are more responsive in the formation of asphaltene aggregates. As our results have shown that aromatic C and S are the ones contributing most to the formation of the aggregates. Knowing this, it is

possible to put some chemical composites that could interact with these elements in order to break down the adhesive bonding and thus avoid the formation of the aggregates. Because the formation of the aggregates causes a problem in enhanced oil recovery such as blocking the pipeline and oil reservoir which reduces the rate of oil extraction. Besides, as our results have also shown, asphaltene with few aromatics rings together with N is less favorable to form aggregate and therefore, may be a good candidate to destabilize the aggregation process in the crude oil.

On the other hand, this work help as a step toward the production of asphalt. As our results have shown that we can obtain stable aggregates and reduced size aggregates with a large number of molecules, it is, therefore, possible to induce this situation so that it will be easy to separate the asphaltenes/asphalt with the lighter part of the crude oil before the refinery process. In this case, the more stable the asphaltene aggregates, the better the separation process and thus, finer production of asphalt.

Mixture composition

In this thesis, it was developed for the first time asphalt models for computer simulations base on Brazilian crude oil source. The results obtained in this work are promising to optimize asphalt materials and predict the physical properties at the macro-level. Physical, chemical, and mechanical properties are governed, in part, by the proportion of organic molecules. Providing a good molecular representation for MD input is important as the properties of asphalt depend largely on its chemical composition.

Based on the elemental analysis, mass fraction, and molecular class composition of the Brazilian/Laguna ABG crude oil source from SHRP, we have developed a molecular model of asphalt composed of four components: docosane, 1,7-dimethylnaphthalene, resin-R, and asphaltene-A. Different molecules were chosen to represent the components of the asphalt basing on their polarity, solubility, and molecular weight. The ABG model has a mass fraction of 19.1% *wt* docosane, 46.6% *wt* 1,7-dimethylnaphthalene, 18.7% *wt* resin-R, and 15.7% *wt* asphaltene-A.

Computational simulation is a powerful tool to investigate the effects of asphalt intrinsic properties. Molecular Dynamics simulations was used to obtain the properties of asphalt that

can be used at the macroscale level to predict the performance of asphalt pavement. MD was performed using the Large-scale Atomic / Molecular Massively Parallel Simulator (LAMMPS) software. The CHARMM force field was used to describe the interactions of molecules in the asphalt. MD was employed to investigate the thermodynamics and mechanical properties of the ABG asphalt model. Qualitatively, the trends of the physical properties of the ABG model were similar to that of real asphalt. The densities values from the MD simulation of the ABG model are closer to that of real asphalt compared to the other molecular models' asphalt in the literature. The simulation results indicate that the temperature-modulus trends of ABG models were compatible with the previously established models. The same trend was also observed with viscosity as it decreases with increasing temperature.

Asphalt and Nanoparticles mixture

Three sets of silica nanoparticles carrying at the surface different amounts of silanol ($i(OH)$) and geminal ($Si(OH)_2$) groups were used as additives to the ABG model. Namely 1) the NP A rich in silanol with 83% $Si(OH)$ and 17% $Si(OH)_2$ group; 2) the NP D rich in geminal with 17% $Si(OH)$ and 83% $Si(OH)_2$ group; 3) the last model E has a balance in silanol and geminal group with 50% $Si(OH)$ and 50% $Si(OH)_2$ group. The mass fraction of the hydroxylated SiO_2 NPs was chosen such that the modified asphalt models have around 3.5 $wt.$ % of the NP.

After the silica nanoparticles were added, the mechanical properties of the asphalt significantly improved. On one hand, the bulk modulus of the modified asphalt models is higher than that of the asphalt without the nanoparticles. Which shows an increase in the resistance of the asphalt to compressive or flexural strength. This mechanical behavior of the modified AGB models to have higher stress-strain compared to the neat ABG indicates that the modified models are the strongest and can sustain the highest tensile load.

On the other hand, when the silica nanoparticles are added, the resistance of the asphalt to gradual deformations caused by shear or tensile stress increase. Thus, preventing further crack propagation and failure that significantly impact the durability of the road pavement. Indicating a tendency toward suitable and durable asphalt pavement.

7.2 Perspectives for further work

Asphalt is a very complex material form by more than 10^6 different molecules. As molecular dynamics simulation is limited in terms of time and length scales, our choice of four types of molecules to represent the components in the ABG model had a hindrance to better achieve the description of the physicochemical properties of real asphalt. To finer represent the real asphalt, we recommend extending the number of types of molecules in the asphalt when doing MD simulation. Although currently, MD simulations may not allow achieving the millions of types of molecules present in the real asphalt. It may also be interesting to use MD simulations to study the aging and rejuvenation of asphalt.

The nanostructures that can be used to improve the performance of asphalt pavement include among others silica nanoparticles, carbon nanostructures, and nanoclays. MD simulation can be used to study and compare the improvement in the thermodynamics and mechanical properties of asphalt for each type of these nanostructures. It will be also interesting to use a different proportion of the nanostructures to see which quantity of nanostructures is suitable for the asphalt and overcome critical challenges faced by researchers in the measure and manipulation of nanostructure in the pavement. This contributes to the sustainability of asphalt pavement in the next generation.

APPENDIX A

FORCE FIELD PARAMETERS

A.1 Force Field for the ABG asphalt

The CHARMM Force Field used to describe interactions of atoms in the asphaltene, resin, 1,7-dimethylnaphthalene, and docosane consists of the bonded ($U_{bond},\ U_{ang},\ U_{di}$) and nonbonded ($U_{LJ},\ U_c$) potential terms as follow:

$$U(r1, r2, ..., rN) = U_{bond} + U_{ang} + U_{di} + U_{LJ} + U_c. \tag{A.1}$$

$$\begin{aligned} U_{bond} &= \sum_r K_r(r - r_0)^2 \\ U_{ang} &= \sum_\theta K_\theta(\theta - \theta_0)^2 \\ U_{di} &= \sum_\phi K_\phi(1 + cos(n\phi - \delta)). \end{aligned} \tag{A.2}$$

$$U_{LJ} = \sum_{ij} 4\epsilon \left[\left(\frac{\sigma}{r_{ij}} \right)^{12} - \left(\frac{\sigma}{r_{ij}} \right)^{6} \right]$$
$$U_c = \sum_{ij} \frac{q_i q_j}{\epsilon r_{ij}}. \tag{A.3}$$

The parameters $r_0,\ \theta_0,\ \delta,\ K_r,\ K_\theta,$ and K_ϕ, as well as partial charges q_i, and the Lennard-Jones parameters σ, ϵ (shown in the Tables below) are taken from the CHARMM General Force Field (CGenFF) version 4.0 [95, 96].

Table A.1: Non bonded parameters for the ABG asphalt model

Atom species	q_i (e)	ϵ $(kcal/mol)$	σ (Å)
CG2R61	-0.115	0.07000	3.55005
CG331	-0.266	0.07800	3.65268
HGR61	0.115	0.03000	2.42004
HGA3	0.090	0.02400	2.38761
CG311	-0.091	0.03200	3.56360
CG321	-0.178	0.05600	3.58141
SG311	-0.242	0.45000	3.56360
HGA2	0.090	0.03500	2.38761
HGA1	0.090	0.04500	2.38761
NG2R51	-0.551	0.20000	3.29632
CG2R51	0.097	0.05000	3.74178
CG2RC0	0.059	0.09900	3.31414
HGP1	0.363	0.04600	0.40001
HGR51	0.176	0.03000	2.42004

Table A.2: Bond stretching parameters for the ABG asphalt model

	K_r $(kcal/mol$ Å$^2)$	r_0 (Å)
CG2R61-CG2R61	305.00	1.375
CG2R61-CG331	230.00	1.490
CG2R61-HGR61	340.00	1.080
CG331-HGA3	322.00	1.111
CG2R61-CG311	230.00	1.490
CG2R61-CG321	230.00	1.490
CG311-CG321	222.50	1.538
CG311-HGA1	309.00	1.111
CG321-HGA2	309.00	1.111
CG311-CG311	222.50	1.500
CG321-CG331	222.50	1.528
CG311-CG331	222.50	1.538
CG321-CG321	222.50	1.530
CG321-SG311	198.00	1.818
NG2R51-CG2R51	400.00	1.380
NG2R51-CG2RC0	300.00	1.375
NG2R51-HGP1	474.00	1.010
CG2R51-CG2R51	410.00	1.360
CG2R51-CG321	229.63	1.500
CG2R51-CG2RC0	350.00	1.430
CG2R51-HGR51	350.00	1.080
CG2RC0-CG2RC0	360.00	1.385
CG2RC0-CG2R61	300.00	1.360

Table A.3: Angle bending parameters for the ABG asphalt model

	K_θ $(kcal/mol\ rad^2)$	θ_0 $(^o)$
CG2R61-CG2R61-CG2R61	40.00	120.0
CG2R61-CG2R61-CG331	45.80	120.0
CG2R61-CG2R61-HGR61	30.00	120.0
CG2R61-CG331-HGA3	49.30	107.5
HGA3-CG331-HGA3	35.50	108.4
CG2R61-CG2R61-CG311	45.80	120.0
CG2R61-CG311-CG321	51.80	107.5
CG2R61-CG311-HGA1	43.00	111.0
CG2R61-CG2R61-CG321	45.80	120.0
CG2R61-CG321-CG311	51.80	107.5
CG2R61-CG321-HGA2	49.30	107.5
CG311-CG321-CG311	58.35	113.5
CG311-CG321-HGA2	33.43	110.1
CG321-CG311-CG321	58.35	113.5
CG321-CG311-HGA1	34.50	110.1
CG311-CG321-CG321	58.35	113.5
CG321-CG311-CG311	53.35	111.0
HGA2-CG321-HGA2	35.50	109.0
CG311-CG311-HGA1	34.50	110.1
CG311-CG321-CG331	58.35	113.5
CG321-CG331-HGA3	34.60	110.1
CG331-CG321-HGA2	34.60	110.1
CG321-CG311-CG331	53.35	114.0
CG311-CG331-HGA3	33.43	110.1
CG331-CG311-HGA1	34.50	110.1
CG321-CG321-CG331	58.00	115.0

CG321-CG321-HGA2	26.50	110.1
CG321-CG321-CG321	58.35	113.6
CG321-CG321-SG311	58.00	114.5
CG321-SG311-CG321	34.00	95.0
SG311-CG321-HGA2	46.10	111.3
NG2R51-CG2R51-CG2R51	130.00	106.0
NG2R51-CG2R51-CG321	45.80	124.0
CG2R51-NG2R51-CG2RC0	85.00	110.0
CG2R51-NG2R51-HGP1	30.00	125.5
NG2R51-CG2RC0-CG2RC0	100.00	105.7
NG2R51-CG2RC0-CG2R61	130.00	132.6
CG2RC0-NG2R51-HGP1	28.00	126.0
CG2R51-CG2R51-CG2RC0	85.00	105.7
CG2R51-CG2R51-HGR51	32.00	126.4
CG2R51-CG2R51-CG321	45.80	130.0
CG2R51-CG321-HGA2	55.00	109.5
CG2R51-CG2RC0-CG2RC0	85.00	108.0
CG2R51-CG2RC0-CG2R61	130.00	132.0
CG2RC0-CG2R51-HGR51	32.00	126.4
CG2RC0-CG2RC0-CG2R61	50.00	120.0
CG2RC0-CG2R61-CG2R61	50.00	120.0
CG2RC0-CG2R61-HGR61	30.00	120.0
CG2R61-CG321-CG321	51.80	107.5

Table A.4: Dihedral parameters for the ABG asphalt model

	K_ϕ $(kcal/mol)$	n	δ $(^o)$
HGA2-CG321-CG321-SG311	0.0100	3	0
CG2R61-CG2R61-CG2R61-CG2R61	3.1000	2	180
CG2R61-CG2R61-CG2R61-HGR61	4.2000	2	180
CG2R51-CG2R51-CG2RC0-CG2R61	3.0000	2	180
CG2R51-CG2R51-CG321-HGA2	0.0000	3	0
CG2R51-CG2RC0-CG2RC0-CG2R61	1.5000	2	180
CG2R51-CG2RC0-CG2R61-CG2R61	4.0000	2	180
CG2R51-CG2RC0-CG2R61-HGR61	4.0000	2	180
HGR51-CG2R51-CG2RC0-CG2RC0	2.6000	2	180
HGR51-CG2R51-CG2RC0-CG2R61	2.8000	2	180
CG2RC0-CG2RC0-CG2R61-CG2R61	3.0000	2	180
CG2RC0-CG2RC0-CG2R61-HGR61	3.0000	2	180
CG2RC0-CG2R61-CG2R61-CG2R61	3.0000	2	180
CG2RC0-CG2R61-CG2R61-HGR61	3.0000	2	180
CG2R61-CG2RC0-CG2RC0-CG2R61	3.0000	2	180
CG2R61-CG2R61-CG2R61-CG2R61	3.1000	2	180
CG2R61-CG2R61-CG2R61-CG321	3.1000	2	180
HGR61-CG2R61-CG2R61-CG2R61	4.2000	2	180
HGR61-CG2R61-CG2R61-HGR61	2.4000	2	180
CG2R61-CG2R61-CG321-CG311	0.2300	2	180
CG2R61-CG2R61-CG321-HGA2	0.0020	6	0
HGR61-CG2R61-CG2R61-CG321	2.4000	2	180
CG2R61-CG2R61-CG321-CG321	0.2300	2	180
CG2R61-CG321-CG311-HGA1	0.0400	3	0
CG2R61-CG321-CG321-HGA2	0.0400	3	0
CG321-CG311-CG321-CG321	0.2000	3	0

CG321-CG311-CG321-HGA2	0.1950	1	0
CG2R61-CG2R61-CG2R61-CG331	3.1000	2	180
CG2R61-CG2R61-CG331-HGA3	0.0020	6	0
CG331-CG2R61-CG2R61-HGR61	2.4000	2	180
HGR61-CG2R61-CG2R61-HGR61	2.4000	2	180
CG2R61-CG2R61-CG2R61-CG2R61	3.1000	2	180
CG2R61-CG2R61-CG2R61-HGR61	4.2000	2	180
CG2R61-CG2R61-CG2R61-CG311	3.1000	2	180
CG2R61-CG2R61-CG311-CG321	0.2300	2	180
CG2R61-CG2R61-CG311-HGA1	0.1000	6	180
HGR61-CG2R61-CG2R61-CG311	2.4000	2	180
CG2R61-CG311-CG321-HGA2	0.0000	3	0
CG2R61-CG2R61-CG2R61-CG321	3.1000	2	180
HGR61-CG2R61-CG2R61-HGR61	2.4000	2	180
CG2R61-CG2R61-CG321-CG311	0.2300	2	180
CG2R61-CG2R61-CG321-HGA2	0.0020	6	0
CG2R61-CG321-CG311-HGA1	0.0400	3	0
CG2R61-CG321-CG311-CG331	0.0400	3	0
CG321-CG2R61-CG2R61-HGR61	2.4000	2	180
CG311-CG321-CG311-CG311	0.2000	3	0
CG311-CG321-CG311-HGA1	0.1950	3	0
CG321-CG311-CG321-CG321	0.2000	3	0
CG321-CG311-CG321-HGA2	0.1950	1	0
CG311-CG321-CG321-CG321	0.5000	3	0
CG311-CG321-CG321-CG321	0.5000	6	180
CG311-CG321-CG321-HGA2	0.1950	3	0
CG321-CG311-CG321-CG311	0.2000	3	0
HGA1-CG311-CG321-HGA2	0.1950	3	0
HGA1-CG311-CG321-CG321	0.1950	3	0

CG321-CG311-CG311-CG321	0.5000	4	180
CG321-CG311-CG311-HGA1	0.1950	3	0
HGA2-CG321-CG311-CG311	0.1950	3	0
CG311-CG311-CG321-CG331	0.2000	3	0
HGA1-CG311-CG311-HGA1	0.1950	3	0
CG311-CG321-CG331-HGA3	0.1600	3	0
HGA1-CG311-CG321-CG331	0.2000	3	0
HGA2-CG321-CG331-HGA3	0.1600	3	0
CG321-CG311-CG331-HGA3	0.2000	3	0
HGA2-CG321-CG311-CG331	0.2000	3	0
HGP1-NG2R51-CG2RC0-CG2RC0	0.8500	2	180
HGP1-NG2R51-CG2RC0-CG2R61	0.2000	2	180
CG2R51-CG2R51-CG2RC0-CG2RC0	4.0000	2	180
CG331-CG311-CG321-CG321	0.2000	3	0
HGA1-CG311-CG331-HGA3	0.1950	3	0
CG321-CG321-CG331-HGA3	0.1600	3	0
HGA2-CG321-CG321-CG331	0.1800	3	0
HGA2-CG321-CG321-HGA2	0.2200	3	0
CG321-CG321-CG321-CG321	0.0645	2	0
CG321-CG321-CG321-CG321	0.1497	3	180
CG321-CG321-CG321-CG321	0.0945	4	0
CG321-CG321-CG321-CG321	0.1125	5	0
CG321-CG321-CG321-HGA2	0.1950	3	0
CG321-CG321-CG321-SG311	0.1950	3	0
CG321-CG321-SG311-CG321	0.2400	1	180
CG321-CG321-SG311-CG321	0.3700	3	0
CG321-SG311-CG321-HGA2	0.2800	3	0
CG321-CG321-CG321-CG331	0.1505	2	0
CG321-CG321-CG321-CG331	0.0813	3	180

HGP1-NG2R51-CG2R51-CG2R51	1.0000	2	180
HGP1-NG2R51-CG2R51-CG321	1.0000	2	180
HGA2-CG321-CG311-HGA1	0.1950	3	0
CG311-CG321-CG321-HGA2	0.1950	3	0
CG311-CG321-CG321-CG321	0.5000	3	0
CG311-CG321-CG321-CG321	0.5000	6	180
CG321-CG321-CG321-CG331	0.1082	4	0
CG321-CG321-CG321-CG331	0.2039	5	0
CG321-CG321-CG321-CG321	0.0645	2	0
CG321-CG321-CG321-CG321	0.1497	3	180
CG321-CG321-CG321-CG321	0.0945	4	0
CG321-CG321-CG321-CG321	0.1125	5	0
CG321-CG321-CG321-HGA2	0.1950	3	0
HGA2-CG321-CG321-HGA2	0.2200	3	0
CG321-CG321-CG321-CG331	0.1505	2	0
CG321-CG321-CG321-CG331	0.0813	3	180
CG321-CG321-CG321-CG331	0.1082	4	0
CG321-CG321-CG321-CG331	0.2039	5	0
CG321-CG321-CG331-HGA3	0.1600	3	0
HGA2-CG321-CG321-CG331	0.1800	3	0
HGA2-CG321-CG331-HGA3	0.1600	3	0
NG2R51-CG2R51-CG2R51-CG2RC0	4.0000	2	180
NG2R51-CG2R51-CG2R51-HGR51	3.5000	2	180
NG2R51-CG2R51-CG321-HGA2	0.1900	3	0
CG2R51-NG2R51-CG2RC0-CG2RC0	1.5000	2	180
CG2R51-NG2R51-CG2RC0-CG2R61	1.5000	2	180
NG2R51-CG2RC0-CG2RC0-CG2R51	6.5000	2	180
NG2R51-CG2RC0-CG2RC0-CG2R61	1.5000	2	180
CG2RC0-NG2R51-CG2R51-CG2R51	5.0000	2	180

NG2R51-CG2RC0-CG2R61-CG2R61	3.0000	2	180
HGA1-CG311-CG321-CG321	0.1950	3	0
HGA2-CG321-CG321-HGA2	0.2200	3	0
CG321-CG321-CG321-SG311	0.1950	3	0
CG321-CG321-CG321-HGA2	0.1950	3	0
CG321-CG321-SG311-CG321	0.2400	1	180
CG321-CG321-SG311-CG321	0.3700	3	0
HGA2-CG321-CG321-SG311	0.0100	3	0
CG321-SG311-CG321-HGA2	0.2800	3	0
CG321-CG321-CG321-CG331	0.1505	2	0
CG321-CG321-CG321-CG331	0.0813	3	180
CG321-CG321-CG321-CG331	0.1082	4	0
CG321-CG321-CG321-CG331	0.2039	5	0
CG321-CG321-CG331-HGA3	0.1600	3	0
HGA2-CG321-CG321-CG331	0.1800	3	0
HGA2-CG321-CG331-HGA3	0.1600	3	0

A.2 Cruz-Chu Force Field for SiO_2

The parameters of the CHARMM-based interatomic potential by Cruz-Chu employed for the SiO_2 nanoparticles are shown in Table A.5 and A.6. These parameters are adapted from the Refs [97, 98].

Table A.5: Non bonded parameters for the SiO_2 nanoparticle

Species	Symbol	q_i (e)	ϵ $(kcal/mol)$	σ (Å)
surface Hydrogen	HS	+0.4320	0.0460	0.449
Oxigen of the bulk Silicon	OSb	-0.4500	0.1500	3.500
Oxigen of the surface Silicon	OSs	-0.6579	0.1521	3.540
bulk Silicon	Sib	+0.9000	0.3000	4.295
surface Silicon	Sis	+0.9010	0.3000	4.295

Table A.6: bonded parameters for the SiO_2 nanoparticle

	Bond stretch	
	K_r $(kcal/mol.\text{Å}^2)$	$(r - r_0)$ (Å)
HS-OSs	545.00000	0.96
OSb-Sis	885.09998	1.61
OSs-Sis	428.00000	1.42
OSb-Sis	885.09998	1.61
	Angle bending	
	K_θ $(kcal/mol.rad^2)$	$(\theta - \theta_0)$ $(^o)$
HS-OSs-Sis	57.50000	106.00
OSb-Sis-OSs	153.25999	111.09
OSb-Sis-OSb	89.62000	116.26
Sis-OSb-Sis	4.66000	174.22
OSs-Sis-OSs	89.62000	116.26
Sis-OSb-Sib	4.66000	174.22
OSb-Sib-OSb	159.57001	110.93
Sib-OSb-Sib	4.66000	174.22

APPENDIX B

DENSITY CONVERGENCE TEST

Here we provided complementary results about the density convergence test of some initial configurations of the ABG and modified ABG asphalt models.

B.1 Densities the ABG asphalt

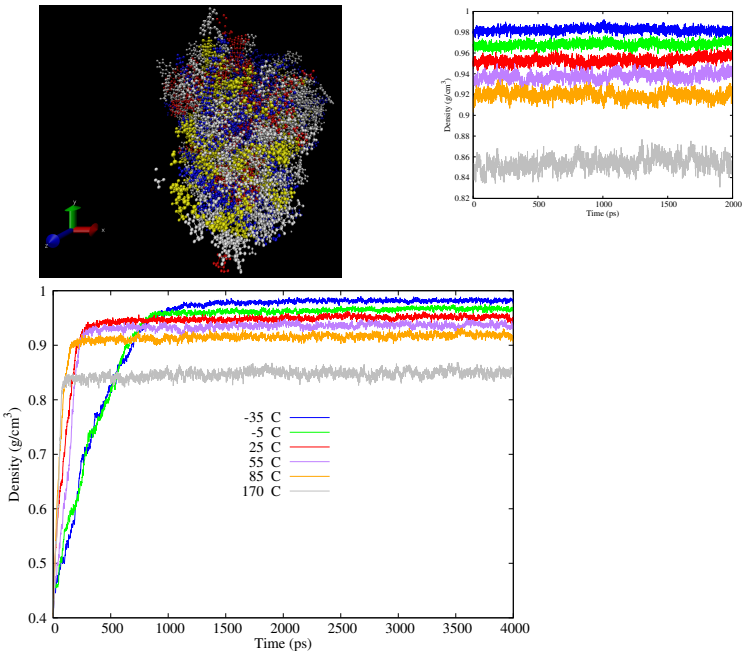

a) Configuration 3

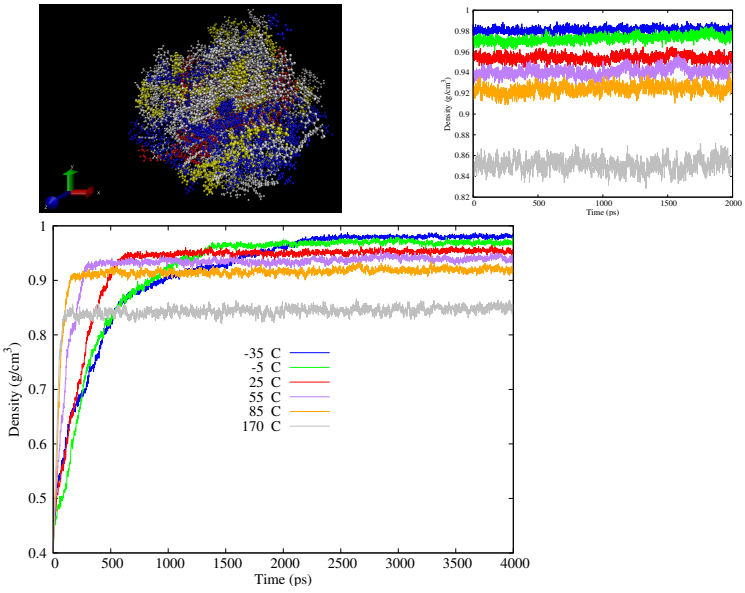

b) Configuration 4

Figure B.1: Evolution of the density as function of the simulation time in the MD simulation for 10 initial different configurations: blue = docosane; white = 1,7-dimethylnaphthalene; yellow = resin; red = asphaltene

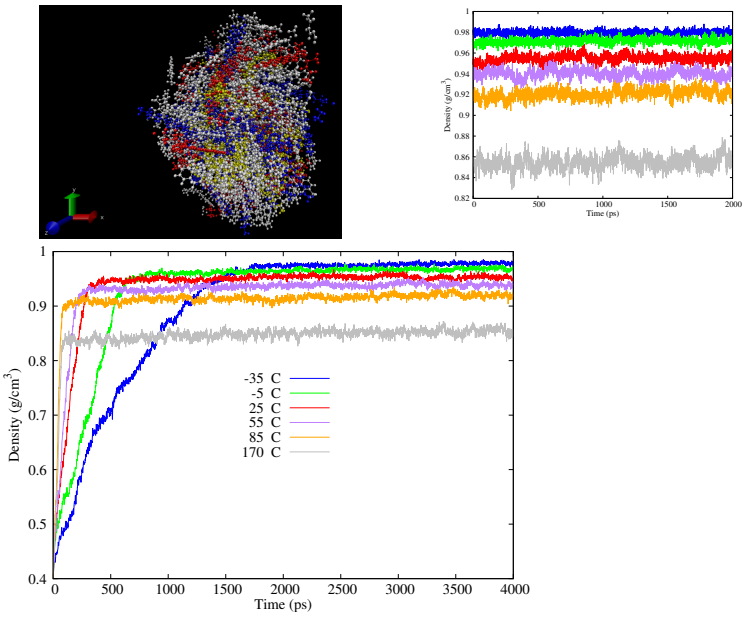

a) Configuration 5

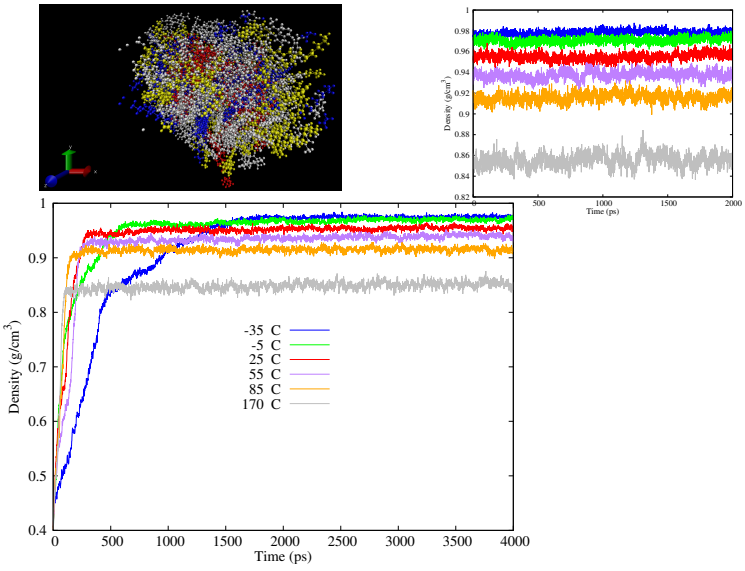

b) Configuration 6

Figure B.2: Evolution of the density as function of the simulation time in the MD simulation for 10 initial different configurations: blue = docosane; white = 1,7-dimethylnaphthalene; yellow = resin; red = asphaltene

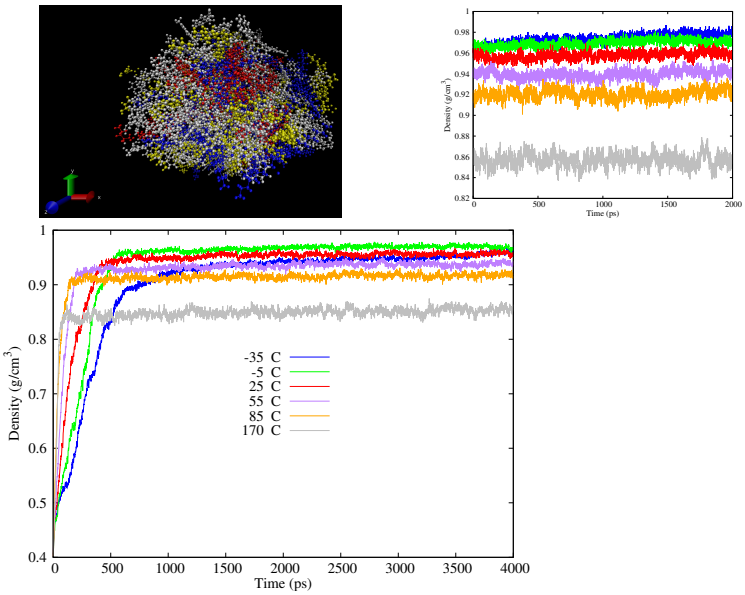

a) Configuration 7

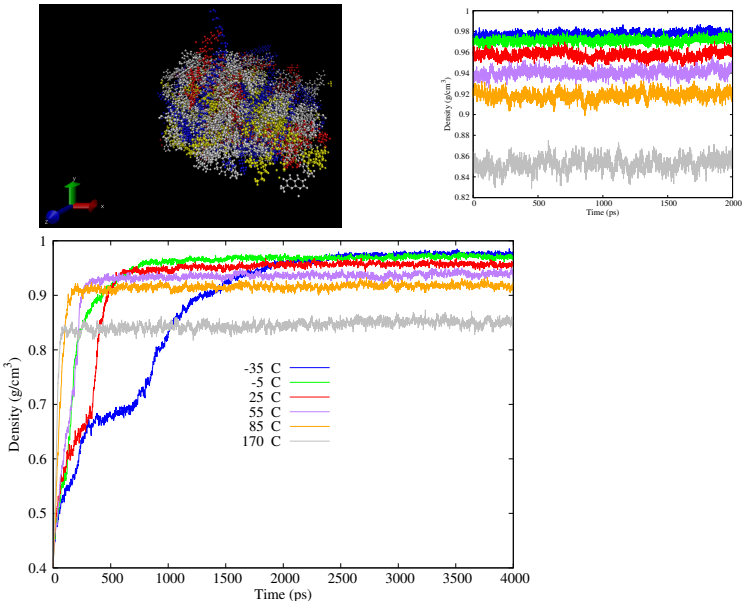

b) Configuration 8

Figure B.3: Evolution of the density as function of the simulation time in the MD simulation for 10 initial different configurations: blue = docosane; white = 1,7-dimethylnaphthalene; yellow = resin; red = asphaltene

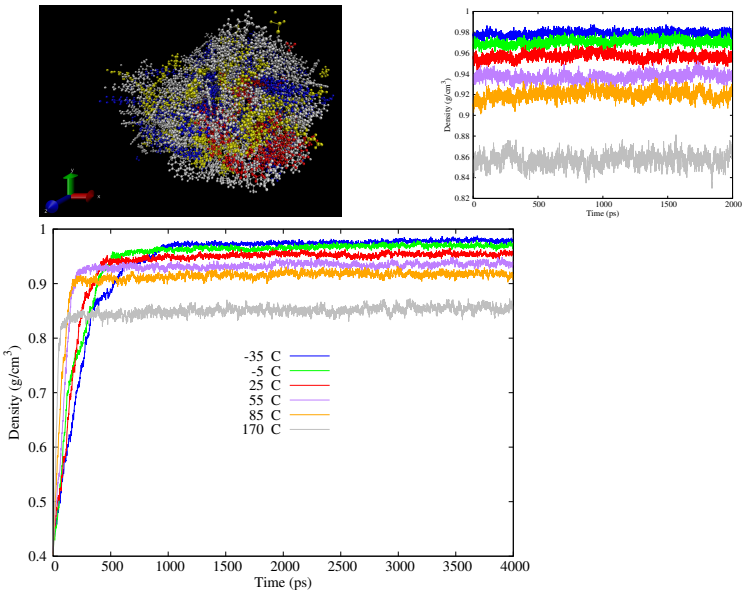

a) Configuration 9

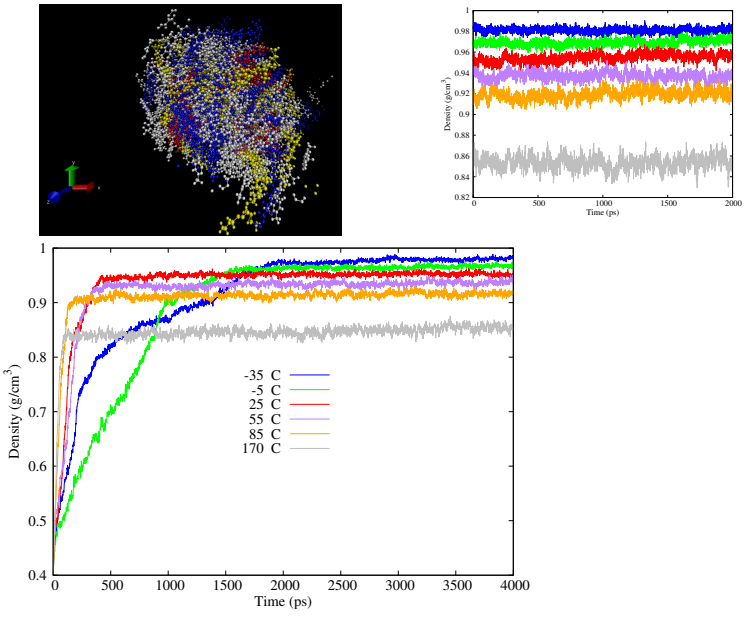

b) Configuration 10

Figure B.4: Evolution of the density as function of the simulation time in the MD simulation for 10 initial different configurations: blue = docosane; white = 1,7-dimethylnaphthalene; yellow = resin; red = asphaltene

B.2 Densities the modified ABG asphalt

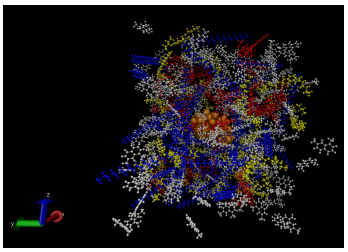

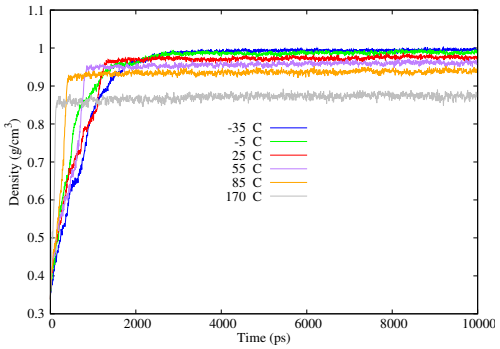

a) Configuration 3

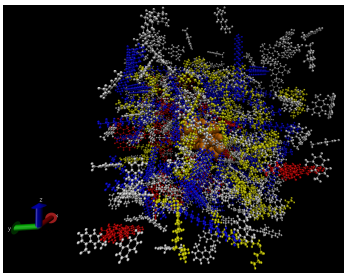

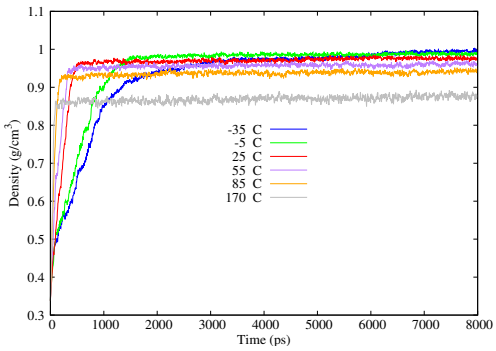

b) Configuration 4

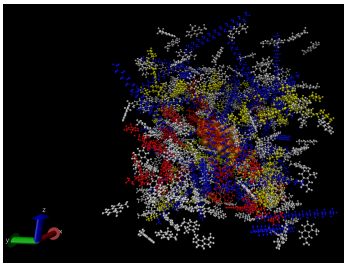

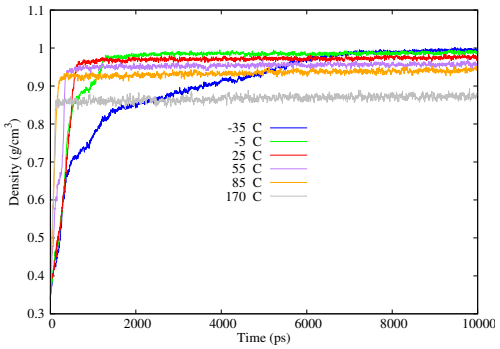

c) Configuration 5

Figure B.5: Evolution of the density as a function of the simulation time in the MD simulation of five initial different configurations of the ABG_A asphalt model: blue = docosane; white = 1,7-dimethylnaphthalene; yellow = resin; red = asphaltene

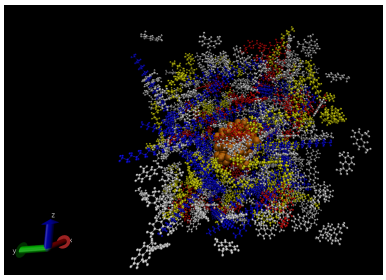

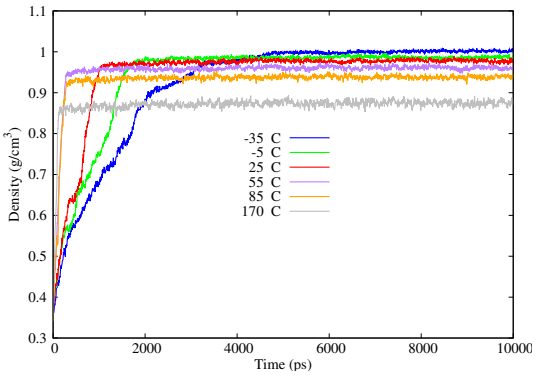

a) Configuration 3

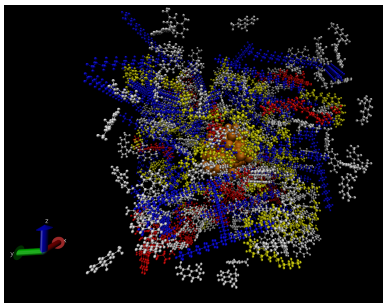

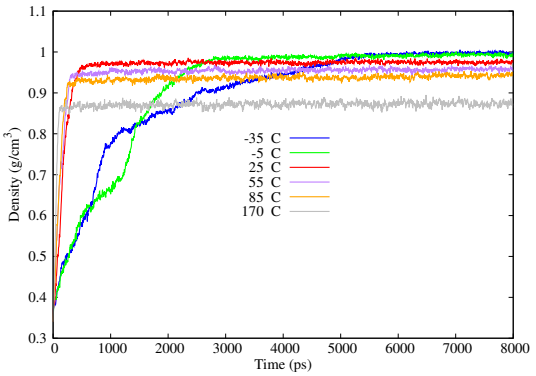

b) Configuration 4

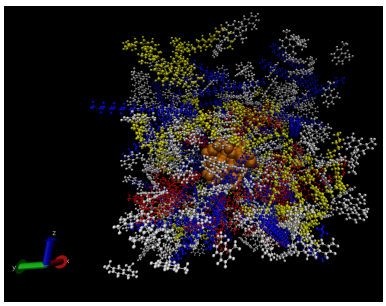

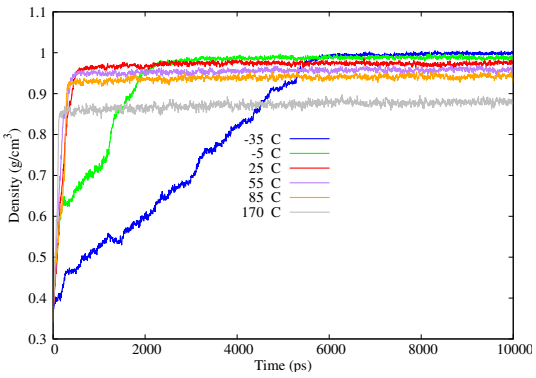

c) Configuration 5

Figure B.6: Evolution of the density as a function of the simulation time in the MD simulation of five initial different configurations of the ABG_D asphalt model: blue = docosane; white = 1,7-dimethylnaphthalene; yellow = resin; red = asphaltene

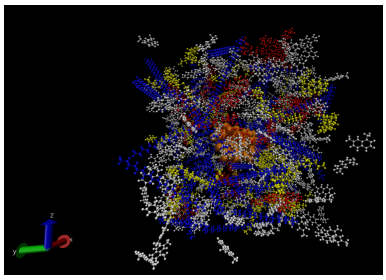

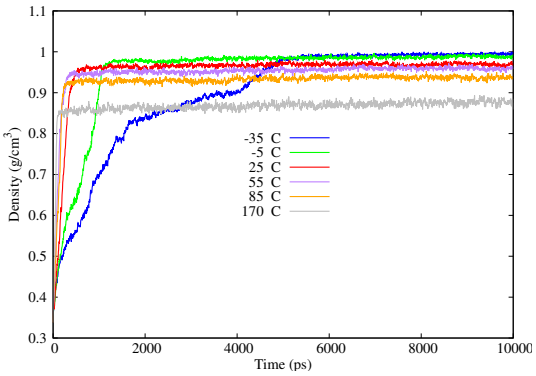

a) Configuration 3

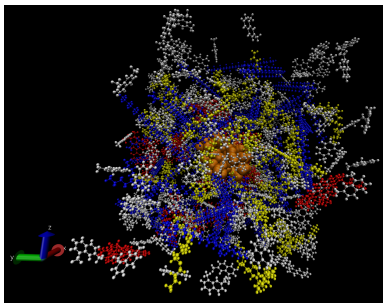

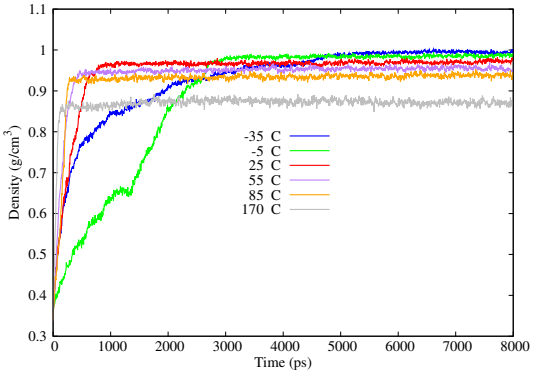

b) Configuration 4

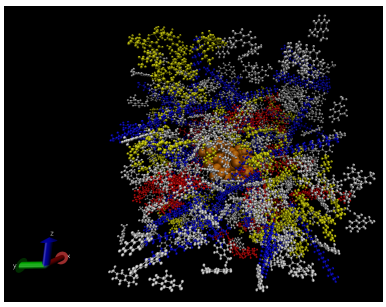

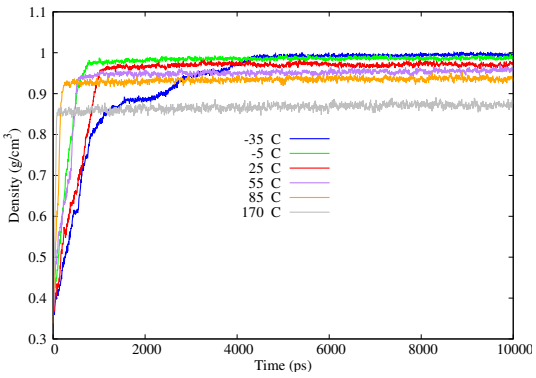

c) Configuration 5

Figure B.7: Evolution of the density as a function of the simulation time in the MD simulation of five initial different configurations of the ABG_E asphalt model: blue = docosane; white = 1,7-dimethylnaphthalene; yellow = resin; red = asphaltene

APPENDIX C

VISCOSITY

A good asphalt quality often requires the binder attributes which can be referred to as its rheological properties. In road engineering, hot mixed asphalt is produced and homogenized at various temperatures, so the mix can be pumped and poured easily. The properties of asphalt can be optimized by testing its viscosity and monitoring the rheological parameters to describe its stiffness and compliance. One way to evaluate the viscosity is through computer simulation. In the LAMMPS package, there are many methods to calculate the viscosity based on non-equilibrium MD (NEMD). In this appendix, we have shown the details of the Müller-Plathe method [68] to calculate the shear viscosity.

C.1 Müller Plathe's Method for Viscosity

The method to calculate the shear viscosity of a fluid is based on the fact that the proportionality coefficient of the shear field with the flux of transverse linear momentum is the shear viscosity as shown in Equation C.1. The shear field is a one-component velocity gradient (let us say the x component) with respect to another direction (let us say the z-direction) $\frac{\partial v_x}{\partial z}$. The momentum flux $j_z(p_x)$ is the x component of the momentum P_x flowing perpendicular to

flux direction (z) at a given time t and per unit area A (see Equation C.1).

$$J_z(p_x) = -\eta \frac{\partial v_x}{\partial z}$$
$$J_z(p_x) = \frac{P_x}{2tA}. \tag{C.1}$$

Where $J_z(p_x)$ is the momentum flux which is also the x component of the momentum flowing in the z-direction per given time t and unit area A. The momentum flux is in units of momentum/area/time; $\frac{\partial v_x}{\partial z}$ is the velocity gradient of the fluid moving in the x-direction normal to the momentum flux, η is the shear viscosity of the fluid which thus has units of pressure-time ($kg.m^{-1}.s^{-1} = 1P$), P_x is the total momentum which is the sum of the Δp_x, A is the area which is equal to the box length $Lx \times Ly$ and t is the simulation length. Factor 2 came from the periodicity of the system.

The momentum flux is imposed on the fluid and the periodic simulation box is subdivided into many layers along the z-direction as shown in Figure C.1. The atoms inside the layer at $z = 0$ moves in the $+x$ direction, whereas those inside the layer at $z = L_z/2$ in the $-x$ direction, and are repeated periodically. L_z is the simulation box length. The highest amount of momentum transferred is found in layer $z = 0$ and the smallest amount in layer $z = L_z/2$ and vice versa. Therefore, the momentum of the pair atoms in the two layers is interchanged. The momentum is then conserved if the two atoms have the same mass. Since the atomic positions are unchanged, the potential energy and, thus, the total energy of the system is conserved. thus, the momentum is conserved.

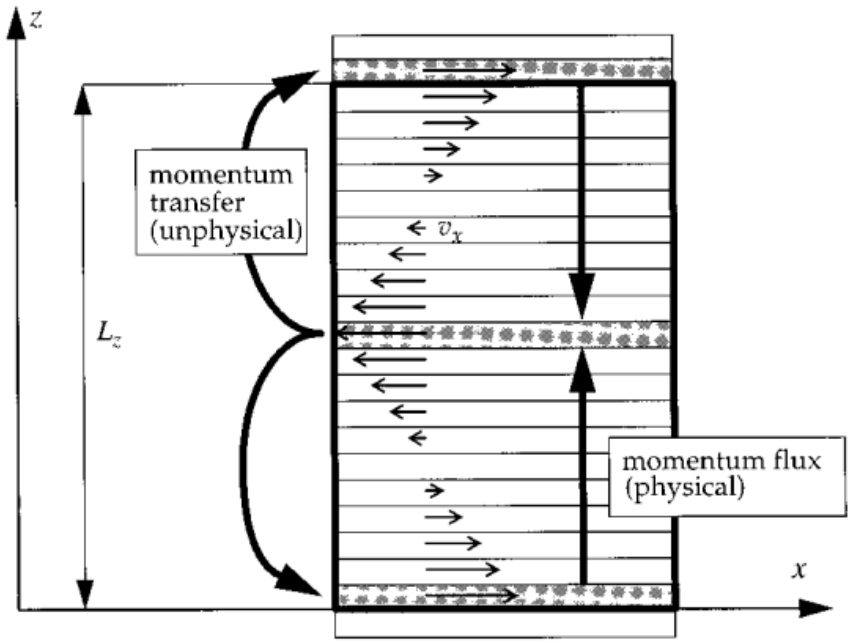

Figure C.1: Schematic view of the momentum flux transfer in the periodic simulation box [68]

In LAMMPS, the Müller-Plathe algorithm uses a reverse non-equilibrium MD (rNEMD) simulation. The cause-and-effect in the usual NEMD is reversed in the sense that the effect, the momentum flux or stress, is imposed on the system, whereas the cause, the velocity gradient or shear rate, is the system's response from the simulation. This algorithm implies a simple exchange of particle momenta, which can be easily implemented. Then, the resulting velocity profile is a sturdy property that converges rapidly.

REFERENCES

[1] EAPA. What is asphalt. https://eapa.org/what-is-asphalt/, 2016.

[2] Amir Yousif Rana and Abd Tayh Sady. *Asphalt Chemistry Lectures notes*. Highway and Transportation Engineering, Al-Mustansiriyah University, 2018.

[3] J. Krishnan Murali. *The physical and chemical structure of asphalt: with a brief history of their usage and availability*. Cambridge University press, 2006.

[4] EAPA. Asphalt the 100% recyclable construction product. https://eapa.org/wp-content/uploads/2019/11/EAPApaper-2.pdf, 2014.

[5] EAPA and NAPA. The asphalt paving industry a global perspective second edition. https://eapa.org/wp-content/uploads/2018/07/GL101-2nd-Edition.pdf, 2011.

[6] Sunil Bukey. Petroleum asphalt market trends 2018 and their impact on global industry 2025. https://www.egypt-business.com/ticker/details/1814-Petroleum-Asphalt-Market-Trends-2018-and-their-Impact-on-Global-Industry-2025/255634, 2018.

[7] Terry E. Ronald and Rogers J. Brandon. *Applied Petroleum Reservoir Engineering, 3rd edition*. Published by Prentice Hall, 2014.

[8] Sharif Hamadi Adel. *Petroleum Refining lecture note for Fourth Class*. University of Technology Chemical Engineering Department, 2020.

[9] CNT and SEST SENAT. Pesquisa cnt de rodovias 2019. https://pesquisarodovias.cnt.org.br/, 2019.

[10] Michael L. Greenfield and Liqun Zhang. Developing model asphalt systems using molecular simulation : final model., 2009.

[11] R. Jones David and W. Kennedy Thomas. THE ASPHALT MODEL: Results of the SHRP Asphalt Research Program., 1991.

[12] Liqun Zhang and Michael L. Greenfield. Analyzing properties of model asphalts using molecular simulation. *Energy & Fuels*, 21(3):1712–1716, 2007.

[13] Liqun Zhang and Michael L. Greenfield. Relaxation time, diffusion, and viscosity analysis of model asphalt systems using molecular simulation. *The Journal of Chemical Physics*, 127(19):194502, 2007.

[14] R. Jones David. SHRP materials reference library, asphalt cements: a concise data compilation., 1993.

[15] Levent Artok, Yan Su, Yoshihisa Hirose, Masahiro Hosokawa, Satoru Murata, and Masakatsu Nomura. Structure and reactivity of petroleum-derived asphaltene. *Energy & Fuels*, 13(2):287–296, 1999.

[16] Yue Hou, Linbing Wang, Dawei Wang, Xin Qu, and Jiangfeng Wu. Using a molecular dynamics simulation to investigate asphalt nano-cracking under external loading conditions. *Applied Sciences*, 7:770, 2017.

[17] Hao Wang, Enqiang Lin, and Guangji Xu. Molecular dynamics simulation of asphalt-aggregate interface adhesion strength with moisture effect. *International Journal of Pavement Engineering*, 18:1–10, 2015.

[18] Hui Yao, Qingli Dai, and Zhanping You. Molecular dynamics simulation of physicochemical properties of the asphalt model. *Fuel*, 164:83 – 93, 2016.

[19] Mohd Ezree Abdullah, Ahmad Kemas, Kemas Zamhari, Rosnawati Buhari, Nurul Hidayah Mohd Kamaruddin, Mohd Kamaruddin, Nafarizal Nayan, Mohd Rosli Hainin, Norhidayah Hassan, Ramadhansyah Putra Jaya, Nur Izzi, and Nur Izzi Md. Yusoff. A review on the exploration of nanomaterials application in pavement engineering. *Jurnal Teknologi*, 73:4–2015, 2015.

[20] Mao hua Zhang and Hui Li. Pore structure and chloride permeability of concrete containing nano-particles for pavement. *Construction and Building Materials*, 25(2):608 – 616, 2011.

[21] H. Li, Mao hua Zhang, and J. Ou. Abrasion resistance of concrete containing nano-particles for pavement. *Wear*, 260:1262–1266, 2006.

[22] Hui Li, Mao hua Zhang, and Jin ping Ou. Flexural fatigue performance of concrete containing nano-particles for pavement. *International Journal of Fatigue*, 29(7):1292 – 1301, 2007.

[23] Hui Yao, Qingli Dai, Zhanping You, Andreas Bick, Min Wang, and Shuaicheng Guo. Property analysis of exfoliated graphite nanoplatelets modified asphalt model using molecular dynamics (md) method. *Applied Sciences*, 7(1), 2017.

[24] Hui Yao, Zhanping You, Liang Li, Xianming Shi, Shu Wei Goh, Julian Mills-Beale, and David Wingard. Performance of asphalt binder blended with non-modified and polymer-modified nanoclay. *Construction and Building Materials*, 35:159 – 170, 2012.

[25] Jinzhou Liu, Bin Yu, and Qianzhe Hong. Molecular dynamics simulation of distribution and adhesion of asphalt components on steel slag. *Construction and Building Materials*, 255:119332, 2020.

[26] D. Makimura, C. Metin, T. Kabashima, T. Matsuoka, Q. P. Nguyen, and Caetano R. Miranda. Combined modeling and experimental studies of hydroxylated silica nanoparticles. *Journal of Materials Science*, 45(18):5084–5088, 2010.

[27] S. de Lara Lucas, A. Rigo Vagner, F. Michelon Mateus, O. Metin Cigdem, P. Nguyen Quoc, and R. Miranda Caetano. Molecular dynamics studies of aqueous silica nanoparticle dispersions: salt effects on the double layer formation. *Journal of Physics: Condensed Matter*, 27(32), 2015.

[28] Vagner A. Rigo, Lucas S. de Lara, and Caetano R. Miranda. Energetics of formation and hydration of functionalized silica nanoparticles: An atomistic computational study. *Applied Surface Science*, 292:742 – 749, 2014.

[29] Lucas De Lara, Mateus Michelon, Cigdem Omurlu, Quoc Nguyen, and Caetano Miranda. Interface tension of silica hydroxylated nanoparticle with brine: A combined experimental and molecular dynamics study. *The Journal of chemical physics*, 136:164702, 2012.

[30] Caetano Rodrigues Miranda, Lucas Stori de Lara, and Bruno Costa Tonetto. *SPE-157033-MS*, chapter Stability and Mobility of Functionalized Silica Nanoparticles for Enhanced Oil Recovery Applications, page 11. Society of Petroleum Engineers, Noordwijk, The Netherlands, 2012.

[31] Lucas S. de Lara, Vagner A. Rigo, and Caetano R. Miranda. The stability and interfacial properties of functionalized silica nanoparticles dispersed in brine studied by molecular dynamics. *The European Physical Journal B*, 88(10):261, 2015.

[32] Derek D. Li and Michael L. Greenfield. Chemical compositions of improved model asphalt systems for molecular simulations. *Fuel*, 115:347 – 356, 2014.

[33] Luke W. Corbett. Composition of asphalt based on generic fractionation, using solvent deasphaltening, elution-adsorption chromatography, and densimetric characterization. *Analytical Chemistry*, 41(4):576–579, 1969.

[34] Juan Gallego, Ana Rodríguez-Alloza, and Rebeca Antón. Influence of the naphthenic-aromatic content of the base binder on the characteristics of crumb rubber modified binders and asphalt mixtures. *Sustainability*, 11:3927, 2019.

[35] Pavement Interactive. Asphalt production and oil refining. https://pavementinteractive.org/reference-desk/materials/asphalt/asphalt-production-and-oil-refining/, 2020.

[36] LLC Refinery Automation Institute. Asphalt cement. http://www.madehow.com/Volume-2/Asphalt-Cement.html, 2020.

[37] T.W. Kennedy and Strategic Highway Research Program (U.S.). Superior performing asphalt pavements (superpave): the product of the shrp asphalt research program, 1994.

[38] Thomas F. Headen, Edo S. Boek, and Neal T. Skipper. Evidence for asphaltene nanoaggregation in toluene and heptane from molecular dynamics simulations. *Energy & Fuels*, 23(3):1220–1229, 2009.

[39] Juan Murgich, Rodríguez, and Yosslen Aray. Molecular recognition and molecular mechanics of micelles of some model asphaltenes and resins. *Energy & Fuels*, 10(1):68–76, 1996.

[40] Mohammad Sedghi, Lamia Goual, William Welch, and Jan Kubelka. Effect of asphaltene structure on association and aggregation using molecular dynamics. *The Journal of Physical Chemistry B*, 117(18):5765–5776, 2013.

[41] Chen Z., Zhang L., Zhao S., Shi Q., and Xu C. Molecular structure and association behavior of petroleum asphaltene. *Structure and Modeling of Complex Petroleum Mixtures. Structure and Bonding*, 168(18):5765–5776, 2015.

[42] Salah Yaseen and G. Ali Mansoori. Asphaltene aggregation due to waterflooding (a molecular dynamics study). *Journal of Petroleum Science and Engineering*, 170:177 – 183, 2018.

[43] Lucas Grillo Celia-Silva, Patricia B. Vilela, Pedro Morgado, Elizabete F. Lucas, Luis F. G. Martins, and Eduardo J. M. Filipe. Preaggregation of Asphaltenes in the Presence of Natural Polymers by Molecular Dynamics Simulation. *Energy & Fuels*, 34(2):1581–1591, 2020.

[44] Edris Joonaki, Aliakbar Hassanpouryouzband, Rod Burgass, Alfred Hase, and Bahman Tohidi. Effects of Waxes and the Related Chemicals on Asphaltene Aggregation and Deposition Phenomena: Experimental and Modeling Studies. *ACS OMEGA*, 5(13):7124–7134, 2020.

[45] H. Santos Silva, A. Alfarra, G. Vallverdu, D. Begue, B. Bouyssiere, and I Baraille. Role of the porphyrins and demulsifiers in the aggregation process of asphaltenes at water/oil interfaces under desalting conditions: a molecular dynamics study. *Petroleum Science*, 17(3):797–810, 2020.

[46] Thomas Headen, Edo Boek, George Jackson, Tim Totton, and Erich Müller. Simulation of asphaltene aggregation through molecular dynamics: Insights and limitations. *Energy & Fuels*, 31, 2017.

[47] Amin Bemani, Abdolrahman Poozesh, Masoud Bahrami, and Siavash Ashoori. Experimental study of asphaltene deposition: Focus on critical size and temperature effect. *Journal of Petroleum Science and Engineering*, 181:106186, 2019.

[48] INSIGHT/DISCOVER. Biosym technologies, 1994.

[49] E. Rogel. Studies on asphaltene aggregation via computational chemistry. *Colloids and Surfaces A: Physicochemical and Engineering Aspects*, 104(1):85 – 93, 1995.

[50] Estrella Rogel. Simulation of interactions in asphaltene aggregates. *Energy & Fuels*, 14, 2000.

[51] Alexandre N.M. Carauta, Júlio C.G. Correia, Peter R. Seidl, and Daniel M. Silva. Conformational search and dimerization study of average structures of asphaltenes. *Journal of Molecular Structure: THEOCHEM*, 755(1):1 – 8, 2005.

[52] Robert C. Rizzo and William L. Jorgensen. Opls all-atom model for amines: Resolution of the amine hydration problem. *Journal of the American Chemical Society*, 121(20):4827–4836, 1999.

[53] Wolfgang Damm, Antonio Frontera, Julian Tirado–Rives, and William L. Jorgensen. Opls all-atom force field for carbohydrates. *Journal of Computational Chemistry*, 18(16):1955–1970, 1997.

[54] Sander Pronk, Szilárd Páll, Roland Schulz, Per Larsson, Pär Bjelkmar, Rossen Apostolov, Michael R. Shirts, Jeremy C. Smith, Peter M. Kasson, David van der Spoel, Berk Hess, and Erik Lindahl. GROMACS 4.5: a high-throughput and highly parallel open source molecular simulation toolkit. *Bioinformatics*, 29(7):845–854, 2013.

[55] Filipe Camargo Dalmatti Alves Lima, Raphael Alvim, and Caetano Miranda. From single asphaltenes and resins to nanoaggregates: A computational study. *Energy & Fuels*, 31, 2017.

[56] Edo S. Boek, Dmitry S. Yakovlev, and Thomas F. Headen. Quantitative molecular representation of asphaltenes and molecular dynamics simulation of their aggregation. *Energy & Fuels*, 23(3):1209–1219, 2009.

[57] Edo S. Boek, Thomas F. Headen, and Johan T. Padding. Multi-scale simulation of asphaltene aggregation and deposition in capillary flow. *Faraday Discuss.*, 144:271–284, 2010.

[58] Kazeem A. Lawal, John P. Crawshaw, Edo S. Boek, and Velisa Vesovic. Experimental investigation of asphaltene deposition in capillary flow. *Energy & Fuels*, 26(4):2145–2153, 2012.

[59] David A. Storm, Stephen J. DeCanio, Maureen M. DeTar, and Vincent P. Nero. Upper bound on number average molecular weight of asphaltenes. *Fuel*, 69(6):735 – 738, 1990.

[60] D. A. Storm, J. C. Edwards, S. J. DeCanio, and E. Y. Sheu. Molecular representations of ratawi and alaska north slope asphaltenes based on liquid- and solid-state nmr. *Energy & Fuels*, 8(3):561–566, 1994.

[61] Henning Groenzin and Oliver C. Mullins. Molecular size and structure of asphaltenes from various sources. *Energy & Fuels*, 14(3):677–684, 2000.

[62] Liqun Zhang and Michael L. Greenfield. Effects of polymer modification on properties and microstructure of model asphalt systems. *Energy & Fuels*, 22(5):3363–3375, 2008.

[63] R. E. Robertson, J. F. Branthaver, P. M. Harnsberger, J. C. Petersen, S. M. Dorrence, J. F. McKay, T. F. Turner, A. T. Pauli, S.-C. Huang, J.-D. Huh, J. E. Tauer, K. P. Thomas, D. A. Netzel, F. P. Miknis, T. Williams, J. J. Duvall, F. A. Barbour, and C. Wright. Fundamental properties of asphalts and modified asphalts volume I: Interpretive report. Technical Report FHWA-RD-99-212, 2001.

[64] Derek D. Li and Michael L. Greenfield. Chemical compositions of improved model asphalt systems for molecular simulations. *Fuel*, 115:347 – 356, 2014.

[65] Steve Plimpton. Fast parallel algorithms for short-range molecular dynamics. *Journal of Computational Physics*, 117(1):1 – 19, 1995.

[66] Friedrich Ritschl, Martin Fait, Klaus Fiedler, Jutta E. H. Köhler, Bernd Kubias, and Manfred Meisel. An extension of the consistent valence force field (cvff) with the aim to simulate the structures of vanadium phosphorus oxides and the adsorption of n-butane and of 1-butene on their crystal planes. *Zeitschrift für anorganische und allgemeine Chemie*, 628(6):1385–1396, 2002.

[67] Wendy D. Cornell, Piotr Cieplak, Christopher I. Bayly, Ian R. Gould, Kenneth M. Merz, David M. Ferguson, David C. Spellmeyer, Thomas Fox, James W. Caldwell, and Peter A. Kollman. A second generation force field for the simulation of proteins, nucleic acids, and organic molecules. *Journal of the American Chemical Society*, 117(19):5179–5197, 1995.

[68] F. Müller-Plathe. Reversing the perturbation in nonequilibrium molecular dynamics: An easy way to calculate the shear viscosity of fluids. *Physical Review E - Statistical Physics, Plasmas, Fluids, and Related Interdisciplinary Topics*, 59(5):4894–4898, 1999.

[69] Arash Motamed, Amit Bhasin, and Kenneth Liechti. Using the poker-chip test for determining the bulk modulus of asphalt binders. *Mechanics of Time-Dependent Materials*, 18, 2014.

[70] Hui Yao, Qingli Dai, Zhanping You, Andreas Bick, and Min Wang. Modulus simulation of asphalt binder models using molecular dynamics (md) method. *Construction and Building Materials*, 162:430 – 441, 2018.

[71] Guangji Xu. *Characterization of Asphalt Properties and Asphalt-Aggregate Interaction Using Molecular Dynamics Simulation.* Graduate Program in Civil and Environmental Engineering, Graduate School-New Brunswick Rutgers, The State University of New Jersey, 2017.

[72] Zhao Du and Xingyi Zhu. Molecular dynamics simulation to investigate the adhesion and diffusion of asphalt binder on aggregate surfaces. *Transportation Research Record: Journal of the Transportation Research Board*, 2673:036119811983722, 2019.

[73] Guangji Xu and Hao Wang. Study of cohesion and adhesion properties of asphalt concrete with molecular dynamics simulation. *Computational Materials Science*, 112:161–169, 2016.

[74] Zhengwu Long, Lingyun You, Xianqiong Tang, Wenbo Ma, Yanhuai Ding, and Fu Xu. Analysis of interfacial adhesion properties of nano-silica modified asphalt mixtures using molecular dynamics simulation. *Construction and Building Materials*, 255:119354, 2020.

[75] Verónica M. Sánchez and Caetano R. Miranda. Modeling acid oil component interactions with carbonate reservoirs: A first-principles view on low salinity recovery mechanisms. *The Journal of Physical Chemistry C*, 118(33):19180–19187, 2014.

[76] Vagner A. Rigo, Cigdem O. Metin, Quoc P. Nguyen, and Caetano R. Miranda. Hydrocarbon adsorption on carbonate mineral surfaces: A first-principles study with van der waals interactions. *The Journal of Physical Chemistry C*, 116(46):24538–24548, 2012.

[77] Rochele C. A. Bevilaqua, Vagner A. Rigo, Marcos Veríssimo-Alves, and Caetano R. Miranda. Nmr characterization of hydrocarbon adsorption on calcite surfaces: A first principles study. *The Journal of Chemical Physics*, 141(20):204705, 2014.

[78] Raphael S. Alvim, Filipe C. D. A. Lima, Verónica M. Sánchez, Thomas F. Headen, Edo S. Boek, and Caetano R. Miranda. Adsorption of asphaltenes on the calcite (10.4) surface by first-principles calculations. *RSC Adv.*, 6:95328–95336, 2016.

[79] P. Hohenberg and W. Kohn. Inhomogeneous electron gas. *Phys. Rev.*, 136:B864–B871, 1964.

[80] W. Kohn and L. J. Sham. Self-consistent equations including exchange and correlation effects. *Phys. Rev.*, 140:A1133–A1138, 1965.

[81] D. M. Ceperley and B. J. Alder. Ground state of the electron gas by a stochastic method. *Phys. Rev. Lett.*, 45:566–569, 1980.

[82] John P. Perdew, Kieron Burke, and Matthias Ernzerhof. Generalized gradient approximation made simple. *Phys. Rev. Lett.*, 77:3865–3868, 1996.

[83] John P. Perdew, Kieron Burke, and Yue Wang. Generalized gradient approximation for the exchange-correlation hole of a many-electron system. *Phys. Rev. B*, 54:16533–16539, 1996.

[84] O. Anatole von Lilienfeld, Ivano Tavernelli, Ursula Rothlisberger, and Daniel Sebastiani. Optimization of effective atom centered potentials for london dispersion forces in density functional theory. *Phys. Rev. Lett.*, 93:153004, 2004.

[85] I-Chun Lin, Maurício D. Coutinho-Neto, Camille Felsenheimer, O. Anatole von Lilienfeld, Ivano Tavernelli, and Ursula Rothlisberger. Library of dispersion-corrected atom-centered potentials for generalized gradient approximation functionals: Elements h, c, n, o, he, ne, ar, and kr. *Phys. Rev. B*, 75:205131, 2007.

[86] G. Makov and M. C. Payne. Periodic boundary conditions in ab initio calculations. *Phys. Rev. B*, 51:4014–4022, 1995.

[87] Charles Kittel. *Introduction to Solid State Physics, 8th Edition*. John Wiley & Sons, 2004.

[88] C Kittel. Introduction to solid state physics. fifth edition, 1976.

[89] H. Hellmann. A new approximation method in the problem of many electrons. *The Journal of Chemical Physics*, 3(1):61–61, 1935.

[90] David Vanderbilt. Soft self-consistent pseudopotentials in a generalized eigenvalue formalism. *Phys. Rev. B*, 41:7892–7895, 1990.

[91] Loup Verlet. Computer "experiments" on classical fluids. i. thermodynamical properties of lennard-jones molecules. *Phys. Rev.*, 159:98–103, 1967.

[92] H. Sun. Compass: An ab initio force-field optimized for condensed-phase applicationsoverview with details on alkane and benzene compounds. *The Journal of Physical Chemistry B*, 102(38):7338–7364, 1998.

[93] Hockney R. W. and Eastwood J. W. *Computer Simulation Using Particles*. Taylor & Francis Group, 1988.

[94] A. D. MacKerell, D. Bashford, M. Bellott, R. L. Dunbrack, J. D. Evanseck, M. J. Field, S. Fischer, J. Gao, H. Guo, S. Ha, D. Joseph-McCarthy, L. Kuchnir, K. Kuczera, F. T. K. Lau, C. Mattos, S. Michnick, T. Ngo, D. T. Nguyen, B. Prodhom, W. E. Reiher, B. Roux, M. Schlenkrich, J. C. Smith, R. Stote, J. Straub, M. Watanabe, J. Wiórkiewicz-Kuczera, D. Yin, and M. Karplus. All-atom empirical potential for molecular modeling and dynamics studies of proteins. *The Journal of Physical Chemistry B*, 102(18):3586–3616, 1998.

[95] K. Vanommeslaeghe, E. Hatcher, C. Acharya, S. Kundu, S. Zhong, J. Shim, E. Darian, O. Guvench, P. Lopes, I. Vorobyov, and A. D. Mackerell Jr. Charmm general force field: A force field for drug-like molecules compatible with the charmm all-atom additive biological force fields. *Journal of Computational Chemistry*, 31(4):671–690, 2010.

[96] Wenbo Yu, Xibing He, Kenno Vanommeslaeghe, and Alexander D. MacKerell Jr. Extension of the charmm general force field to sulfonyl-containing compounds and its utility in biomolecular simulations. *Journal of Computational Chemistry*, 33(31):2451–2468, 2012.

[97] Eduardo R. Cruz-Chu, Aleksei Aksimentiev, and Klaus Schulten. Water-silica force field for simulating nanodevices. *The Journal of Physical Chemistry B*, 110(43):21497–21508, 2006.

[98] Joerg R. Hill and Joachim Sauer. Molecular mechanics potential for silica and zeolite catalysts based on ab initio calculations. 1. dense and microporous silica. *The Journal of Physical Chemistry*, 98(4):1238–1244, 1994.

[99] Thomas Lengauer and Matthias Rarey. Computational methods for biomolecular docking. *Current Opinion in Structural Biology*, 6(3):402 – 406, 1996.

[100] Leonardo G. Ferreira, Ricardo N. Dos Santos, Glaucius Oliva, and Adriano D. Andricopulo. Molecular docking and structure-based drug design strategies. *Molecules (Basel, Switzerland)*, 20(7):13384–13421, 2015.

[101] Barry L. Stoddard and Daniel E. Koshland. Prediction of the structure of a receptor-protein complex using a binary docking method. *Nature*, 358(6389):774–776, 1992.

[102] Garrett M. Morris, David S. Goodsell, Ruth Huey, and Arthur J. Olson. Distributed automated docking of flexible ligands to proteins: Parallel applications of autodock 2.4. *Journal of Computer-Aided Molecular Design*, 10(4):293–304, 1996.

[103] Julie R. Schames, Richard H. Henchman, Jay S. Siegel, Christoph A. Sotriffer, Haihong Ni, and J. Andrew McCammon. Discovery of a novel binding trench in hiv integrase. *Journal of Medicinal Chemistry*, 47(8):1879–1881, 2004.

[104] Jie Liu and Renxiao Wang. Classification of current scoring functions. *Journal of Chemical Information and Modeling*, 55(3):475–482, 2015.

[105] Garrett M. Morris, Ruth Huey, William Lindstrom, Michel F. Sanner, Richard K. Belew, David S. Goodsell, and Arthur J. Olson. Autodock4 and autodocktools4: Automated docking with selective receptor flexibility. *Journal of Computational Chemistry*, 30(16):2785–2791, 2009.

[106] Garrett M. Morris and David S. Eisenberg. *User Guide AutoDock Version 4.2, Updated for version 4.2.6.* The Scripps Research Institute Molecular Graphics Laboratory 10550 N. Torrey Pines Rd. La Jolla, California 92037-1000 USA, 2014.

[107] Garrett M. Morris, David S. Goodsell, Robert S. Halliday, Ruth Huey, William E. Hart, Richard K. Belew, and Arthur J. Olson. Automated docking using a lamarckian genetic algorithm and an empirical binding free energy function. *Journal of Computational Chemistry*, 19:1639–1662, 1998.

[108] Francisco J. Solis and Roger J.-B. Wets. Minimization by random search techniques. *Mathematics of Operations Research*, 6(1):19–30, 1981.

[109] Miguel de Carvalho. A generalization of the solis–wets method. *Journal of Statistical Planning and Inference*, 142(3):633–644, 2012.

[110] Jan Fuhrmann, Alexander Rurainski, Hans-Peter Lenhof, and Dirk Neumann. A new lamarckian genetic algorithm for flexible ligand-receptor docking. *Journal of computational chemistry*, 31(9):1911–1918, 2010.

[111] Paolo Giannozzi, Stefano Baroni, Nicola Bonini, Matteo Calandra, Roberto Car, Carlo Cavazzoni, Davide Ceresoli, Guido L Chiarotti, Matteo Cococcioni, Ismaila Dabo, Andrea Dal Corso, Stefano de Gironcoli, Stefano Fabris, Guido Fratesi, Ralph Gebauer, Uwe Gerstmann, Christos Gougoussis, Anton Kokalj, Michele Lazzeri, Layla Martin-Samos, Nicola Marzari, Francesco Mauri, Riccardo Mazzarello, Stefano Paolini, Alfredo Pasquarello, Lorenzo Paulatto, Carlo Sbraccia, Sandro Scandolo, Gabriele Sclauzero, Ari P Seitsonen, Alexander Smogunov, Paolo Umari, and Renata M Wentzcovitch. QUANTUM ESPRESSO: a modular and open-source software project for quantum simulations of materials. *Journal of Physics: Condensed Matter*, 21(39):395502, 2009.

[112] Quantum-ESPRESSO. https://www.quantum-espresso.org/, 2009.

[113] W Tang, E Sanville, and G Henkelman. A grid-based bader analysis algorithm without lattice bias. *Journal of Physics: Condensed Matter*, 21(8):084204, 2009.

[114] Edward Sanville, Steven D. Kenny, Roger Smith, and Graeme Henkelman. Improved grid-based algorithm for bader charge allocation. *Journal of Computational Chemistry*, 28(5):899–908, 2007.

[115] Graeme Andrew Henkelman, Andri Arnaldsson, and Hannes Jónsson. A fast and robust algorithm for bader decomposition of charge density. *Computational Materials Science*, 36(3):354–360, 2006.

[116] Min Yu and Dallas R. Trinkle. Accurate and efficient algorithm for bader charge integration. *The Journal of Chemical Physics*, 134(6):064111, 2011.

[117] I. Kowalewski, M. Vandenbroucke, A. Y. Huc, M. J. Taylor, and J. L. Faulon. Preliminary results on molecular modeling of asphaltenes using structure elucidation programs in conjunction with molecular simulation programs. *Energy & Fuels*, 10(1):97–107, 1996.

[118] L. Martínez, R. Andrade, E. G. Birgin, and J. M. Martínez. Packmol: A package for building initial configurations for molecular dynamics simulations. *Journal of Computational Chemistry*, 30(13):2157–2164, 2009.

[119] Aidan P. Thompson, Steven J. Plimpton, and William Mattson. General formulation of pressure and stress tensor for arbitrary many-body interaction potentials under periodic boundary conditions. *The Journal of Chemical Physics*, 131(15):154107, 2009.

[120] D.J. Evans and G.P. Morriss. Nonlinear-response theory for steady planar couette flow. *Physical Review A*, 30(3):1528–1530, 1984.

[121] Melville S. Green. Markoff random processes and the statistical mechanics of time-dependent phenomena. ii. irreversible processes in fluids. *The Journal of Chemical Physics*, 22(3):398–413, 1954.

[122] Shuichi Nosé. A unified formulation of the constant temperature molecular dynamics methods. *The Journal of Chemical Physics*, 81(1):511–519, 1984.

[123] William G. Hoover. Canonical dynamics: Equilibrium phase-space distributions. *Phys. Rev. A*, 31:1695–1697, 1985.

[124] Peter J. Daivis and B. D. Todd. A simple, direct derivation and proof of the validity of the sllod equations of motion for generalized homogeneous flows. *The Journal of Chemical Physics*, 124(19):194103, 2006.

[125] Billy D. Todd and Peter J. Daivis. *Nonequilibrium Molecular Dynamics: Theory, Algorithms and Applications*. Cambridge University Press, 2017.

[126] Christian D. Lorenz, Paul S. Crozier, Joshua A. Anderson, and Alex Travesset. Molecular dynamics of ionic transport and electrokinetic effects in realistic silica channels. *The Journal of Physical Chemistry C*, 112(27):10222–10232, 2008.

[127] M. Parrinello and A. Rahman. Polymorphic transitions in single crystals: A new molecular dynamics method. *Journal of Applied Physics*, 52(12):7182–7190, 1981.

[128] Glenn J. Martyna, Douglas J. Tobias, and Michael L. Klein. Constant pressure molecular dynamics algorithms. *The Journal of Chemical Physics*, 101(5):4177–4189, 1994.

[129] William L. Jorgensen, David S. Maxwell, and Julian Tirado-Rives. Development and testing of the opls all-atom force field on conformational energetics and properties of organic liquids. *Journal of the American Chemical Society*, 118(45):11225–11236, 1996.

[130] Lucas S. de Lara, Mateus F. Michelon, and Caetano R. Miranda. Molecular dynamics studies of fluid/oil interfaces for improved oil recovery processes. *The Journal of Physical Chemistry B*, 116(50):14667–14676, 2012.

[131] Abbas Mohajerani, Lucas Burnett, John V. Smith, Halenur Kurmus, John Milas, Arul Arulrajah, Suksun Horpibulsuk, and Aeslina Abdul Kadir. Nanoparticles in construction materials and other applications, and implications of nanoparticle use. *Materials*, 12(19), 2019.

[132] Ahmed Alhosani and Nagu Daraboina. Unified Model to Predict Asphaltene Deposition in Production Pipelines. *Energy & Fuels*, 34(2):1720–1727, 2020.

[133] Garrett M. Morris. http://autodock.scripps.edu/, 1989.

[134] M. Valiev, E.J. Bylaska, N. Govind, K. Kowalski, T.P. Straatsma, H.J.J. Van Dam, D. Wang, J. Nieplocha, E. Apra, T.L. Windus, and W.A. de Jong. Nwchem: A comprehensive and scalable open-source solution for large scale molecular simulations. *Computer Physics Communications*, 181(9):1477 – 1489, 2010.

[135] Marcus G. Martin. Mcccs towhee: a tool for monte carlo molecular simulation. *Molecular Simulation*, 39(14-15):1212–1222, 2013.

[136] BIOVA. Materials studio version 7.0. https://www.3dsbiovia.com/products/collaborative-science/biovia-materials-studio/, 2013.

[137] Hassan K. Al Halwachi, Dmitry S. Yakovlev, and Edo S. Boek. Systematic optimization of asphaltene molecular structure and molecular weight using the quantitative molecular representation approach. *Energy & Fuels*, 26(10):6177–6185, 2012.

[138] I.A. Wiehe and K.S. Liang. Asphaltenes, resins, and other petroleum macromolecules. *Fluid Phase Equilibria*, 117(1):201 – 210, 1996.

[139] Eric Y. Sheu and Oliver C. Mullins. Asphaltene fundamentals and applications. *Springer Science and Business Media*, 2013.